Max-Planck-Institut
für Meteorologie

EXAMENSARBEIT Nr. 28

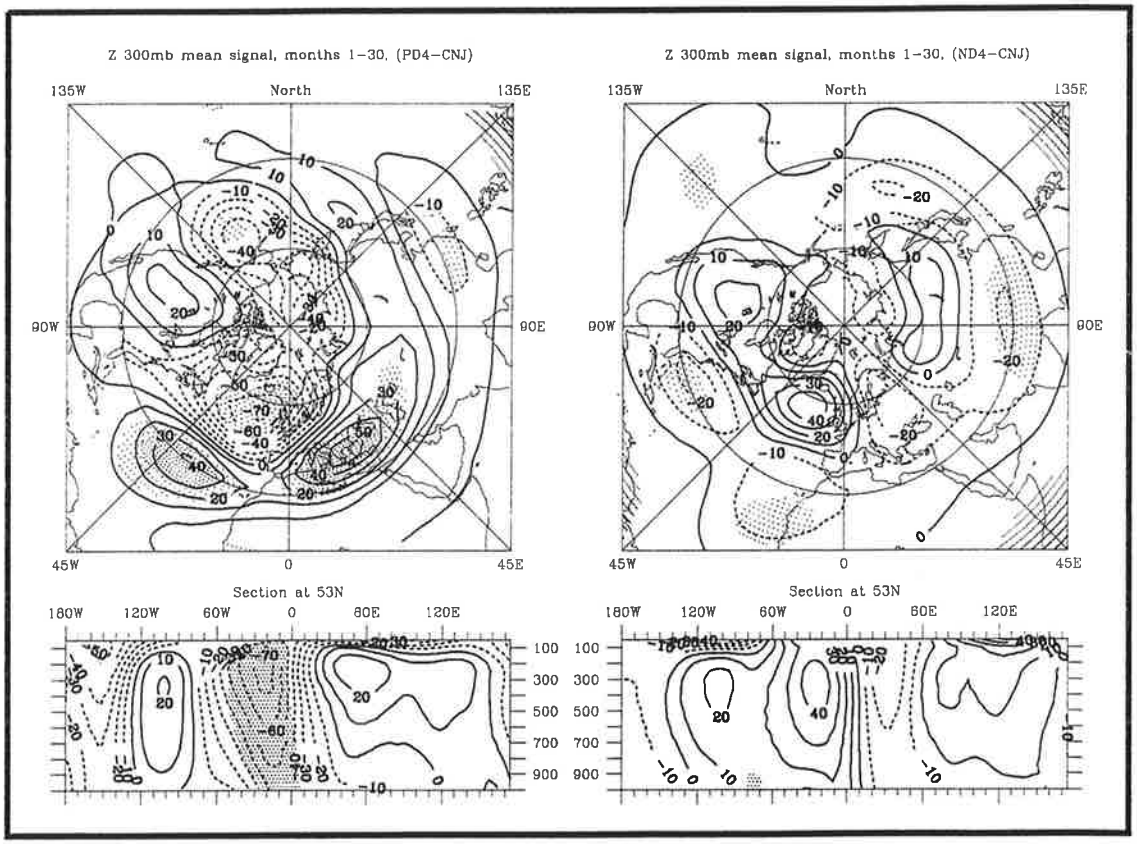

THE ATMOSPHERIC RESPONSE TO NORTH ATLANTIC SEA SURFACE TEMPERATURE ANOMALIES IN GCM EXPERIMENTS

VON

VIACHESLAV V. KHARIN

HAMBURG, Mai 1995

Dissertation im Rahmen des Promotionsverfahrens

Autor:

Viacheslav V. Kharin

Max-Planck-Institut
für Meteorologie

MAX-PLANCK-INSTITUT
FÜR METEOROLOGIE
BUNDESSTRASSE 55
D-20146 Hamburg
F.R. GERMANY

Tel.: +49-(0)40-4 11 73-0
Telefax: +49-(0)40-4 11 73-298
E-Mail: <name> @ dkrz.d400.de

The Atmospheric Response to North Atlantic Sea Surface Temperature Anomalies in GCM Experiments

Dissertation
zur Erlangung des Doktorsgrades
der Naturwissenschaften im Fachbereich
Geowissenschaften
der Universität Hamburg

vorgelegt von

Viacheslav V. Kharin

aus
Serov, Sverdlowsk Gebiet, Rußland

Hamburg
1995

ISSN 0938-5177

Als Dissertation angenommen vom Fachbereich Geowissenschaften
der Universität Hamburg

auf Grund der Gutachten von Prof. Dr. Klaus Fraedrich

und Dr. Hans von Storch

Hamburg, den 26. April, 1995

Professor Dr. M. Dunst
Sprecher des Fachbereichs Geowissenschaften

Contents

1 Introduction

1.1 Review of present understanding of the atmospheric response to extratropical SST anomalies

The problem of large scale air-sea interaction in middle latitudes frequently attracts the attention of meteorologists and climatologists attempting to use sea surface temperature (SST) anomalies as a significant predictor of climate on time scales of a month to a season. Namias (1964, 1978), for example, tried to relate the activity of blocking events in 1958-1960 over Northern Europe to an anomalously cold SST off Newfoundland, and SST anomalies in the North Pacific to an anomalous winter circulation over North America.

The subject of the role of extratropical SST anomalies in atmospheric circulation are rather controversial. Some authors have reported feedback relationships between Atlantic SST anomalies and monthly atmospheric circulation anomalies over western Europe. Particularly, Ratcliffe and Murray (1970) showed that cold SST anomalies in a key area in the North Atlantic south of Newfoundland are associated with blocking patterns over Northern and Western Europe the following month whereas a warmer than usual ocean in the same area favours a more zonal circulation. On the other hand, Barnett et al. (1984) did not find statistically significant indications that SST anomalies in North Atlantic could serve as a good predictor for seasonal surface air temperature anomalies over Europe and Asia.

Many papers published during recent years have been devoted to the study of observed atmosphere/ocean interactions in midlatitudes on seasonal and annual time scales. Several different techniques of statistical analysis, such as canonical correlation analysis, singular value decomposition etc., have been used to define coupled modes of air-sea variability (Lanzante, 1984; Dymnikov and Filin, 1985a; Wallace and Jiang, 1987; Wallace et al., 1990; Wallace et al., 1992; Zorita et al., 1992, to name a few). Summarizing the results of these studies, one might conclude that there is a large scale nonlocal relation between the atmosphere and the ocean in midlatitudes on these time scales.

Leading patterns of atmospheric extratropical variability are statistically significantly correlated with extratropical SST anomalies. Lag correlations between observed time series of SST and different atmospheric parameters indicate that the atmosphere mainly leads the ocean on seasonal and annual time scales (Davis, 1978; Wallace and

Jiang, 1987; Zorita et al., 1992). Nevertheless, a possible atmospheric response to SST anomalies is not excluded in such relationships. Since the characteristic time scale of the atmospheric reaction to extratropical SST anomalies is of order of a few days such a response cannot be seen in lag correlations based on monthly or seasonal data sets.

The analysis of the best correlated patterns between observed 500 mb geopotential height (H500) or sea level pressure (SLP) over the Northern Hemisphere and SST in the North Atlantic and the North Pacific in winter indicates that the air-ocean interaction in midlatitudes has possibly a modal character. Atmospheric modes obtained by means of a singular vector decomposition technique (Wallace et. al., 1992) or a canonical correlation analysis (Zorita et al., 1992) are similar to well known North Atlantic and West Atlantic teleconnection patterns identified by Wallace and Gutzler (1981). This result seems to be important because it demonstrates that possible reactions of the extratropical atmosphere to SST anomalies can be interpreted in terms of normal modes rather than in terms of local wave-trains (see also Wallace and Jiang, 1987).

The study of observed correlation linkages alone cannot answer the question of how strong the atmospheric response to SST anomalies actually is. Numerous publications in the recent years have been devoted to the study of the sensitivity of the atmospheric circulation to extratropical SST anomalies in general circulation models (GCMs) of different complexity (e.g. Pitcher et al., 1988; Palmer and Sun, 1985; Lau and Nath, 1990, 1994; Kushnir and Lau, 1992). They have shown that the physical processes involved in the formation of the atmospheric response are very complicated and the model results depend on the GCM used.

The theory of stationary Rossby-wave dispersion (e.g. Hoskins and Karoly, 1981; Webster, 1981) supplies us with a theoretical background on a possible stationary atmospheric response to stationary heating. According to this theory, an extratropical near surface heating anomaly in winter has to be mainly compensated by the horizontal advection of cold air from northern regions leading to the formation of a low pressure system downstream of the heat source at lower levels. In the vicinity of the heat source the atmospheric response is baroclinic with a westward tilt over the SST anomaly. Far away from the heat source the atmospheric response resembles the equivalent barotropic wave train propagating north- and south-eastwards from the source. Numerical simulations based on simple models linearized about the zonal flow (e.g. Held, 1983) demonstrated that Rossby waves propagating from the source of vorticity can interfere with each other leading to a resonantly strong response at certain wavenumber if the atmospheric diffusion is not too large.

The relation between SST anomalies and heating in midlatitudes is not obvious. The dependence of anomalous sensible and latent heat fluxes into the atmosphere on SST anomalies is nonlinear and nonlocal. The heat content in the water evaporated over a SST anomaly can be released far away from the source in the form of rainfall. The feedback relationships between anomalous atmospheric circulation and the heat source complicate the assessment of the heat forcing due to SST anomalies. Moreover, recent experimental studies (Palmer and Sun, 1985; Dymnikov and Filin, 1985a,b; Lau and Nath, 1990) suggested that transient eddies play an substantial role in the formation of atmospheric anomalies on monthly and seasonal time scales.The variability of the stormtracks due to SST anomalies leads to changes of the feedback forcing of the mean flow by synoptical scale eddies. The geographical localization of zones of high baroclinicity due to zonal asymmetry of the basic atmospheric flow with respect to SST anomalies seems to be important, too (Ting, 1991).

In view of the complex character of the air-sea interactions in middle latitudes, possibly the most appropriate tool for studying the reaction of the atmosphere to extratropical SST anomalies are general circulation models with a fine spatial resolution and a complex and full parameterization of physical processes in the atmospheric boundary layer. Most GCM studies examined only the stationary response of the model atmosphere. The main difficulty involved in such studies is the high natural variability of the atmosphere on monthly time scales in middle latitudes which hides the atmospheric signal caused by SST anomalies. The usual way to overcome the problem is to integrate the GCM over a long time period and to compare climatological means of the anomaly run to those of the control run (e.g. Pitcher et al., 1988). Other authors (e.g. Palmer and Sun, 1985) have produced several GCM runs for a shorter time period, but still long enough to attain the ultimate amplitude for the atmospheric signal, starting from different initial conditions and averaging the results over all integrations.

Assuming that the atmospheric response behaves linearly with respect to the SST anomaly sign the statistical significance of the results can be increased if a "positive anomaly" run is compared with a "negative anomaly" run. However, the question on the linearity of the atmospheric response to SST anomalies of 2-4 K used in the most of GCM studies is open. Pitcher et al. (1988) showed that the model response in the NCAR Community Climate general circualtion model to ± 2 K SST anomalies in the North Pacific was not symmetric.

Palmer and Sun (1985) investigated the atmospheric response in the GCM of the U.K. Meteorological Office to a SST anomaly in the north-west Atlantic with the am-

plitude of about 3 K. They obtained a positive geopotential height anomaly over the central North Atlantic downstream of the positive SST anomaly and a negative height anomaly over Europe. The response appeared to be equivalent barotropic and inconsistent with the thermal forcing theory of Hoskins and Karoly (1981). The anomalous baroclinic wave activity over the Atlantic was suggested to be essential as a momentum forcing for the anomalous time-mean flow pattern. On the other hand, the role of thermal forcing, provided by anomalous diabatic heating and transient eddy heat flux convergence, may be still important for the obtained atmospheric reaction.

Bjerknes (1962) suggested that the atmospheric response on SST anomalies could be important on these time scale. Hense et al. (1990) examined the stationary atmospheric response in a GCM on large scale SST anomalies in the Atlantic Ocean derived from SST observed in 1903-1914 ("cold event") and in 1951-1960 ("warm event"). The SST anomalies they used covers the whole Atlantic basin. The changes in GCM surface pressure over the Northern Hemisphere due to the SST changes were in broad agreement with the observations. The atmospheric signal was found to be recurrent only in scale-dependent hierarchy based on spherical harmonics and in that based on the advection operator at 1000 mb, and to be not statistically significant in the hierarchy based on the barotropic normal modes of the mean 300 mb flow. The authors concluded that at low levels, local heating and advection are dominant mechanisms in the atmospheric reaction, but at upper levels the extratropical signal is a remote response to modifications of the tropical convetion.

Dymnikov and Filin (1985b) studied besides the stationary response of the model atmosphere also the transient processes involved in the formation of the atmospheric anomalies due to SST anomalies of different spatial configurations in the North Atlantic. They revealed different phases of the behavior of the atmospheric response: the local generation of vorticity anomaly and its advection downstream with the mean flow and the propagation of Rossby waves from the heat source. The GCM they used had, however, a coarse spatial resolution (10° in longitude, 6° in latitude and 3 levels in the vertical). The authors carried out only one single 60-day integration for each type of SST anomaly so that the statistical stability of the results is questionable.

1.2 Concept and organization of the present study

This study is aimed to examine the dynamical processes involved in the formation of the atmospheric response to extratropical SST anomalies in the North Atlantic in a

GCM. Both, the stationary and the transient atmospheric responses will be discussed. *Long term integrations* of the GCM with constant SST anomalies during the whole integration period in the perpetual January conditions were performed to study the stationary reaction of the model atmosphere in winter. The results of such long term integrations can be of interest for studies of atmospheric deviations due to SST changes on decadal time scales.

On time scales shorter than a month transient effects can be of importance. The nonstationary atmospheric behavior during the first few weeks after introducing SST anomalies was studied in *Monte-Carlo simulations*. In these experiments SST anomalies were "turned on" instantly at the beginning of integrations. This can be considered as an extreme case of a strong storm passing over the ocean and thus changing within a short time the surface temperature via extremely high heat flux anomalies and enhanced mixing. The characteristic time scale of wintertime SST anomalies in the middle latitudes is, however, much larger than the dominant time scale of a few days of the atmospheric forcing fields, even though substantial SST changes may occur over short periods (e.g. Frankignoul, 1985). Thus the above interpretation may be considered only with reservations. Nevertheless, the experiments of this kind allow to study possible physical processes and mechanisms which could be relevant for the atmospheric response in the observed air-sea interactions.

The intermediate and more realistic situation between the two extreme cases, the stationary response in the long term experiments and instantaneous atmospheric reaction in the Monte-Carlo experiments, can be achieved in GCM experiments made with time variable SST, e.g. with observed SST. A number of such experiments have been made and analyzed recently by a number of authors (e.g. Graham et al., 1994; Lau and Nath, 1990, 1994; Kharin, 1994). The problem of the relative importance of tropical and extratropical SST can be also concerned in the experiments forced by observed SST. Particularly, Graham et al. (1993) and Kharin (1994) studied atmospheric variability in three GCM experiments one of which was forced by global observed 1970-1988 monthly SST (the GAGO run) and two other were made with observed SST variability limited to tropical regions (the TOGA run) and to extratropical regions (the MOGA run). Similar experiments but with an another GCM and for a slightly different time period were carried out by Lau and Nath (1994). They produced for each type of SST forcing (global, tropical and extratropical) four independent realizations, increasing the statistical value of their results. All of the GCM experiments were able to reproduce certain aspects of the observed circulation variability with the best agreement if the

tropical SST anomalies were included. Graham et al. (1994) found some indications of the atmospheric response to SST anomalies in the extratropical North Pacific. The decadal shift in the mid-1970's was reproduced in each experiment with best results over the North Pacific in the TOGA run and over the North Atlantic and Europe in the GAGO and MOGA experiments. Lau and Nath (1994) found the response to the midlatitude SST anomalies in the North Pacific to be weaker and less systematic than the response to the tropical SST variability.

In the present study special attention is given to dynamical mechanisms for the atmospheric response in the GCM experiments. The quasigeostrophic potential vorticity theory (e.g. Pedlosky, 1979) is applied to explain the behavior of the atmospheric response in the first few days. On longer time scales the ideas of barotropic instability and barotropic normal modes of zonally asymmetric flows are applied (see e.g. Branstator, 1985a,b; Dymnikov and Skiba, 1985). Normal modes in the GCM are compared with the leading modes of the atmospheric variability and with the atmospheric response to SST anomalies.

The work is organized as follows. First, we present in Section 2 some observational indications of air-sea interactions in the North Atlantic region after Zorita et al. (1992). Section 3 gives a short description of the GCM and the design of numerical experiments as well as the statistical methods used for the assessment of the GCM results. The results of the Monte-Carlo and the long term experiments are discussed in Sections 4 and 5, respectively. GCM experiments made with observed SST anomalies are discussed in Section 6 after Kharin (1994). Barotropic normal modes are described in Section 7. Conclusions and discussions follow in Section 8. Some technical aspects and tests for the statistical assessment of the results of the canonical correlation analysis are gathered in Appendices.

2 Observed air-sea relationships in the North Atlantic

To have an idea about air-sea interactions in extratropics we present in this paragraph the results of the canonical correlation analysis (CCA) applied to observed winter monthly means of SST and SLP in the North Atlantic region after Zorita et al. (1992). Data sets used in the analysis were taken from the COADS (Woodruff et al., 1987) and covered the winter period (December, January, February) 1951-1986. Without going into much details of the CCA (see e.g. Anderson, 1984) we note only that this method allows to select pairs of patterns of two space-time dependent variables such that their time coefficients are optimally correlated. Mathematically, the problem is reduced to a coupled eigenvalue problem, the eigenvectors of which define canonical patterns and the eigenvalues are squared correlations between the time coefficients of the canonical patterns. Previous to the CCA the SST and SLP fields were filtered by projecting the original data onto their empirical orthogonal functions (EOFs) and retaining only the first 5 EOFs for each field, explaining most of the total variance (87% and 62% for SLP and SST, respectively). The canonical time series are normalized to variance one so that the canonical maps represent the "typical" strength of the signal.

The first two pairs of patterns with canonical correlations 0.56 and 0.47, respectively, are shown in Figure 9. The first canonical patterns of SLP (Figure 9a) and SST (Figure 9b) explain about 20% of the total variance. The mutual configuration of the canonical maps is consistent with the hypothesis of atmospheric anomalies causing SST anomalies. The main features of the SLP pattern are an increase of the westerly wind at about $50°N$ and an anomalous anticyclonic circulation centered at $30°N$ $40°W$. North of the anticyclonic, where the westerly wind is enhanced, the ocean surface is cooler than normal. West of the anticyclone, where the southerly winds are enhanced, the ocean is warmed substantially. Lag correlations between the canonical time series support the leading role of the atmosphere: the 1-month lag correlation is .65 if SLP leads SST but only .09 if SLP is lagging.

The second canonical SLP map (Figure 9c) explains 31% of the total variance and the corresponding SST pattern (Figure 9d) explains 15%. This second CCA pair can be interpreted in the same manner as the first one. If SLP leads SST by 1 month, the lag correlation is 0.48 compared to .03 if SLP lags by 1 month.

The first canonical SST pattern (Figure 9b) resembles the first EOF of SST in the

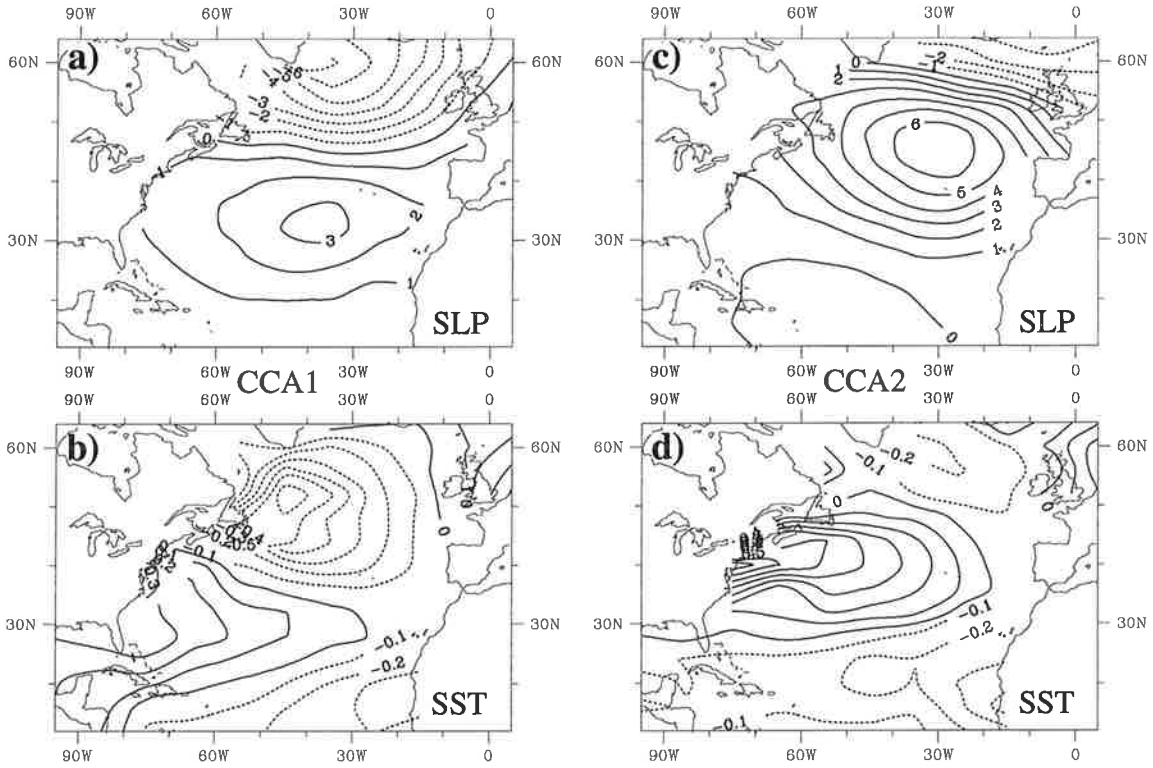

Figure 1: *The patterns of the first two canonical pairs of SLP (a, c) and SST (b, d) in the North Atlantic area in winter 1951-1986. The correlation between the corresponding canonical time series is 0.56 for the first pair and 0.47 for the second pair. Contour interval is 1 mb for SLP and 0.1 K for SST.*

North Atlantic in winter and the second canonical pattern (Figure 9d) is similar to the second SST EOF. With respect to SLP, the order is, however, reversed. The second canonical SLP pattern (Figure 9a) is similar to the first SLP EOF and represents most of the month-to-month wintertime variability (31%). The first canonical SLP map (Figure 9c) is like the second SLP EOF and represents only 21% of the SLP variance. Seemingly, the SST response to the first SLP EOF is weaker than the response to the second EOF. This fact could be explained, for example, by the following hypothetical mechanism: the atmospheric response to a SST anomaly with the first canonical pattern is stronger than to a SST anomaly with the second canonical pattern and contributes positively to the observed atmospheric canonical pattern.

3 Design of GCM experiments

The Hamburg low resolution version of the ECMWF spectral general circulation model ECHAM2 with triangular truncation of the spectral harmonic representation at wavenumber T21 was used for numerical experiments. A detailed description of the GCM can be found in Roeckner et al. (1992). Nonlinear terms and parameterization of diabatic processes are evaluated on a near regular "Gaussian" grid with spatial resolution of about 5.6° in longitude and latitude. The vertical resolution of the GCM is 19 levels combining a sigma-coordinate at low model levels with a constant pressure coordinate in the stratosphere.

The parameterization of physical processes comprises radiation, cloud cover, large-scale condensation and deep convection schemes, turbulent vertical diffusion and three-layer diffusion of heat and moisture in the ground. The exchange of heat, moisture and momentum at the surface, as well as vertical turbulent transport in the model planetary layer are provided by a diffusion scheme with coefficients depending on stability (Richardson number), vertical wind shear and mixing length. The planetary boundary layer is resolved by about four layers. The surface drag coefficients are determined as a function of roughness length and Richardson number via Monin-Obukhov similarity theory. The ECHAM2/T21 model employs orography representation spectrally fitted to the model resolution and uses no gravity wave drag. The Reynolds (1988) SST climatology and the sea-ice dataset of Alexander and Mobley (1976) were used for the lower boundary condition in the ECHAM2 model.

In the Monte-Carlo simulations and in the long term experiments the model was integrated with climatological January conditions for the radiation scheme and for the surface boundary distributions (deep soil temperature and deep soil wetness). The control run, hereafter denoted as the CNJLT ("CoNtrol permanent January Long Term") run, was performed for 30 months with the climatological January SST field.

The ECHAM2/T21 model performs quite well in the Northern Hemisphere. The long-term mean circulation and the interannual atmospheric variability has been thoroughly studied by several authors (e.g. Roeckner et al., 1992). The position and the amplitude of planetary stationary waves is well simulated. The baroclinic activity is, however, underrepresented in the model, mainly due to low spatial resolution.

As an example, Figure 9 demonstrates the time mean of relative vorticity derived from geopotential height at 500 hPa in the control CNJLT run (a) and observed in winter 1970-1987 provided by NCAR (b). The details of the derivation of the relative

vorticity field from the geopotential height field are presented in Appendix C. The general structure of stationary planetary waves is correctly reproduced in the GCM. A more careful analysis of the patterns reveals some differences in the amplitude of the main vorticity centers. The amplitude of the vorticity dipole in the western North Pacific in the GCM is larger than in the observations. The observed positive vorticity center over the Mediterranean Sea is stronger than in the CNJLT run. In the North Atlantic sector the amplitude of the vorticity centers in the observations and in the GCM is comparable.

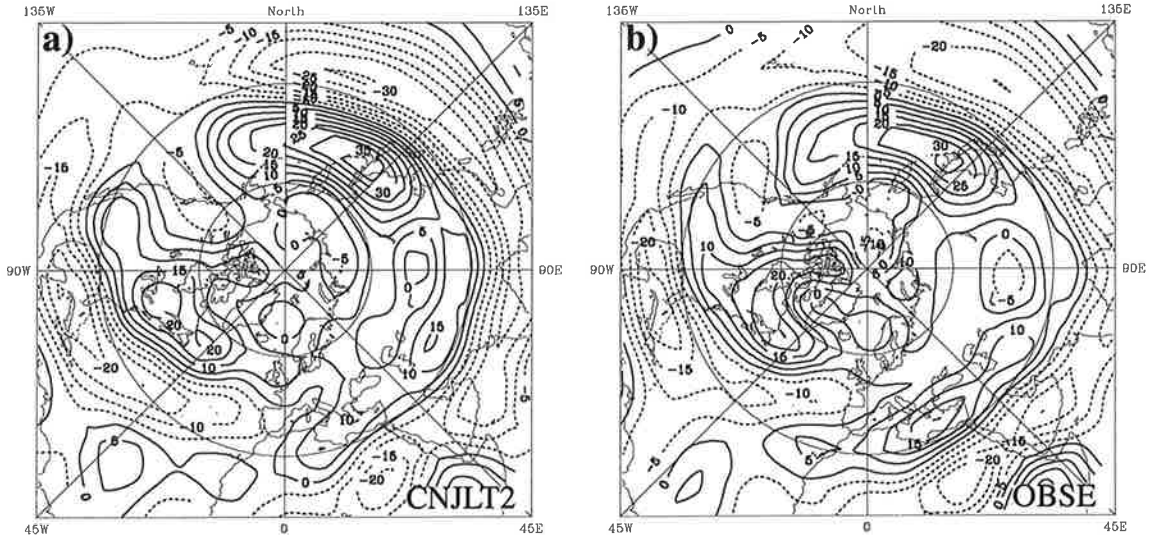

Figure 2: *The time mean of relative vorticity at 500 hPa in the CNJLT run (a) and observed in 1970-1987 (b) derived from 500 hPa geopotential height. Contour interval is* $5 \times 10^{-6} sec^{-2}$*; labels are multiplied by* 10^6.

3.1 The SST anomalies

Most of results of the SST sensitivity experiments discussed in this study were obtained for the SST anomalies derived from the first canonical pattern of observed SST described in the previous section (Figure 9b). This pattern was shown by Zorita et al. (1992) to be the dominant variability mode of wintertime SST. Since we are interested in the atmospheric response only to extratropical SST anomalies we omitted the subtropical center of the SST variability in the upwelling zone off the African coast presented in the original canonical pattern.

As we already mentioned in Introduction, numerous previous studies reported about difficulties to detect the extratropical atmospheric signal to SST anomalies of moderate

amplitudes below 2 K located in the middle latitudes. Taking into account this fact, we increased the amplitude of the SST anomaly up to about ±4 K. The resulting SST anomaly patterns are shown in Figure 9. They consist of two centers of action, one being placed in the northern North Atlantic off Newfoundland and south of Greenland and another one being located off the US coast.

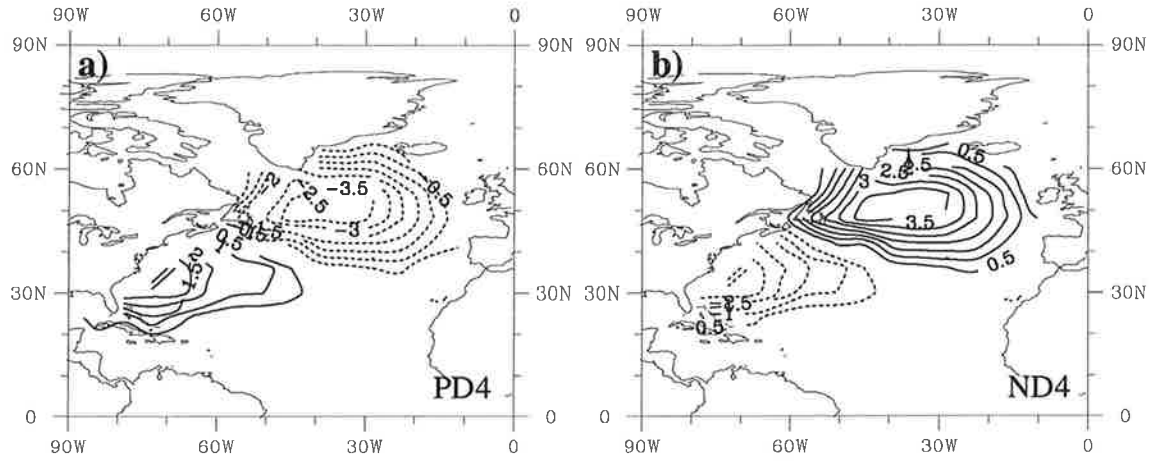

Figure 3: *The positive (a, PD4) and the negative (b, ND4) North Atlantic SST anomaly dipoles of the amplitude 4 K used in GCM experiments. Contour interval is .5 K. Zero line is omitted.*

By convention, we will refer to the SST anomaly of the amplitude 4 K and of the polarity as shown in Figure 9a with the positive SST center off the US coast and the negative center in the north of the North Atlantic, as "The Positive SST Dipole 4 K" (PD4). The SST anomaly of the opposite polarity will be called "The Negative SST Dipole 4 K" (ND4).

A SST anomaly of similar amplitude but of different spatial structure was used by Palmer and Sun (1985). In their study the SST anomaly was a monopole placed roughly in the middle between the SST centers of the dipole anomaly which is more similar to the second SST canonical pattern (Figure 9d). For completeness, we performed also several GCM runs with the SST anomalies (not shown) derived from the second observed SST canonical pattern. The amplitude of this anomaly was again chosen to be 4 *K*. Subtropical and subpolar SST centers presented in the second canonical pattern were excluded to have a monopole-type SST anomaly. The obtained SST anomalies will be referred as "the Positive Monopole Middle 4 K" (PMM4) and "the Negative Monopole Middle 4 K" (NMM4).

3.2 Monte-Carlo experiments

The nonstationary adaptation period of the atmospheric response was studied in Monte-Carlo simulations. For each polarity of the SST dipole anomaly, added to the SST climatology, we performed 20 independent 3-month GCM runs. Initial conditions used to start each individual integration have been taken from the control CNJLT run. The time interval between initial conditions was at least one month so that each 3-month integration can be considered as a statistically independent realization. The SST anomalies were "turned on" right at the beginning of integrations.

The corresponding fields of the control integration CNJLT were subtracted day-by-day from the results of anomaly runs to calculate anomalies of the atmospheric circulation. Then these anomalies were averaged over all 20 runs. As a result we had a 90-day mean evolution of the anomalous atmospheric flow for each polarity of the SST anomaly. We abbreviate them as the PD4MC ("Positive Dipole 4 K Monte-Carlo") and the ND4MC ("Negative Dipole 4 K Monte-Carlo") experiments. To prove the stability of the results, the evolution of atmospheric anomalies was also estimated separately for 10 arbitrary selected runs and for the other 10 runs.

Another two sets of Monte-Carlo simulations were made with SST anomalies of the same dipole structure but of the amplitude of 2 K to examine the linearity of the atmospheric response with respect to the amplitude of the SST anomaly. We will call these experiments the PD2MC and ND2MC runs.

3.3 Long term experiments

The stationary atmospheric response was examined in *long term* experiments. Two GCM runs each 30 months long were made for both the positive and the negative SST dipoles shown in Figure 9 added to the January climatology. We will call these runs in the following the PD4LT ("Positive Dipole 4 K Long Term") run and the ND4LT ("Negative Dipole 4 K Long Term") run. The climatological means averaged over 30 months for each anomaly run were compared with 30-month means of the control CNJLT run. Two 30-month integrations (the PD2LT and ND2LT runs) were made with 2 K SST dipoles.

Finally, we addressed the question about the relative importance of SST centers in the SST dipoles, or in other words, how sensible the atmospheric response is to the geographical location of SST anomalies. For this purpose we performed 4 GCM runs, each 24 months long, in which only one center of the SST dipole was retained. In Figure 9 the

positive SST monopoles placed at the US coast and the north of the North Atlantic are shown. We will refer to these integrations as the PMS4LT ("Positive Monopole South 4 K Long Term"), PMN4LT ("Positive Monopole North 4 K Long Term"), NMS4LT ("Negative Monopole South 4 K Long Term") and NMN4LT ("Negative Monopole North 4 K Long Term") runs. The labels "North" or "South" in the abbreviations of the experiments attribute either to the northern or to the southern center of the SST dipole which the GCM run was made with.

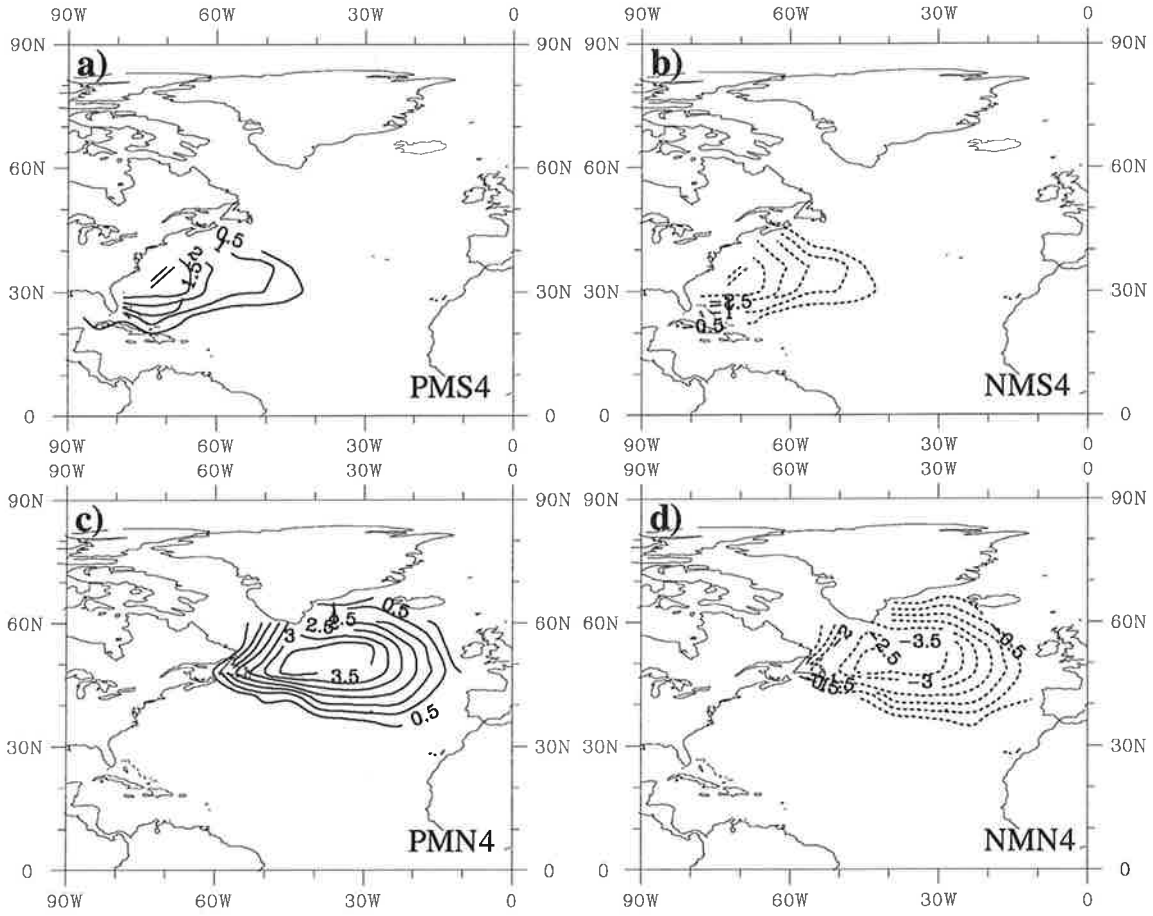

Figure 4: *The positive (a, PMS4; c, PMN4) and negative (b, NMS4; d, NMN4) SST monopoles of amplitude 4 K at the US coast (upper panels) and in the north of the North Atlantic (lower panels) used in the long term GCM experiments. Contour interval is .5 K. Zero line is omitted.*

In addition, the stationary atmospheric response to the SST anomaly derived from the second SST canonical pattern was examined in the PMM4LT ("Positive Monopole Middle 4 K Long Term") and NMM4LT ("Negative Monopole Middle 4 K Long Term") 24-month GCM runs.

3.4 The GCM experiments with variable SST

There were several 19-year GCM runs made with observed SST available for the analysis. These have already been described in detail by Graham et al. (1994) and Kharin (1994). Here we present only a brief summary of the GCM experiments. All experiments cover the period from January 1970 through December 1988. In the first experiment the observed sea surface temperatures from the NMC analysis were specified globally in 1981-1988 and near-globally in 1970-1980 for each month. We will refer to this integration as the GAGO ("Global Atmosphere - Global Ocean") run.

Another two GCM runs were driven by observed monthly mean SST prescribed in geographically limited areas to examine the relative importance of SST anomalies in the tropics and midlatitudes. One of these, the MOGA ("Midlatitude Ocean - Global Atmosphere") run, was conducted in the same manner as the GAGO experiment, except the SST anomalies were prescribed only in midlatitudes (northwards of $30°N$ and southwards of $30°S$) whereas in the tropics the climatological values of SST were used. In the other integration, the TOGA ("Tropical Ocean - Global Atmosphere") run, the observed SST was prescribed in the tropics ($25°S - 25°N$) and the climatological SST elsewhere. In addition, a 19-year CONTROL run with the climatological SST prescribed everywhere for each calendar month was also available. The CONTROL integration served as the reference run for estimating the internal atmospheric variability in the absence of external interannual SST forcing.

Monthly means in winter (December, January, February), altogether 57 months, were used in the analysis of the atmospheric variability. To verify the stability of the results to sampling errors we used also a five month winter season (November - March). The annual cycle defined as the 19-year mean for each calendar month was eliminated from the data.

The full list of the GCM experiments is provided in Table 9.

3.5 Statistical methods for the assessment of the model response

An univariate recurrence analysis (von Storch and Zwiers, 1988) was applied to estimate the statistical stability of the atmospheric response in the Monte-Carlo and long-term GCM experiments. This method compares two ensembles and establishes a measure of the strength of their discrimination. In the case of long term experiments one ensemble contains monthly means taken from the anomaly run and the other ensemble consists of

Abbrev.	The description of the GCM experiments	SST anomaly
PD4MC	Positive Dipole 4 K Monte-Carlo ECHAM2/T21 run	Figure 9a
ND4MC	Negative Dipole 4 K Monte-Carlo ECHAM2/T21 run	Figure 9b
PD2MC	Positive Dipole 2 K Monte-Carlo ECHAM2/T21 run	$\frac{1}{2}$(Figure 9a)
ND2MC	Negative Dipole 2 K Monte-Carlo ECHAM2/T21 run	$\frac{1}{2}$(Figure 9b)
CNJLT	Control Permanent January Long Term 30-month ECHAM2/T21 run	No SST anomalies
PD4LT	Positive Dipole 4 K Long Term 30-month ECHAM2/T21 run	Figure 9a
ND4LT	Negative Dipole 4 K Long Term 30-month ECHAM2/T21 run	Figure 9b
PD2LT	Positive Dipole 2 K Long Term 30-month ECHAM2/T21 run	$\frac{1}{2}$(Figure 9a)
ND2LT	Negative Dipole 2 K Long Term 30-month ECHAM2/T21 run	$\frac{1}{2}$(Figure 9b)
PMS4LT	Positive Monopole South 4 K Long Term 24-month ECHAM2/T21 run	Figure 9a
NMS4LT	Negative Monopole South 4 K Long Term 24-month ECHAM2/T21 run	Figure 9b
PMN4LT	Positive Monopole North 4 K Long Term 24-month ECHAM2/T21 run	Figure 9c
NMN4LT	Negative Monopole South 4 K Long Term 24-month ECHAM2/T21 run	Figure 9d
PMM4LT	Positive Monopole Middle 4 K Long Term 24-month ECHAM2/T21 run	not shown; derived from Figure 9d
NMM4LT	Negative Monopole Middle 4 K Long Term 24-month ECHAM2/T21 run	not shown; derived from Figure 9d
CONTROL	Control 19-year ECHAM2/T21 run	Observed SST climatology
GAGO	Global Atmopshere - Global Ocean 19-year ECHAM2/T21 run	Observed SST prescribed globally
MOGA	Middle Latitude Ocean - Global Atmosphere 19-year ECHAM/T21 run	Observed SST in extratropics
TOGA	Tropical Ocean - Global Atmosphere 19-year ECHAM/T21 run	Observed SST in the tropics

Table 1: *The list of the GCM experiments.*

monthly means of the control integration. In Monte-Carlo experiments a natural choice of these two ensembles is the time means of 20 anomaly runs and the corresponding time means taken from the control run.

At each grid point the distribution of the anomaly ensemble is compared with the distribution of the control ensemble. The recurrence analysis defines the probability that a sample, which might belong to either the anomaly or the control ensemble, will be classified correctly as a anomaly or control case. A formal definition of this probability and the way it is estimated from the data follows below.

Given two random variables $\mathbf{X}$ and $\mathbf{Y}$ with expectations μ_X and μ_Y the probability $p = prob\,(\mathbf{Y} > \mu_X) = 1 - prob\,(\mathbf{Y} < \mu_X)$ is calculated. If $p = 50\%$ then the random variables are not separated from each other. A large value such as $p = 95\%$ or a small value such as $p = 5\%$ indicates that the two random variables overlap only little. If $p = 95\%$ then any random realization of $\mathbf{Y}$ will very likely be larger than the mean of $\mathbf{X}$, and only 5% of all $\mathbf{Y}$-realizations will be smaller than this threshold. The opposite interpretation applies for $p = 5\%$.

If both random variables are Gaussian distributed with the same variance σ^2 then the probability p is given by $p = F_S^{-1}\left(\frac{\mu_X - \mu_Y}{\sigma^2}\right)$ with the standard normal (cumulative) distribution function F_S. In practical situations, as in the present study, the estimated means and the estimated standard deviation are used for the computation of p.

An alternative, and more conventional statistical approach would be a t-test. A shortcoming of this hypothesis testing approach is, however, the dependency of the result on the sample size. The level of recurrence, p, does not imply any statement on a statistical significance (like the rejection of the null hypothesis of equal means with a controlled certainty). Instead p is an *estimated measure of statistical stability.*

The canonical correlation analysis (CCA) with a limited number of EOFs (e.g. Barnett and Preisendorfer, 1987; Bretherton et al., 1992) was applied to the GAGO, MOGA and TOGA runs to obtain the best correlated patterns for two fields, one of which was a SST anomaly field and the other an atmospheric parameter. For each field we retained the first 5 principal components. Actually, the results of the CCA depends on the number of EOFs retained. Particularly, the canonical correlations tend to be artificially high if the number of EOFs is too large. One has to find a compromise between, on the one hand, the wish to retain as much explained variance and, consequently, as much of the potential signal, as possible, and on the other hand the requirement to eliminate the noise from the data. A number of preliminary tests with the CCA with different numbers of EOFs suggested that the first 4-5 leading EOFs

retained for each field could be appropriate in our case.

To estimate the level of canonical correlations that would appear in the CCA by chance, we produced for each run 200 CCAs with data time series which were randomly rearranged in time. The results of these simulations are collected into Appendix A.

Canonical correlations are obtained as the eigenvalues of a matrix which is a function of the covariance and autocovariance matrices of both fields. Due to sampling errors these matrices are estimated only approximately and that can lead to systematic errors in canonical correlations. Glynn and Muirhead (1978) proposed a technique for estimating such errors and deriving corrected unbiased values for canonical correlations. Appendix B gathers the results of this test.

4 The transient response in the Monte-Carlo experiments

This chapter considers the nonstationary transient period of the atmospheric response to SST anomalies during the adjustment phase in the first several months. First, a review of the response as envisaged by theoretical reasoning is offered. As an aid to understanding the results we applied simplified equations of relative vorticity and potential temperature including a heating term in quasi-geostrophic approximation (e.g. Pedlosky, 1979; Held, 1983). For simplicity we consider the atmospheric circulation on β-plane. The results can be easyly extended to spherical geometry (see e.g. Hoskins and Karoly, 1981).

The basic assumption of quasi-geostrophic theory is the smallness of the Rossby number $Ro = \frac{V}{fL}$, where V and L are typical horizontal velocity and length scales and f is the Coriolis parameter. To lowest order f may be replaced by f_0, so that the horizontal velocity $\mathbf{v}$ is approximately equal to the geostrophic velocity $\mathbf{v_g}$ which is non-divergent and determined by the streamfunction $\psi = \Phi/f_0$. To a higher order in Ro, only the vertical component of vorticity must be considered and the vertical advection, the nonlinear stretching and the twisting terms in the vorticity equation may be neglected, giving:

$$\frac{\partial}{\partial t}\nabla^2\psi + J(\psi, \nabla^2\psi + \beta y) = f_0\frac{\partial w}{\partial p}, \tag{1}$$

where ψ is the streamfunction, $\nabla^2\psi \equiv \xi$ is the geostrophic vertical component of relative vorticity, $f = f_0 + \beta y$ is the Coriolis parameter and $w \equiv dp/dt$ is the pressure velocity. The thermodynamical equation is modified by allowing the vertical advection act only on a standard potential temperature distribution Θ which is a function of p only:

$$\frac{\partial\theta}{\partial t} + J(\psi, \theta) = -\frac{d\Theta}{dp}w + \frac{\kappa}{R}\left(\frac{p_0}{p}\right)^{\kappa}\dot{Q}, \tag{2}$$

Here, θ is the potential temperature and $\dot{Q}$ is the diabatic heat rate per unit mass. R is the gas constant, p_0 is standard pressure on the surface and $\kappa = R/C_p$, C_p is specific heat content of dry air at constant pressure. The potential temperature can be excluded from (2) by means of the hydrostatic equation

$$\frac{\partial\Phi}{\partial p} \equiv f_0\frac{\partial\psi}{\partial p} = -\frac{R}{p}\left(\frac{p}{p_0}\right)^{\kappa}\theta \tag{3}$$

resulting in

$$\frac{\partial}{\partial t}\left(\frac{\partial \psi}{\partial p}\right) + J(\psi, \frac{\partial \psi}{\partial p}) = -\frac{f_0}{\delta^2} w - \frac{\kappa}{f_0 p}\dot{\mathcal{Q}}, \tag{4}$$

where

$$\delta^2 = -\frac{f_0^2 p}{R(p/p_0)^\kappa \frac{d\Theta}{dp}}. \tag{5}$$

Eliminating the vertical velocity w from (1) and (4) results in the equation of quasi-geostrophic potential vorticity

$$\frac{\partial q}{\partial t} + J(\psi, q) = -\frac{\partial \mathcal{D}}{\partial p}. \tag{6}$$

where

$$\mathcal{D} = \delta^2 \frac{\kappa}{p f_0}\dot{\mathcal{Q}}. \tag{7}$$

The (quasi-)potential vorticity q in (6) is

$$q = f_0 + \beta y + \nabla^2 \psi + \frac{\partial}{\partial p}\left(\delta^2 \frac{\partial \psi}{\partial p}\right). \tag{8}$$

The elliptic equation (8) can be solved if the distribution of q is given by (6) and boundary conditions are specified. The latter can be obtained from the thermodynamical equation (4) assuming in the absence of the orography $w = 0$ and $\dot{\mathcal{Q}} = \dot{\mathcal{Q}}_{p_0}$ at the surface layer $p = p_0$:

$$\frac{\partial}{\partial t}\left(\frac{\partial \psi}{\partial p}\right)_{p_0} + J(\psi, \frac{\partial \psi}{\partial p})_{p_0} = -\frac{\kappa}{f_0 p_0}\dot{\mathcal{Q}}_{p_0}. \tag{9}$$

At the top of the atmosphere the right side term in (9) is assumed to be zero.

Since the atmospheric circulation in mid-latitudes is dominated by the zonal flow, we linearize equations (1)-(2) about the zonal basic state U:

$$\frac{\partial \xi'}{\partial t} + U\frac{\partial \xi'}{\partial x} + \beta v' = f_0 \frac{\partial w}{\partial p}, \tag{10}$$

$$\frac{\partial \theta'}{\partial t} + U\frac{\partial \theta'}{\partial x} + v'\frac{\partial \bar{\theta}}{\partial y} = -\frac{d\Theta}{dp} w + \frac{\kappa}{R}\left(\frac{p}{p_0}\right)^\kappa \dot{\mathcal{Q}}', \tag{11}$$

or, in terms of the potential vorticity q

$$\underbrace{\frac{\partial q'}{\partial t}}_{I} + \underbrace{U\frac{\partial q'}{\partial x}}_{II} + \underbrace{v'\frac{\partial \bar{q}}{\partial y}}_{III} = -\frac{\partial \mathcal{D}'}{\partial p}. \tag{12}$$

In (11) $\bar{\theta}$ is related to U through the thermal wind relation

$$\frac{\partial \bar{\theta}}{\partial y} = \frac{f_0 p}{R}\left(\frac{p_0}{p}\right)^{\kappa}\frac{\partial U}{\partial p}. \tag{13}$$

If the basic state U does not depend on p then $\partial\bar{q}/\partial y = \beta$ and the term (III) in (12) is just the β-term. A scaling analysis provides the following ratios of the terms on the left side of

(12)

$$\frac{\partial q'}{\partial t} : U\frac{\partial q'}{\partial x} : \beta v' = \frac{1}{l\tau} : \frac{V}{l^2} : \frac{1}{LT}. \tag{14}$$

Here l and τ are spatial and time scales of the vorticity disturbances, V is typical horizontal velocity ($\simeq 20\ m/sec$), L is the spatial scale of the Coriolis parameter meridional gradient ($\simeq 10^4\ km$) and T is the time scale of the Earth rotation ($\simeq 1\ day$), respectively.

Equation (12) demonstrates clearly the dynamical mechanisms involved into the formation of the atmospheric response:

- On the first stage (first several days), all processes can be considered to be local. The spatial scale of vorticity anomalies is comparable to the spatial scale of SST anomalies ($l \simeq 1000\ km$) and is much smaller than the planetary scale ($l \ll L$). For $\tau \simeq 1\ day$ (14) results in

  $$(I) : (II) : (III) = 1.0 : 1.7 : 0.1 \tag{15}$$

  i.e. the β-term III may be neglected. Thus, equation (12) describes local generation of potential vorticity by external heat forcing over SST anomalies and advection of anomalous vorticity downstream with the mean flow U (terms I and II).

- With a time, the amplitude and the horizontal scale of vorticity anomalies l becomes larger. The β-term (III) in (12) cannot be more neglected. Indeed, taking $l \simeq 4000\ km$ and $\tau \sim 3\ days$ one obtains

  $$I : II : III = 0.8 : 1.1 : 1.0. \tag{16}$$

i.e. all terms are of the same order. For a large-scale atmospheric motion of equivalent-barotropic structure (i.e. $\psi = A(p)\hat{\psi}(x,y)$) there are no phase tilts in the vertical and the thermal advection is zero. Integrating (10), in vertical results in the linear equation of free planetary Rossby waves on β–plane:

$$\frac{\partial \hat{\xi}'}{\partial t} + \hat{U}\frac{\partial \hat{\xi}'}{\partial x} + \beta \hat{v}' = 0. \tag{17}$$

where $\hat{\varphi} = \int_0^{p_0} A(p)\varphi dp$.

- Finally, the atmosphere reaches the stationary equilibrium state in which the terms on the left side of (12), except of the temporal derivative of vorticity, plus diffusion and friction terms which are for simplicity omitted in (12) are balanced by thermal forcing on the right side.

The results of the Monte-Carlo simulations followed by the long term experiments in the next section will be presented according to the dynamical scheme of the atmospheric response behavior suggested above.

4.1 Generation and advection of potential vorticity

According to (14), in the very first moment ($\tau \ll 1$ day) all terms in (12), except $\partial q'/\partial t$, may be to first order neglected:

$$\frac{\partial q'}{\partial t} \approx -\frac{\partial \mathcal{D}'}{\partial p}. \tag{18}$$

Integrating (18) in vertical and substituting the boundary conditions derived from (9) we obtain

$$\frac{\partial}{\partial t}\nabla^2[\psi'] \approx 0 \tag{19}$$

where $[\psi'] = \frac{1}{p_0}\int \psi' dp$. Thus, the vertically integrated streamfunction anomaly $[\psi']$ in the vicinity of the thermal forcing over the SST anomaly remains constant in time at the first moment.

The anomalous heat flux from the ocean to the atmosphere over the warm SST anomaly is positive so that the overlaying air becomes warmer. The maximal amplitude of air temperature anomalies is expected to be at the surface. The hydrostatic equation (3) written for disturbances implies the negative pressure gradient $\frac{\partial \psi'}{\partial p} < 0$. Together with (19), this results in a negative height anomaly at the surface and a positive anomaly at higher levels.

Figure 9 illustrates 850 hPa temperature anomaly fields in the Northern Hemisphere and longitude-pressure temperature sections over the two SST anomaly centers after the first integration day in the Monte-Carlo simulations with the ± 4 K dipole SST anomalies. Left panels show temperature anomalies in the PD4MC run and right panels in the ND4MC run. Stipling indicates areas with estimated local level of recurrence $p \leq 10\%$ or $p \geq 90\%$. The signal in the temperature fields in the vicinity of the SST anomalies after one day is very stable. The maximum of air temperature anomalies exceeds 1.5 K and is located at the surface over the SST anomalies.

The corresponding anomalies of 300 hPa geopotential height together with longitude-pressure sections after one day are depicted in Figure 9. The anomaly structure is consistent with the theoretical predictions outlined above. Negative (positive) height anomalies of 4-5 gpm are located directly over the warm (cold) SST anomaly near the surface. In the middle troposphere at 300-500 hPa the height anomalies are of opposite sign. The near surface geopotential height anomalies over the south-western counterparts of the SST dipoles (longitude-pressure section at 36^oN in Figure 9b,e) penetrate deeper into the troposphere than those over the north-eastern SST anomalies (section at 53^oN in Figure 9c,e). This structure is consistent with air temperature anomalies shown in Figure 9. The air temperature anomalies over the SST anomalies at the US coast (Figure 9b,e) have larger vertical scale than the air temperature anomalies over the SST anomalies in the north of the North Atlantic (Figure 9c,f).

In the following few days the amplitude of atmospheric anomalies is growing and disturbances of vorticity are being transported by the mean flow eastwards according to (12) where only terms I are retained on the left side. Figure 9 demonstrates the atmospheric response averaged over the third day. Given a zonal wind of 20 m/sec and a time period of 2 days, simple estimations imply an advection of the signal to the distance of about 3.500 km. This corresponds approximately to the transport of atmospheric anomalies shown in Figure 9.

Since the mean zonal circulation at higher levels ($\sim$ 300 hPa) is stronger than at lower levels, the upper anomalies are advected farther to the east than the surface anomalies. This can be clearly seen in the longitude-pressure sections of geopotential height anomalies which reveals noticeable eastward tilt with height. The amplitude of the signal has doubled within two days attaining 10 gpm near the surface and at the 300 hPa level.

The meridional size of the height anomalies after 3 days is of the order of $3,000\ km$. Downstream of the main anomaly centers at 300 hPa one can already recognize the first

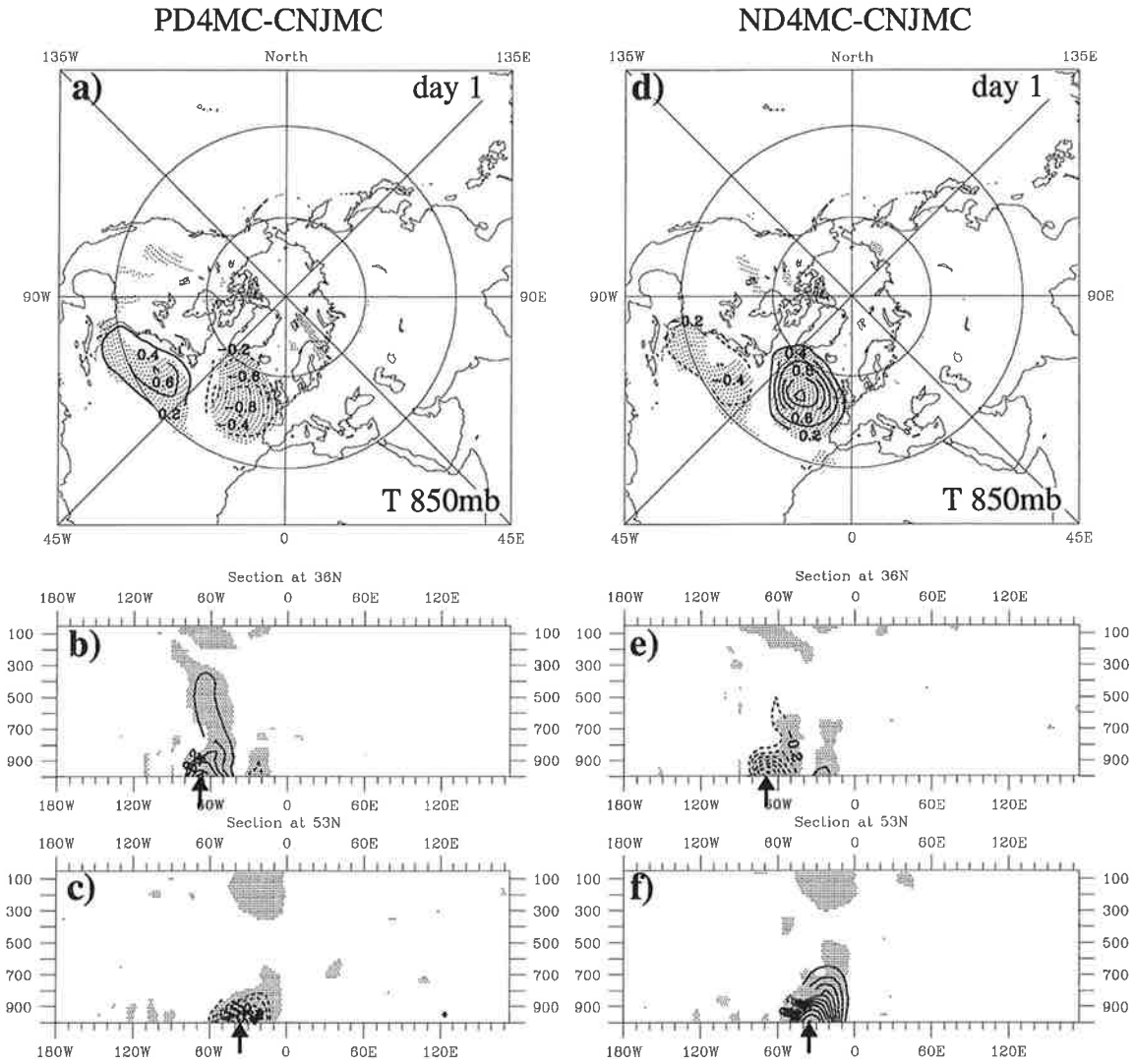

Figure 5: *850 hPa temperature anomaly fields in the Northern Hemisphere (a, d) and longitude-pressure sections of anomalous temperature over the SST anomaly centers at 36°N (b, e) and at 53°N (c, f) after the first integration day in the PD4MC experiment (left panels) and in the ND4MC experiment (right panels). Contour interval is 0.2 K. Zero line is omitted. Stipling represents the areas with estimated local level of recurrence $p \leq 10\%$ or $p \geq 90\%$. Arrows at the bottom of the section diagrams indicate the position of the SST anomalies.*

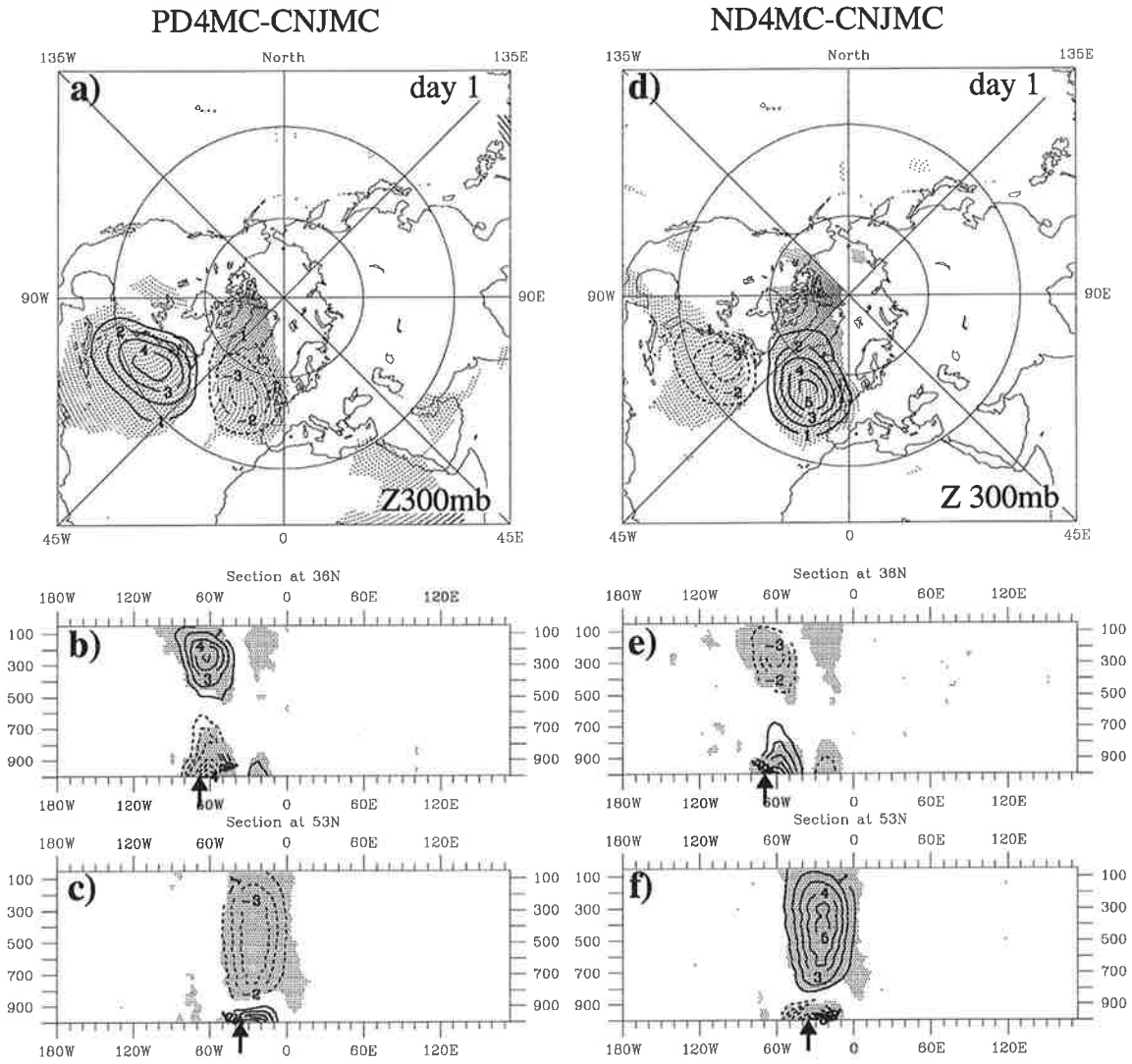

Figure 6: *300 hPa geopotential height anomaly fields in the Northern Hemisphere (a, d) and longitude-pressure sections of anomalous geopotential height over the SST anomaly centers at 36°N (b, e) and at 53°N (c, f) after the first integration day in the PD4MC experiment (left panels) and in the ND4MC experiment (right panels). Contour interval is 1 gpm. Zero line is omitted. Stipling represents the areas with estimated local level of recurrence $p \leq 10\%$ or $p \geq 90\%$. Arrows at the bottom of the section diagrams indicate the position of the SST anomalies.*

weak indications of the wave pattern propagating the signal eastwards. Particularly, small but relatively stable geopotential height anomalies of 2-3 gpm at 300 hPa with near equivalent-barotropic structure can be seen in the region over the Black Sea. The atmospheric signal is still symmetric with respect to the sign of the SST anomalies.

4.2 Rossby wave propagation

After a couple of days the horizontal scale of atmospheric anomalies becomes large enough so that the meridional changes of mean potential vorticity, or in terms of (12) the β-term III, cannot be more neglected. As indicated by (16), all 3 terms in (12) are needed to describe the dynamics of vorticity disturbances. Large-scale equivalent barotropic waves on β-plane are described by equation (17). On the sphere, the linearized equation of free barotropic Rossby waves in the Mercator projection ($x = a\lambda$ and $y = a\ln[(1+\sin\phi)/\cos\phi]$, where λ and ϕ are geographical longitude and latitude, respectively, and a is the Earth radius) has the same form as (17) (e.g. Hoskins and Karoly, 1981):

$$\left(\frac{\partial}{\partial t} + U_M\frac{\partial}{\partial x}\right)\left(\frac{\partial^2\psi}{\partial x^2} + \frac{\partial^2\psi}{\partial y^2}\right) + \beta_M\frac{\partial\psi}{\partial x} = 0, \tag{20}$$

where $U_M = U/\cos\phi$ and

$$\beta_M = \frac{2\Omega}{a}\cos^2\phi - \frac{d}{dy}\frac{1}{\cos^2\phi}\frac{d}{dy}(\cos^2\phi U_M) \tag{21}$$

is the meridional gradient of the absolute vorticity on the sphere times $\cos\phi$.

The dispersion relation for plane waves with zonal wave number k and meridional wave number l is

$$w = U_M k - \frac{\beta_M k}{k^2 + l^2}. \tag{22}$$

The group velocity $\mathbf{c_g} = (u_g, v_g)$ of Rossby waves is

$$u_g \equiv \frac{\partial w}{\partial k} = \frac{\omega}{k} + \frac{2\beta_M k^2}{(k^2+l^2)^2} = U_M + \beta_M\frac{k^2 - l^2}{(k^2+l^2)^2}, \tag{23}$$

$$v_g \equiv \frac{\partial w}{\partial l} = \beta_M\frac{2kl}{(k^2+l^2)^2}. \tag{24}$$

The wave energy propagates along a ray defined by the vector of the group velocity $\mathbf{c_g}$ with speed equal to $c_g \equiv |\mathbf{c_g}|$. The dispersion relation (22) does not depend on x and t

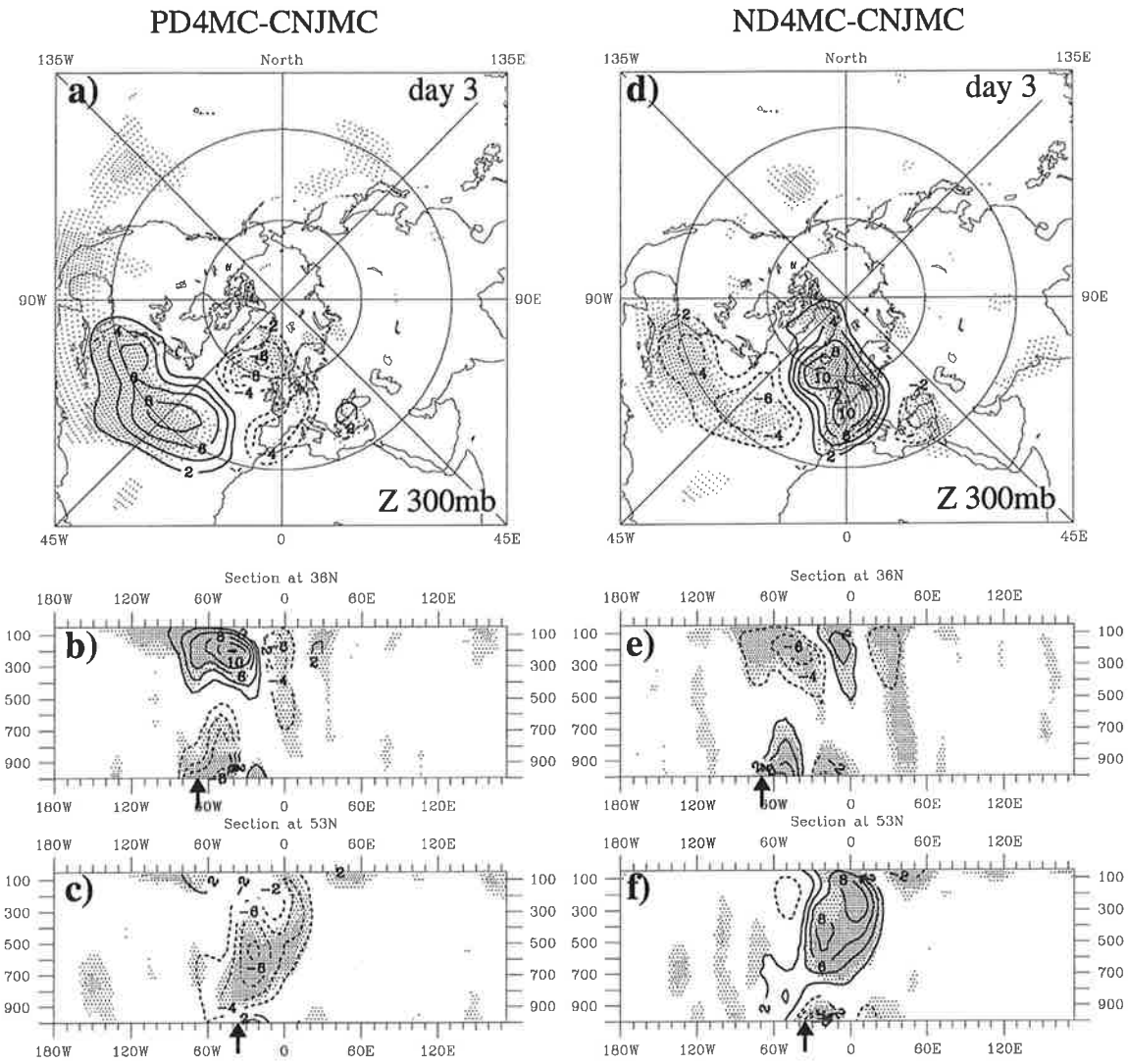

Figure 7: *300 hPa geopotential height anomaly fields in the Northern Hemisphere (a, d) and longitude-pressure sections of anomalous geopotential height over the SST anomaly centers at 36°N (b, e) and at 53°N (c, f) averaged over the third integration day in the PD4MC experiment (left panels) and in the ND4MC experiment (right panels). Contour interval is 2 gpm. Zero line is omitted. Stipling represents the areas with estimated local level of recurrence $p \leq 20\%$ or $p \geq 80\%$ (light) and $p \leq 10\%$ or $p \geq 90\%$ (middle). Arrows at the bottom of the section diagrams indicate the position of the SST anomalies.*

so that the zonal wave number k and w must be constant along a ray. The meridional wave number k varies along the ray such that (22) is satisfied everywhere.

For the particular case of stationary Rossby waves ($w = 0$) the group velocity is

$$c_g = 2\frac{k_s}{K_s}U_M, \tag{25}$$

where "stationary wavenumber" is

$$K_s \equiv (k_s^2 + l_s^2)^{1/2} = (\beta_M/U_M)^{1/2}. \tag{26}$$

Thus on the sphere, the energy propagates along a ray at a speed double that of the component of the basic flow in the direction of the ray. A propagation ray is given by

$$\frac{dy}{dx} = \frac{v_g}{u_g} = \frac{l}{k}, \tag{27}$$

and along a ray $k = constant$.

Wave amplitude and phase on the sphere can be estimated by WKB theory (see e.g. Hoskins and Karoly, 1981). Assuming that the meridional length scale l^{-1} is slowly varying, the WKB approximate form for the solution ψ is

$$\psi \sim l^{-1/2} exp\left[i(kx + \int^y l dy - wt)\right]. \tag{28}$$

For stationary solutions ($w = 0$), assuming that K_s is a decreasing function of latitude, l decreases according to (26) if the wave propagates northwards. The ray path becomes more zonally oriented and the streamfunction amplitude increases. For equatorwards propagating waves the WKB solution is again valid. At the critical latitude y_c at which $U_M = 0$ the ray tends to become meridional and the group velocity tends to zero. The WKB solution is not valid close to the critical line but a local analysis can be performed.

For a constant angular velocity flow $U_M = a\bar{\omega}$ the ray path is a great circle. Given the speed at the equator $\sim 20\ m/sec$ the fastest possible Rossby wave of zero frequency would propagate around the sphere in the absent of friction within $\simeq 10\ days$ and return to the vorticity source. The atmospheric friction, which is neglected in equation (12), decreases the amplitude of waves away from the source. Held (1983) demonstrated that for small values of the linear drag coefficient with a damping time scale of $r^{-2} = 20\ days$ the results of a linear barotropic model show a clear resonance structure and the atmospheric signal to the topographic forcing is near global. In opposite case of high friction ($r^{-2} = 5\ days$ the response is located near the vorticity source and little of the resonant structure remains.

Figure 9 shows the atmospheric response in the second week averaged over days 8-15 after introducing the SST anomalies. The amplitude of 300 hPa geopotential hight anomalies in the North Atlantic region exceeds 20 gpm. The signal have already reached the North Pacific region although the height anomalies here are weaker than in the North Atlantic and are less stable. The amplitude of the anomalies over the East Europe, first evidences of which could be already seen after 3 days in Figure 9, is significantly increased and is comparable with the amplitude of anomalies in the North Atlantic sector.

The atmospheric pattern of the atmospheric signals in Figure 9 resemble poleward and eastward wavetrain whose trajectory starts in the subtropical region of the North Atlanitc and goes through the northern North Atlantic to the european part of Russia. The amplitude of the geopotential height anomalies in moderate latitudes is larger than in subtropics of the North Atlantic, as expected from the theoretical considirations.

The atmospheric signal at this stage behaves near linearly with respect to the sign of SST anomalies. Particularly, over the northern part of the North Atlantic negative (positive) height anomalies are situated in the PD4MC (ND4MC) experiments. South of them in the subtropical North Atlantic at about 30^oN the sign of anomalies is opposite. The same is roughly valid for anomalies located over the european part of Russia. However, the signal in the PD4MC experiment is slightly stronger and more stable, with local values of recurrence $p \leq 10\%$ and $p \geq 90\%$, than in the ND4MC run where p-values are $\leq 20\%$ or $\geq 80\%$ only in few small areas. The equivalent-barotropic part dominates already in the vertical structure of anomali.

4.3 The establishment of the stationary response

After all nonstationary processes have been disappeared due to internal diffusion and atmospheric friction in the boundary layer the system reaches the stationary state. The linearized form of the equations

(1)-(2) for the stationary response is

$$U\frac{\partial \xi'}{\partial x} + \beta v' = f_0 \frac{\partial w}{\partial p}, \tag{29}$$

$$U\frac{\partial \theta'}{\partial x} + v'\frac{\partial \bar{\theta}}{\partial y} = -\frac{d\Theta}{dp}w + \frac{\kappa}{R}\left(\frac{p}{p_0}\right)^{\kappa}\dot{Q}'. \tag{30}$$

The full linear stationary solution consists of a partial solution ψ'_p and a homogeneous solution ψ'_h obtained for the zero heat rate $\dot{Q} = 0$, the sum of which satisfies the boundary conditions at the surface ($\omega = 0$ at $p = p_0$).

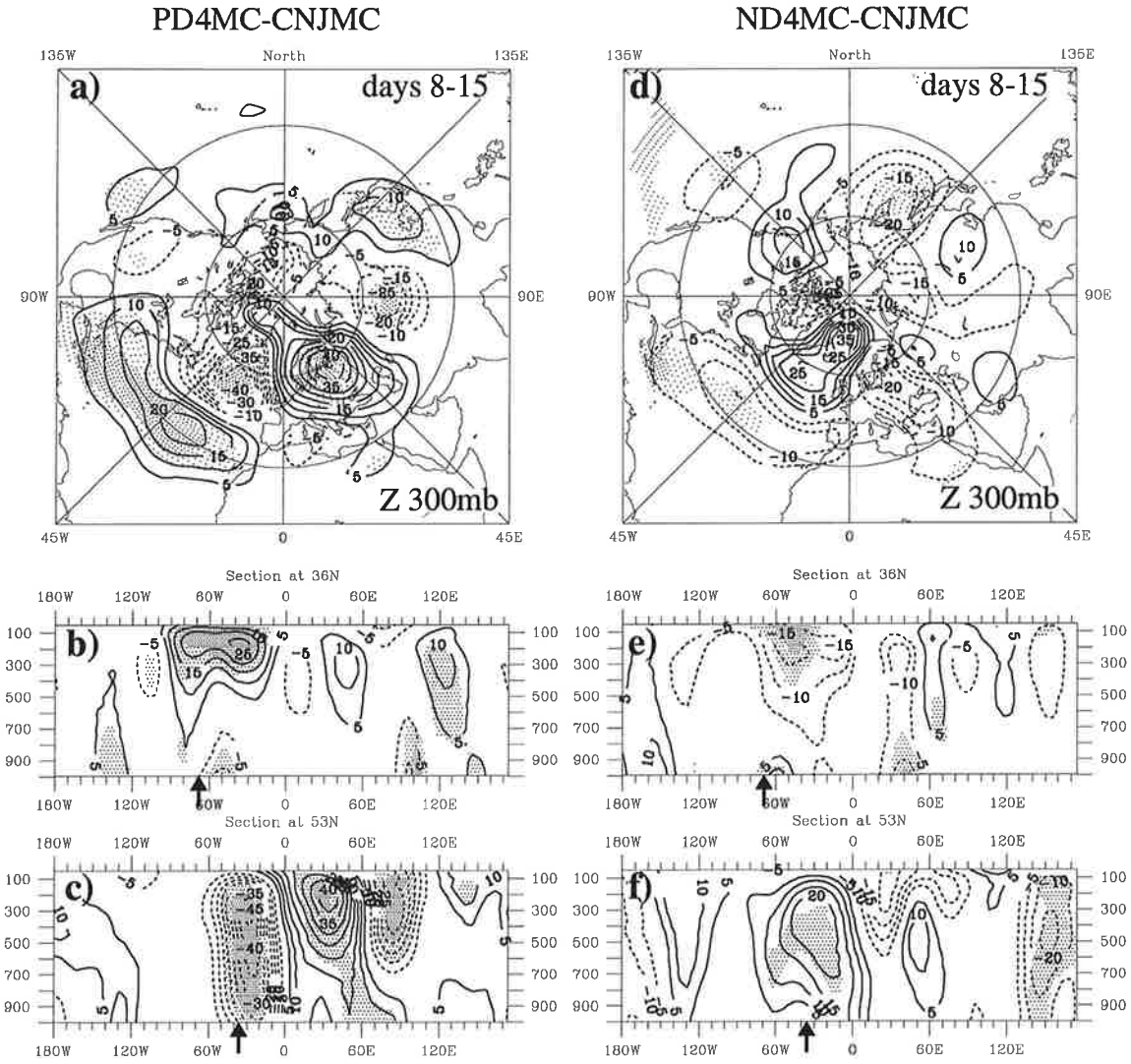

Figure 8: *300 hPa geopotential height anomaly fields in the Northern Hemisphere (a, d) and longitude-pressure sections of anomalous geopotential height over the SST anomaly centers at 36°N (b, e) and at 53°N (c, f) averaged over the days 8-15 in the PD4MC experiment (left panels) and in the ND4MC experiment (right panels). Contour interval is 5 gpm. Zero line is omitted. Stipling represents the areas with estimated local level of recurrence* $p \leq 20\%$ *or* $p \geq 80\%$ *(light) and* $p \leq 10\%$ *or* $p \geq 90\%$ *(middle). Arrows at the bottom of the section diagrams indicate the position of the SST anomalies.*

Whatever the relative importance of ψ'_p and ψ'_h in the vicinity of the heat source, the magnitude of the partial solution will decrease and the homogeneous solution will eventually dominate far away from the source. For localized heating source, the remote atmospheric response will be dominated by large scale equivalent barotropic Rossby waves with the appropriate local stationary wavelength and with maximum amplitude near the tropopause. Stationary barotropic solutions will be considered in more details in Section 7. Here we address only the properties of the partial solution ψ'_p.

The structure of the forced atmospheric response depends decisively on whether the heating is balanced by horizontal advection, either zonal or meridional, or mainly by adiabatic cooling. Scale considerations (e.g. Hoskins and Karoly, 1981) suggest that in the middle latitudes the limit in which horizontal advection dominates in the heat balance is more relevant.

Suppose that horizontal advection balances the diabatic heating. Expressing θ' and v' in terms of ψ' and replacing the meridional gradient of mean potential temperature by the vertical gradient of mean flow by means of the thermal wind relation, the the particular solution can be found in this case from

$$U\frac{\partial}{\partial x}\frac{\partial \psi'}{\partial p} - \frac{\partial \psi'}{\partial x}\frac{\partial U}{\partial p} = -\frac{\kappa}{f_0 p}\dot{Q}' \tag{31}$$

or

$$U^2\frac{\partial}{\partial x}\frac{\partial}{\partial p}\left(\frac{\psi'}{U}\right) = -\frac{\kappa}{f_0 p}\dot{Q}' \equiv \mathcal{R}' \tag{32}$$

The solution for the Fourier amplitudes $\tilde{\psi}'$ has the form:

$$\tilde{\psi}' = \frac{iU}{k}\int_o^p \frac{\tilde{\mathcal{R}}'}{U^2}dr. \tag{33}$$

From the linearized vorticity equation

$$ikU(K_s^2 - K^2)\tilde{\psi}' = f_0\frac{\partial \tilde{\omega}}{\partial p} \tag{34}$$

where $K_s^2 \equiv \beta/U$, one obtains for vertical velocity:

$$\tilde{\omega} = -\frac{ik}{f_0}\int_0^p U(K_s^2 - K^2)\tilde{\psi}'dr. \tag{35}$$

The consistency of this solution can be checked by noting whether or not $\tilde{\omega}\frac{d\Theta}{dp}$, with $\tilde{\omega}$ defined by (35), is indeed negligible in (30). If U can be taken as uniform within the source region (i.e. the second term in (31) is dropped out) and if $\dot{Q}$ can be assumed

to have simple vertical scale, $H_Q \propto |\dot{Q}/\frac{\partial \dot{Q}}{\partial z}|$ where $z = Hln(\frac{p_0}{p})$ that is smaller than or comparable to the scale height of the atmosphere, then from (33)

$$\tilde{\psi}' \propto \mathcal{R}' H_Q / kU, \tag{36}$$

and

$$\tilde{\omega} \propto \mathcal{R}' f_0^{-1} H_Q^2 (K_s^2 - K^2). \tag{37}$$

We have consistency if and only if

$$\epsilon \equiv \frac{d\Theta}{dp} f_0^{-1} H_Q^2 (K_s^2 - K^2) \ll 1. \tag{38}$$

In the extratropical lower troposphere, $K^2 \ll K_s^2$ for the planetary scale waves of interest. Taking into account this approximation, one finds for typical $N^2 \equiv g/\Theta \frac{d\Theta}{dz} = 1. \times 10^{-4} sec^{-2}$ that (38) reduces approximately to $(H_Q/6\ km)^2 \ll 1$.

If U cannot be taken as constant with height this consistency condition will be altered. In particular, if the second rather the first term in (31) dominates, that is if $H_U \propto |U/\frac{\partial U}{\partial z}| \ll H_Q$ within the region of diabatic heating, then $\tilde{\psi}' \propto \mathcal{R}' H_U / kU$, and H_U replaces H_Q in (38). For the not untypical parameters 5 m/sec at the surface and linearly increasing to 20 m/sec at 10 km, $H_U \sim 3\ km$ in the lower troposphere, so we still expect the consistency condition to be reasonably well satisfied for extratropical lower tropospherical heating.

The partial solution always possesses a low pressure center placed a quarter wavelength downstream of the heating maximum. (We assume for simplicity that $\tilde{\mathcal{Q}}$ has no phase variation with height). Whether it is cold or warm low depends on the vertical scale of the heat source. If $H_Q \ll H_U$, so that zonal temperature advection is dominant, then air in the low pressure system downstream is warm. If meridional advection is dominant, $H_U \ll H_Q$, then the low is warm (cold) if $\dot{Q}$ decreases (increases) with height.

The scaling arguments (see e.g. Held, 1983) suggest that within the source region $|\psi_h/\psi_p| \propto \epsilon/(m \min(H_Q, H_U))$, where m is the local vertical wavenumber of $\tilde{\psi}'$. If ψ_p does dominate in the source region, then one should see a gradual transition from ψ_p to ψ_h with height. One can show that for the long propagating waves this implies a rapid westward phase shift with height i.e. the total solution is baroclinic in the vicinity of the heating.

The atmospheric response averaged over two weeks in days 31-45 is depicted in Figure 9. The atmospheric response in the PD4MC experiment has a well developed structure in the North Atlantic/European sector. The atmospheric signal in this region is quite stable with recurrence values $p \leq 10\%$ and $p \geq 90\%$. A strong negative height anomaly of the amplitude over 140 gpm is placed in the northern part of the North Atlantic with the center south of Iceland. Two positive centers are situated south and south-east of the negative anomaly. Moderate and less stable anomalies are found over the North America and over the North Pacific.

The longitude-pressure cross-sections (Figure 9b,c) display the equivalent barotropic structure of the response downstream of the SST anomalies. Moderate negative height anomalies at lower levels and statistically stable positive anomalies at higher levels are found east of the warm SST anomaly in the PD4MC experiment (Figure 9b). Thus, the structure of the response in the vicinity of the positive SST anomaly is roughly consistent with the structure of the baroclinic partial stationary solution predicted from the quasi-geostrophic theory.

The atmospheric response in the ND4MC run after one month (Figure 9d-f) is much weaker than in the PD4MC experiment. The nonlinear effects become to be substantial making the signal nonsymmetric in the PD4MC and ND4MC experiments. The well developed positive height center over the northern part of the North Atlantic found in days 8-15 (Figure 9d-f) which was even more stronger in the following two weeks (not shown) practically disappeared. A negative height anomaly placed previously over the Black Sea is situated now over the West Europe with the center over the North Sea. The signal in the ND4MC experiment after one month is substantially less stable than in the PD4MC run, though the negative anomaly over Europe is still moderately stable with recurrence level $p \leq 20$.

Finally, we demonstrate in Figure 9 the eventual response averaged over the last two months of the integration (days 31-90). The spatial structure of the anomalous patterns remains near the same as in days 31-45 shown in Figure 9, though the amplitude of the signal is smaller. The response in the PD4MC experiment is still statistically stable with local recurrence levels $p \leq 10\%$ and $p \geq 90\%$ in the North Atlantic / European sector. The stationary signal in the ND4MC run is weak and not statistically stable. The asymmetrical behavior of the stationary atmospheric signal with respect to the sign of the SST anomalies has been also confirmed by the long term experiments which will be discussed in Section 5.

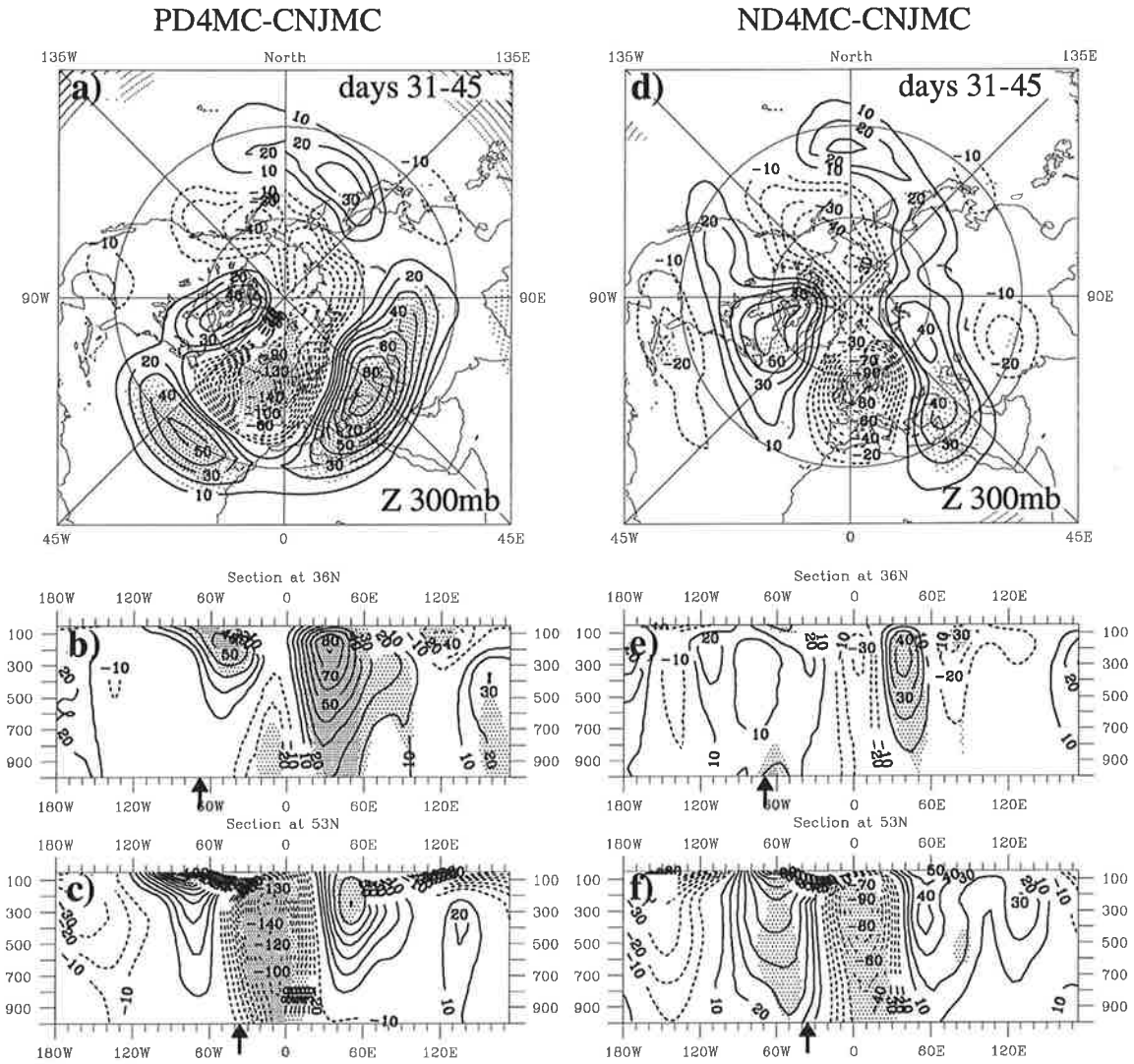

Figure 9: *300 hPa geopotential height anomaly fields in the Northern Hemisphere (a, d) and longitude-pressure sections of anomalous geopotential height over the SST anomaly centers at 36^oN (b, e) and at 53^oN (c, f) averaged over the days 31-45 in the PD4MC experiment (left panels) and in the ND4MC experiment (right panels). Contour interval is 10 gpm. Zero line is omitted. Stipling represents the areas with estimated local level of recurrence $p \leq 20\%$ or $p \geq 20\%$ (light) and $p \leq 10\%$ or $p \geq 90\%$ (middle). Arrows at the bottom of the section diagrams indicate the position of the SST anomalies.*

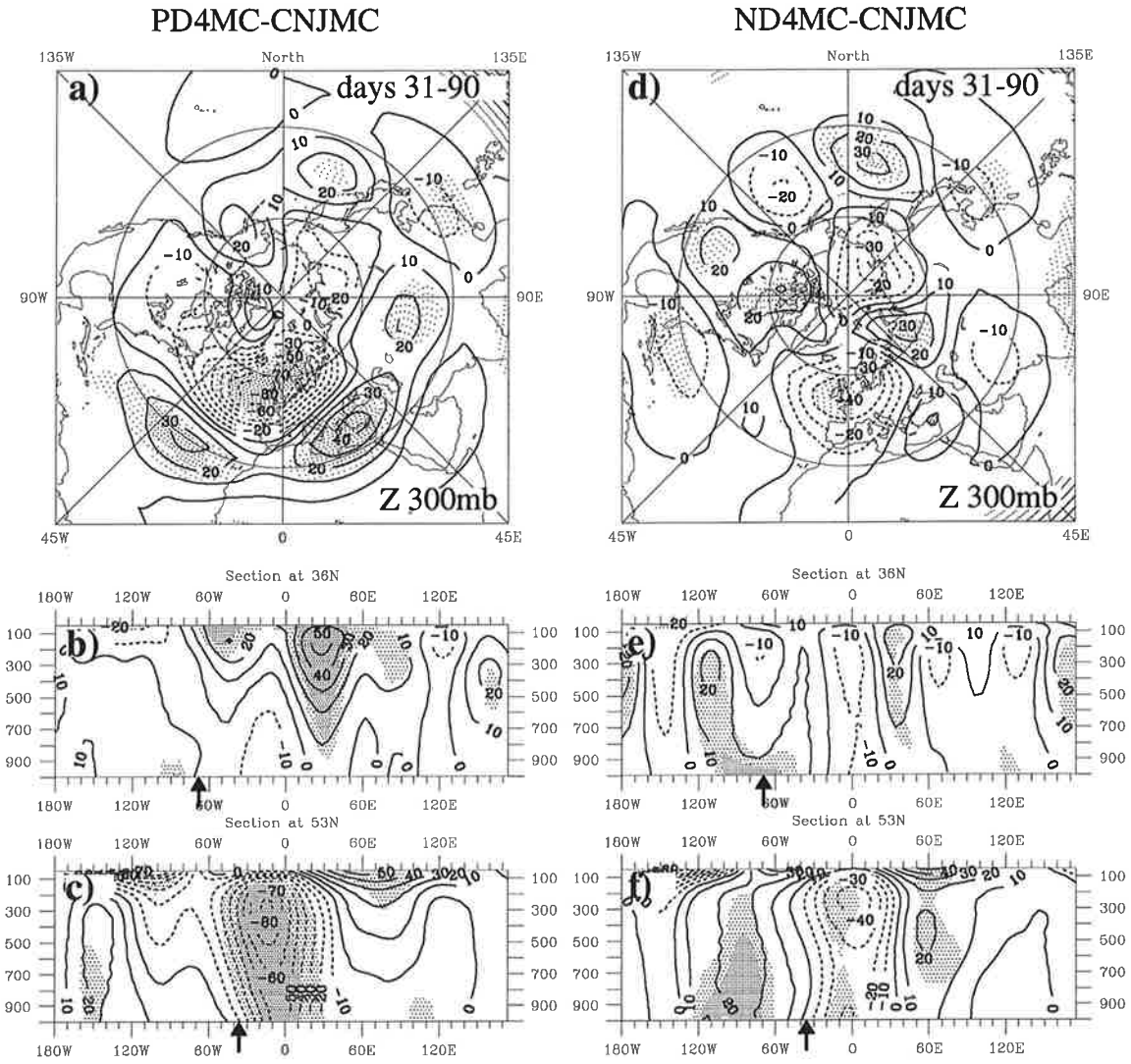

Figure 10: *300 hPa geopotential height anomaly fields in the Northern Hemisphere (a, d) and longitude-pressure sections of anomalous geopotential height over the SST anomaly centers at 36°N (b, e) and at 53°N (c, f) averaged over the days 31-90 in the PD4MC experiment (left panels) and in the ND4MC experiment (right panels). Contour interval is 10 gpm. Stipling represents the areas with estimated local level of recurrence $p \leq 20\%$ or $p \geq 80\%$ (light) and $p \leq 10\%$ or $p \geq 90\%$ (middle). Arrows at the bottom of the section diagrams indicate the position of the SST anomalies.*

4.4 Monte-Carlo simulations with 2 K SST anomalies

The atmospheric response obtained in Monte-Carlo simulations with ±2 K SST anomalies is almost at all stages about half of that obtained from the experiments with ±4 K SST anomalies. Especially good linearity of the results was found in the first month. Particularly, we show in Figure 9 the transient height response in days 8-15 days in the PD2MC and ND2MC experiments. Compared to the PD4MC/ND4MC runs the anomalies in the North Atlantic and over Europe are approximately of the same structure but roughly of the half amplitude. Over and eastwards of the warm (cold) SST anomalies the positive (negative) 300 hPa geopotential height anomalies are found. The atmospheric signal to ±2 K SST anomalies is hidden to much extent by high natural variability and is statistically not very stable.

The established response to ±2 K SST anomalies in the last two months differs from the stationary response in Monte-Carlo experiments made with ±4 K SST anomalies. Since the stationary atmospheric reaction in the Monte-Carlo simulations appeared to be very similar to the response obtained in the long term experiments, SST amplitudes, we will discuss the differences between the stationary responses to the SST anomalies of the both amplitudes in the following section.

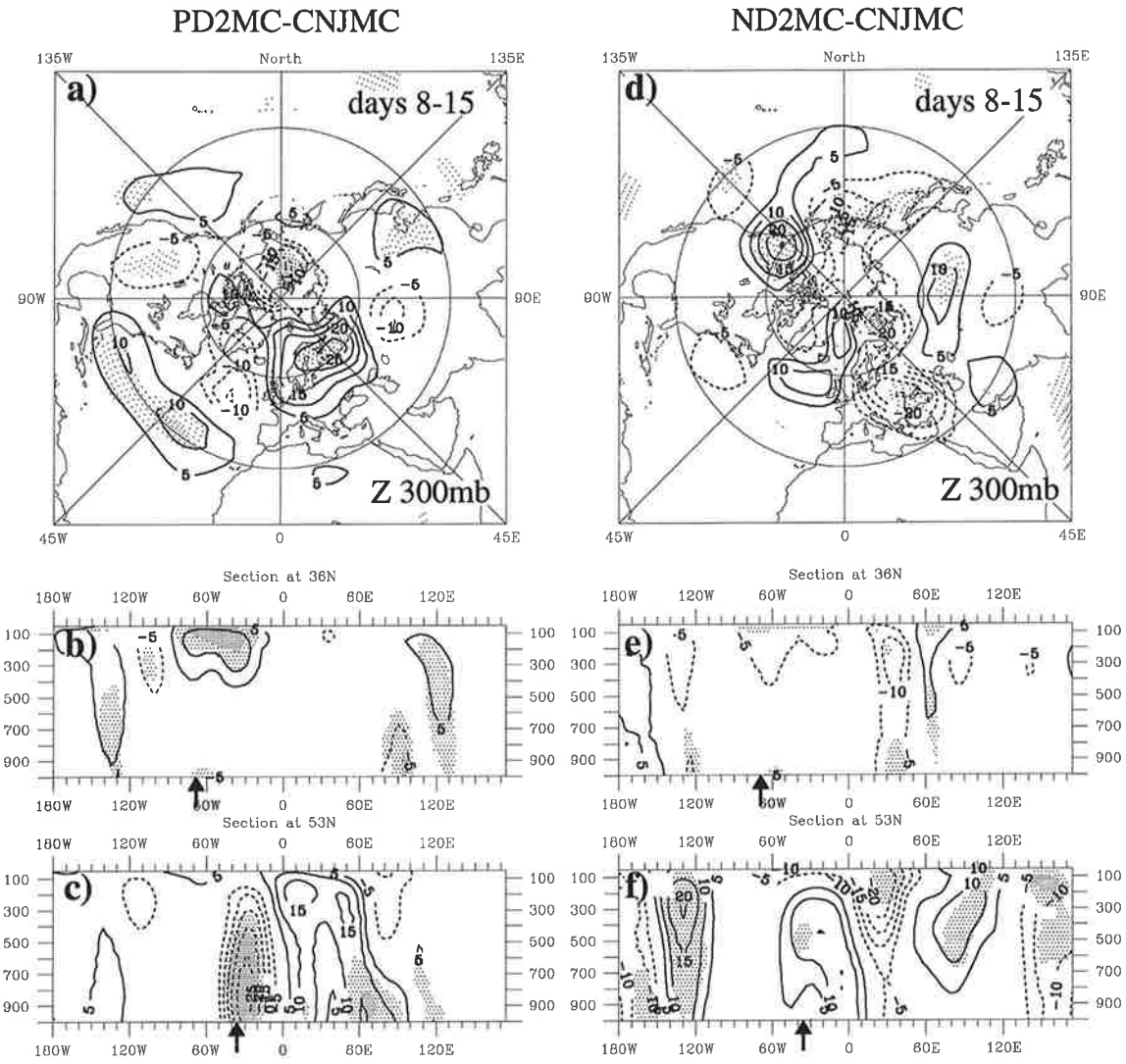

Figure 11: *300 hPa geopotential height anomaly fields in the Northern Hemisphere (a, d) and longitude-pressure sections of anomalous geopotential height over the SST anomaly centers at 36°N (b, e) and at 53°N (c, f) averaged over the days 8-15 in the PD2MC experiment (left panels) and in the ND2MC experiment (right panels). Contour interval is 10 gpm. Zero line is omitted. Stipling represents the areas with estimated local level of recurrence $p \leq 20\%$ or $p \geq 80\%$ (light) and $p \leq 10\%$ or $p \geq 90\%$ (middle). Arrows at the bottom of the section diagrams indicate the position of the SST anomalies.*

5 The atmospheric response in the long term experiments

In this section the stationary atmospheric response in the GCM to different SST anomalies in the North Atlantic is described. Two aspects of the response are examined. First, the results of the long term experiments made with dipole SST anomalies of different amplitudes are presented and the linearity of the signal with respect to the sign and the amplitude of SST anomalies is discussed. Then, the dependence of the atmospheric response on the geographical location of the heat source is examined. This question has been addressed by several authors who studied the atmospheric response to adiabatic anomalous heating in different regions in the tropics (e.g. Simmons, 1982; Simmons et al., 1983) and in middle latitudes as well (Navarra, 1990). They demonstrated that the amplitude of the atmospheric response and partly its spatial structure depends on the location of the heat source.

The theoretical backgrounds of the model stationary response have been already considered in the previous section on the example of the quasi-geostrophic model linearized about the zonal flow . The full stationary solution in the linear model is composed of the partial solution, which influences mainly the structure of the response in the vicinity of the heat source, and the homogeneous solution which dominates far away from the heating. The partial solution is of baroclinic structure and is rather insensitive to fine details of the basic flow. The properties of the large scale equivalent-barotropic homogeneous solution depend, on the contrary, crucially on the global structure of the basic flow. The detailed analysis of stationary barotropic solutions will be presented in Section 7.

5.1 The stationary response to 4 K dipole SST anomalies

Figure 9 shows 30-month mean anomaly fields of 300 hPa geopotential height over the Northern Hemisphere and two longitude-pressure sections made over the SST anomaly centers in the PD4LT and ND4LT runs. A relatively strong atmospheric signal is found only in the PD4LT run. As expected, the atmospheric response in this experiment is comparable with the stationary atmospheric response averaged over the last one or two months in the Monte-Carlo experiments (cg. Figure 9). Anomalies of large amplitudes are located in the North Atlantic / Southern Europe sector. A negative geopotential height anomaly is placed in the northern part of the North Atlantic with amplitude

over 70 gpm in the center south of Iceland. Positive height anomalies are located over the central subtropical North Atlantic and over Southern Europe. The anomalies in these three centers are moderately stable with local levels of recurrence $p \leq 20\%$ and $p \geq 80\%$. Another not very stable positive height anomaly is placed over the North American continent. In the north-western part of the North Pacific and in the polar regions moderate and slightly stable negative anomalies with $p \leq 30\%$ are found.

The atmospheric response in the ND4LT experiment is, opposite to the PD4LT run, weak and statistically not very stable. Local recurrence values $p \leq 30\%$ or $p \geq 70\%$ are found only in a few small areas. The positive geopotential height anomaly with maximal values of 40 gpm at 300 hPa in the northern part of the North Atlantic is located approximately in the same region as the negative anomaly in the PD4LT run. It is however not statistically stable. Obviously, nonlinear effects play a significant role for the atmospheric response in the GCM on SST anomalies of order 4 K.

The longitude-pressure geopotential height sections indicate that the atmospheric response is to high extent equivalent barotropic in the main body of the troposphere in the both runs. In the vicinity of the SST anomalies, however, baroclinic features such as westward tilts with height are noticeable. A low pressure system is found over and downstream of the positive SST anomaly in the PD4LT run (Figure 9b) whereas at higher levels positive height anomalies are is located. The same but with opposite sign is valid for the response in the vicinity of the negative SST anomaly in the ND4LT run (Figure 9b). This corresponds exactly to the structure of the partial solution expected from the linear quasi-geostrophic model under the condition that near surface anomalous heating is compensated by horizontal advection.

The same theoretical arguments can be applied also to the local atmospheric response on SST anomalies placed east of Newfoundland. However the barotropic part of the full stationary solution, which is basically due to a remote response to the SST anomalies placed at the US coast, is in this region so large that the height anomalies have the same sign throughout the whole atmosphere. But the westward tilt of anomalies with height is still evident over the northern counterparts of the SST anomaly dipoles.

To have an idea about the stability of the stationary response in the long term experiments we computed the anomalies of 300 hPa geopotential height in the PD4LT and ND4LT runs averaged separately for the first and for the second 15 months (Figure 9). One can see that the 15-months means still reveals relatively high variability. The response is extremely strong and very stable in the first 15 months of the PD4LT

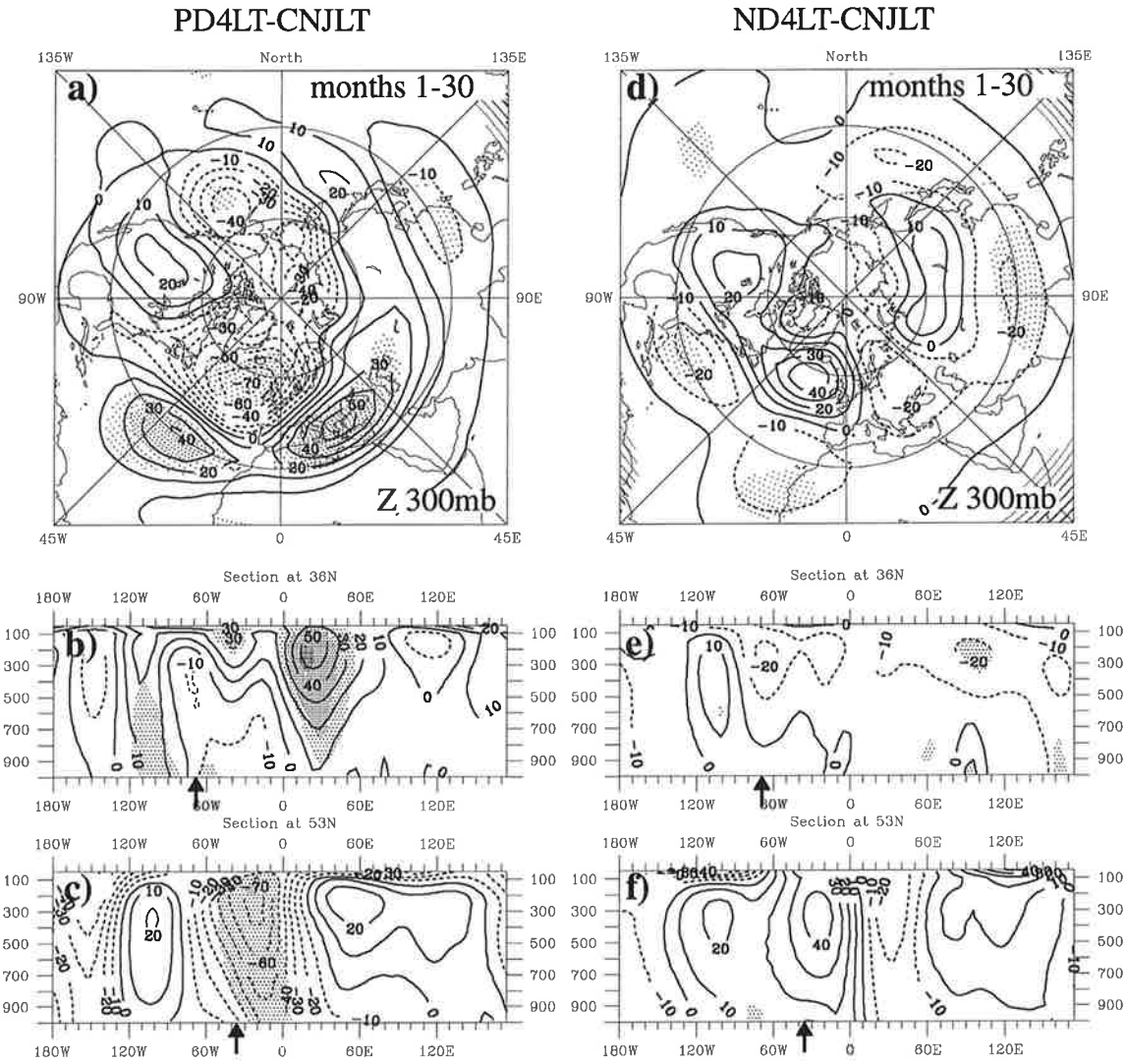

Figure 12: *300 hPa geopotential height anomaly fields in the Northern Hemisphere (a, d) and longitude-pressure sections of anomalous geopotential height over the SST anomaly centers at 36°N (b, e) and at 53°N (c, f) averaged over the months 1-30 in the PD4LT experiment (left panels) and in the ND4LT experiment (right panels). Contour interval is 10 gpm. Stipling represents the areas with estimated local level of recurrence $p \leq 30\%$ or $p \geq 70\%$ (light), $p \leq 20\%$ or $p \geq 80\%$ (moderate), $p \leq 10\%$ or $p \geq 90\%$ (heavy). Arrows at the bottom of the section diagrams indicate the position of the SST anomalies.*

run and is weaker in the second 15 months. In the ND4LT run the atmospheric signal is relatively weak in both subperiods. Positive geopotential height anomalies are located predominantly in the northern North Atlantic (Figure 9c,d). In the first 15-month period a positive height anomaly is found also over the North american continent. Negative anomalies are placed in subtropical regions and over the east and south of Europe.

The main features of the atmospheric response remain near the same in both halves of the integration period. Particularly, negative height anomalies are found over the northern parts of the both oceans in both subperiods in the PD4LT run, except a small area over Greenland with positive values in the second 15-month period (Figure 9a,b). Positive anomalies are located over the subtropical North Atlantic and in the latitude band $30^oN - 60^oN$ over Eurasia.

The surface atmospheric 30-month mean response in the PD4LT and ND4LT experiments is depicted in Figure 9. The anomaly fields of SLP (Figure 9a,d), total (sensible + latent) heat flux through the air/sea surface (Figure 9b,e) and precipitation (Figure 9c,f) are shown. The surface anomalous circulation in the PD4LT run transports cold air from the northern regions over the positive SST anomaly placed at the US coast. In this region the largest anomalies of heat flux (over 140 W/m^2) and of rainfall (over 2 cm/day) are located. The low in the North Atlantic sector is over 5 mb strong and is shifted slightly to the east of the with respect to the negative center at 300 hPa. Negative SLP anomalies in the PD4LT run are found, similarly to 300 hPa geopotential height anomalies, also over the northern North Pacific and in the polar regions around the North Pole.

In the ND4LT run small positive SLP anomalies of 1-2 mb are placed in the latitude band $40^oN - 60^oN$ over the North Atlantic sector with centers over the north-east of the North American continent and over the northern Great Britain. Negative SLP anomalies are found over the North Pacific and over the northern regions of Russia. All extratropical SLP anomalies in the ND4LT run are not very stable. Anomalous heat fluxes are located predominantly over the SST centers. The anomaly fields of total precipitation (Figure 9c,f) indicate that most of anomalous latent heat flux is released over the SST anomalies.

Some authors (e.g. Palmer and Sun, 1985; Lau and Nath, 1990) suggested that transient eddy forcing of the mean flow plays a substantial role in the atmospheric response to SST anomalies. Lau (1988) showed on the base of observational data that the barotropic forcing by synoptical scale disturbances are positively correlated with the monthly averaged flow pattern. A diagnostic technique which has proven to be useful for

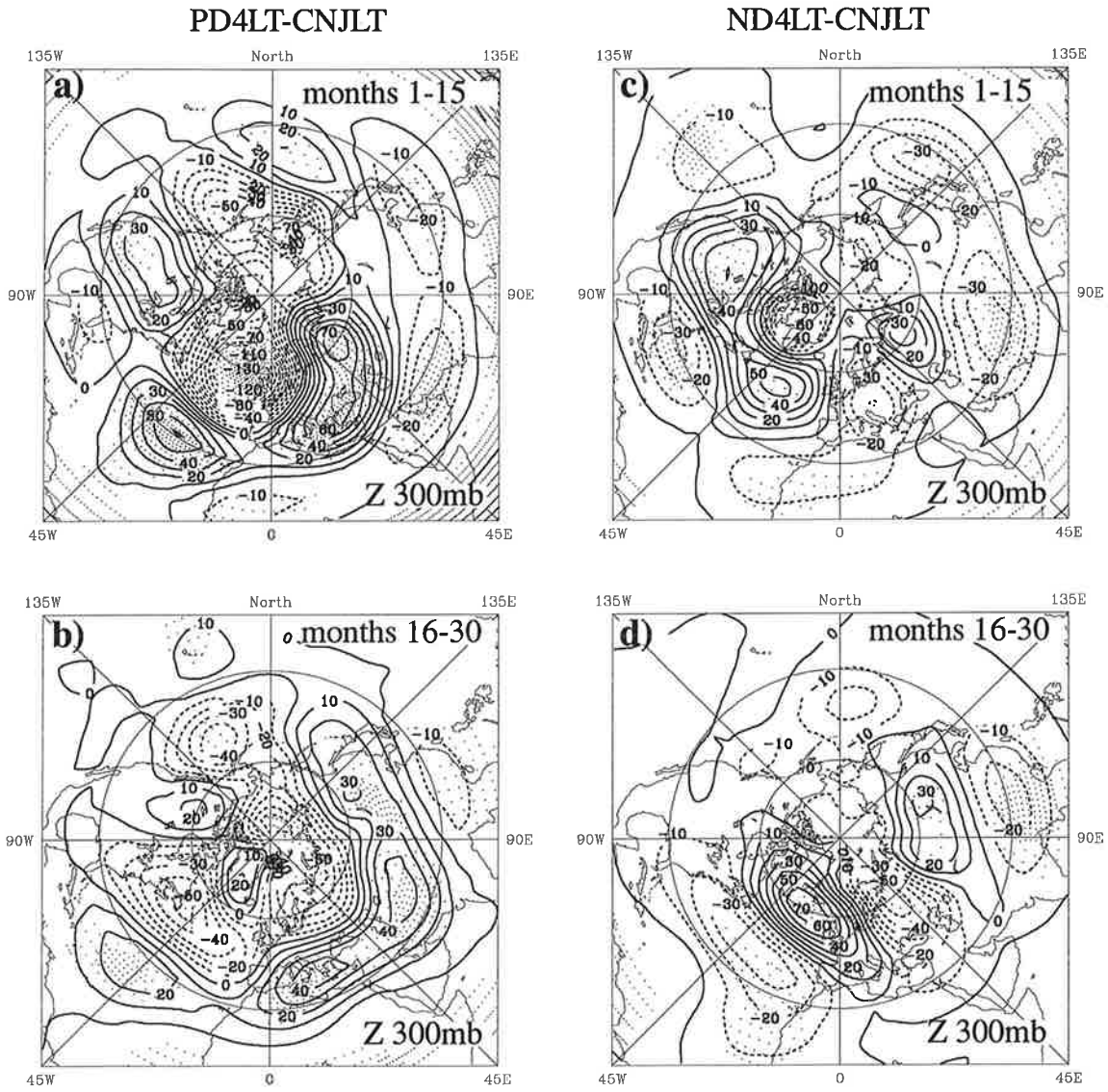

Figure 13: *300 hPa geopotential height anomaly fields in the Northern Hemisphere averaged over the months 1-15 (a,c) and 16-30 (b,d) in the PD4LT experiment (left panels) and in the ND4LT experiment (right panels). Contour interval is 10 gpm. Stipling represents the areas with estimated local level of recurrence* $p \leq 30\%$ *or* $p \geq 70\%$ *(light),* $p \leq 20\%$ *or* $p \geq 80\%$ *(moderate),* $p \leq 10\%$ *or* $p \geq 90\%$ *(heavy).*

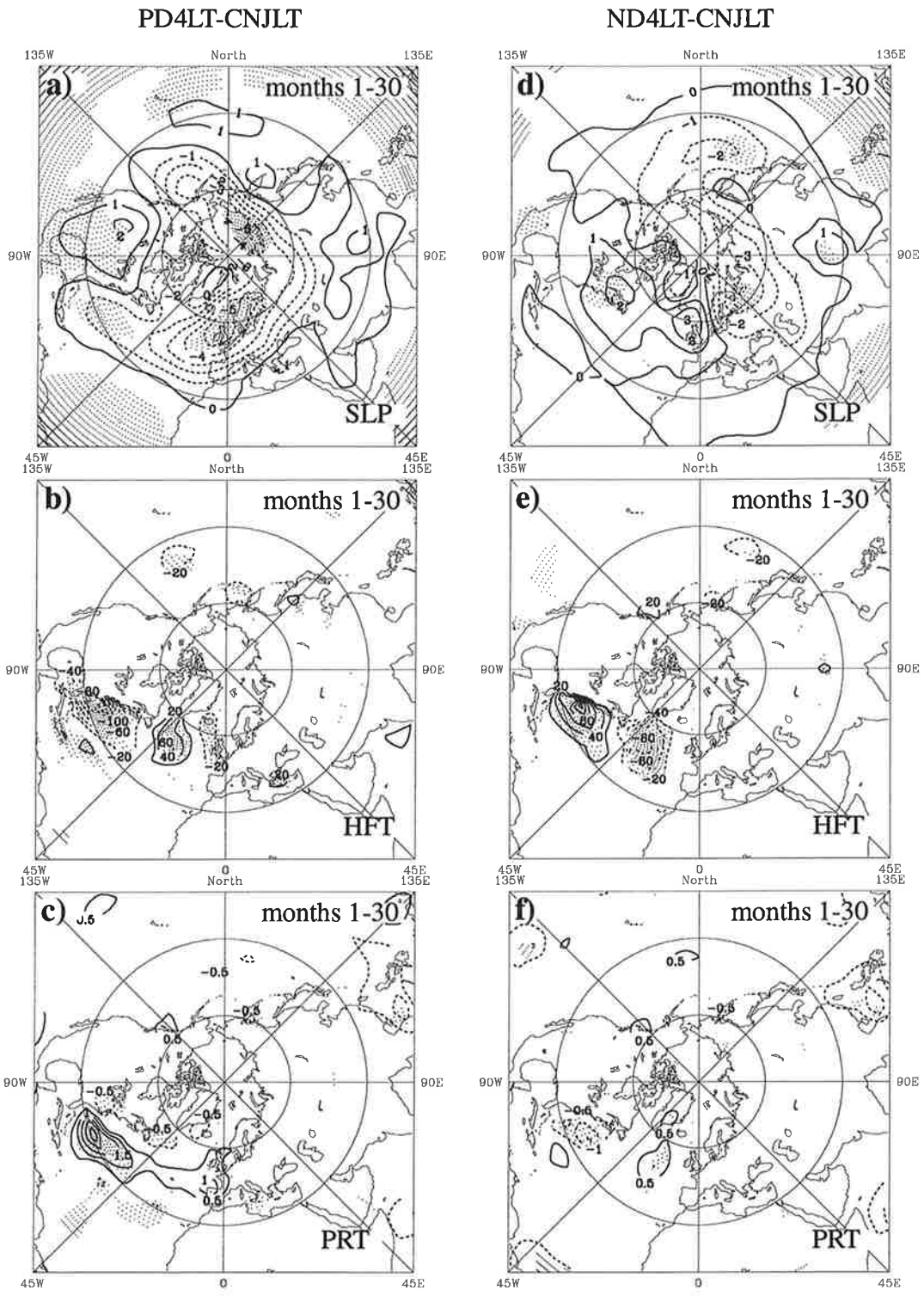

Figure 14: *30-month mean anomaly field of SLP (a,d; contour interval 1 mb), total (sensible + latent) heat flux through air/sea surface (b,e; contour interval 20 W/m^2) and total precipitation (c,f; contour interval .5 cm/day) in the Northern Hemisphere in the PD4LT run (left panels) and in the ND4LT (right panels). Positive values of heat flux anomalies stand for anomalous heat flux from the atmosphere into the ocean. Stipling represents the areas with estimated local level of recurrence $p \leq 30\%$ or $p \geq 70\%$ (light), $p \leq 20\%$ or $p \geq 80\%$ (moderate), $p \leq 10\%$ or $p \geq 90\%$ (heavy).*

delineating the quantitative aspects of local eddy-mean interactions is the geopotential tendency approach outlined in Lau and Holopainen (1984). By examining climatological eddy statistics they showed that the geopotential tendency in the upper troposhere is mostly determined by eddy vorticity fluxes. These authors further reported that the vertical variation of the geopotential height tendency associated with vorticity fluxes is characterized by an equivalent barotropic structure, with strongest amplitude in the upper troposphere.

To estimate the effect of baroclinic eddies (2.5-6 days) in the GCM experiments we computed tendencies of geopotential height at 300 hPa due to barotropic transient eddy forcing according to Lau (1988). This is a simplified two-dimensional form of the three-dimensional formulation of Lau and Holopainen (1984):

$$\frac{\partial Z_{eddy}}{\partial t} = \frac{f}{g}\nabla^{-2}\pi \tag{39}$$

where

$$\pi \equiv \frac{1}{a^2\cos\phi}\frac{\partial}{\partial\phi}\frac{1}{\cos\phi}\frac{\partial}{\partial\phi}\cos^2\phi\,\overline{u'v'} - \frac{1}{a^2\cos^2\phi}\frac{\partial^2}{\partial\lambda^2}\overline{u'v'} + \frac{1}{a^2\cos^2\phi}\frac{\partial^2}{\partial\lambda\partial\phi}\cos\phi(\overline{u'^2} - \overline{v'^2}) \tag{40}$$

is the convergence of the transient eddy vorticity fluxes.

The resulting anomalies of 300 hPa geopotential height tendencies in the PD4LT and ND4LT runs are shown in Figure 9. Main anomaly centers of geopotential height tendency correspond to the geopotential height anomalies implying the positive feedback from the transient eddies which supports anomalies of the mean flow. Given a geopotential height anomaly of about 70 gpm and a geopotential height tendency anomaly of 7 gpm/day such as in the northern North Atlantic in the PD4LT run, the characteristic eddy forcing time scale is $\sim \frac{70\ gpm}{7\ gpm/day} = 10$ days. This value supports the hypothesis that the transient forcing is substantial on monthly time scales and exerts a considerable influence on the seasonal and interannual circulation. The SST anomalies placed in the west North Atlantic are, in turn, related to the variability of the storm tracks, where the most significant transports of vorticity and heat in the extratropics are known to take place.

5.2 The stationary response to 2 K dipole SST anomalies

The stationary atmospheric response to ±2 K SST dipoles in the PD2LT and ND2LT runs is shown in Figure 9. The signal is, as expected, weaker and is statistically less

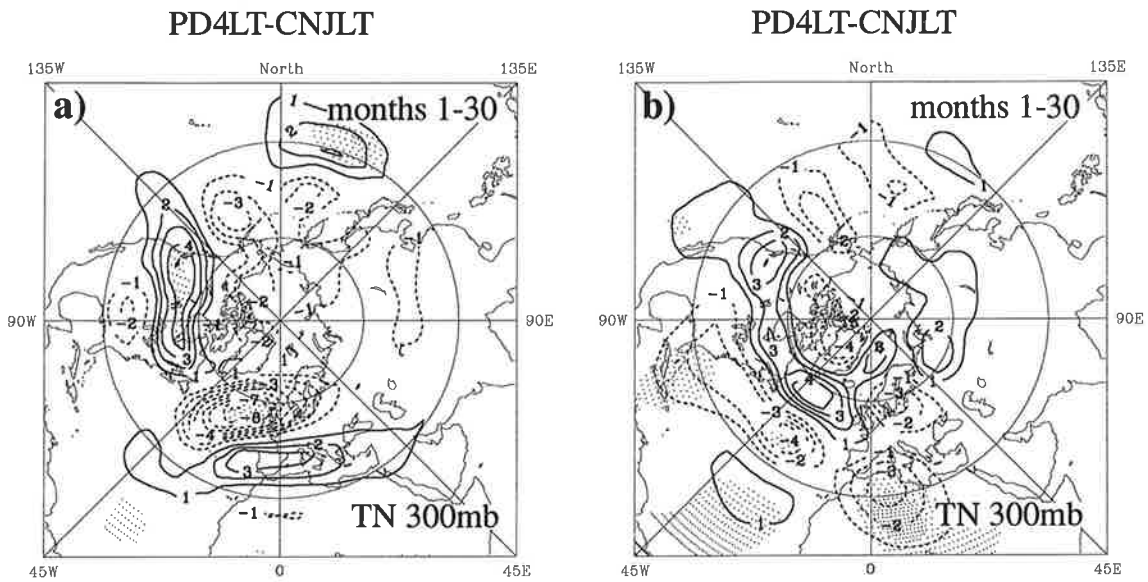

Figure 15: *30-month mean anomaly fields of 300 hPa geopotential height tendency due to barotropic transient eddy (2.5-6 days) forcing in the Northern Hemisphere in the PD4LT run (a) and in the ND4LT (b) experiments. Contour interval is 1 gpm/day. Stipling represents areas with estimated local level of recurrence* $p \leq 30\%$ *or* $p \geq 70\%$ *(light),* $p \leq 20\%$ *or* $p \geq 80\%$ *(moderate),* $p \leq 10\%$ *or* $p \geq 90\%$ *(heavy).*

stable. The spatial structure of 300 hPa geopotential anomalies in the PD2LT run differs significantly from that in the PD4LT experiment. The zero line between negative and positive geopotential height anomalies in the North Atlantic is shifted in the PD2LT run by about 15^o northwards compared to the PD4LT run. The positive geopotential height center placed in the PD4LT run over southern Europe is moved to the east at 55^oN 90^oE in the PD2LT experiment.

The 300 hPa geopotential height anomaly field in the ND2LT run is basically the same as in the ND4LT. Positive height anomaly is found in the northern North Atlanitc and over the North America continent. The local statistical stability of the patterns in the ND2LT run is not very high.

The amplitude of the atmospheric response in the experiments with the halfed SST anomalies, although being slightly smaller, is not twice less than in the PD4LT and ND4LT runs. The spatial structure of anomaly patterns is different in the GCM exeriemtns with ± 4 K and ± 2 K SST anomalies. Thus, the atmospheric response in the GCM depends non-linearly on SST anomalies of amplitudes over 2 K. Let us assume that the stationary response is a solution of the following nonlinear system:

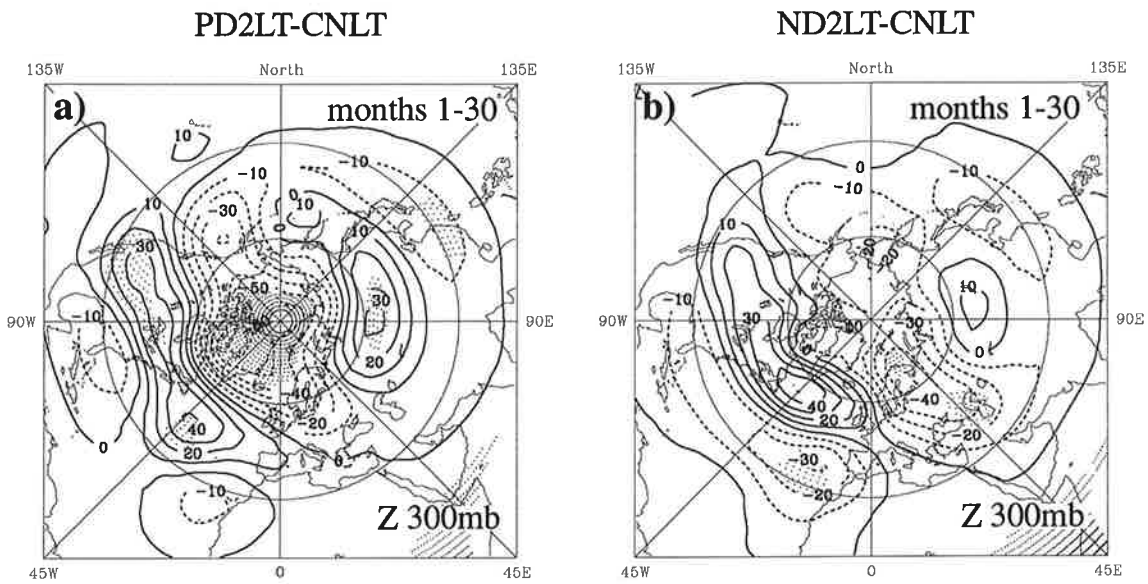

Figure 16: *30-month mean anomaly fields of geopotential height at 300 hPa in the PD2LT run (a,b,c) and in the ND2LT (d,e,f) experiments in the Northern Hemisphere compared to the control run. Contour interval is 10 gpm. Stipling represents areas with estimated local level of recurrence* $p \leq 30\%$ *or* $p \geq 70\%$ *(light),* $p \leq 20\%$ *or* $p \geq 80\%$ *(moderate).*

$$A(\bar{\phi}, \phi', ...) = F(\delta T, \bar{\phi}, \phi', ...). \tag{41}$$

Here A is the nonlinear operator depending on the mean atmospheric state $\bar{\phi}$, the stationary solution ϕ' etc. F is the external forcing which depends in addition on SST anomalies δT. According to (41) at least two kinds of factors may be responsible for the nonlinear behavior of the atmospheric signal. First, the nonlinear dependence of the forcing term F on the SST anomalies δT. Secondly, if the deviations ϕ' from the mean flow $\bar{\phi}$ are not small then the nonlinear effects may be caused by the nonlinear operator A.

We examined the influence of some model parameters on the linearity of model response. Particularly, the turbulent heat flux at the surface in the model boundary layer is parameterized as follows

$$J_H = -\rho C_H(Ri)|u|\delta T \tag{42}$$

where J_H is the surface heat flux, ρ is the specific mass of the air, C_H is the heat transfer coefficient and $|u|$ is the absolute value of the horizontal velocity at the lowest

model level. The transfer coefficient C_H depends strongly nonlinearly on the Richardson number which is in turn proportional to δT (DKRZ, 1992; Roeckner et al., 1992). For unstable cases with large positive SST anomalies δT (negative values of Ri) the transfer coefficient is much larger than for near neutral or stable cases (negative δT).

We performed a number of GCM experiments with the fixed Richardson number at the surface to exclude at least this nonlinear factor. The atmospheric response on ± 4 K dipole SST anomalies in these experiments (not shown) remained asymmetric with respect to the sign of SST anomalies. Thus, the nonlinear behavior of the atmospheric signal cannot be explained only in terms of local nonlinear dependence of heat fluxes on the SST anomalies.

5.3 The stationary response to monopol-type SST anomalies

In the previous subsection the dependence of the atmospheric response on the amplitude of SST anomalies is demonstrated. Another question of interest is the dependence of the atmospheric signal on the geographical location of the heat forcing. Figure 9 shows the stationary signal at 300 hPa in the long term experiments made with monopole SST anomalies of ± 4 K in different parts of the North Atlantic.

Only in one case the atmosperic response is relatively strong, namely, if the positive SST anomaly is placed at the US coast between Newfoundland and Peninsula Florida (the PMS4LT run in Figure 9a). The spatial structure and the amplitude of the 300 hPa geopotential height anomaly in this run is comparable to the those in the PD4LT run with the dipole SST anomaly. It seems that the atmospheric response to the positive SST dipole is mainly due to the positive SST anomaly at the US coast. The extratropical response in all other GCM runs with monopole SST anomalies is weak and statistically not stable.

The extratropical response to the negative SST anomaly at the US coast (the NMS4LT run, Figure 9b) is much smaller than the signal to the positive SST anomaly at this place. Negative height anomalies are found in subtropical region at the African coast, in polar regions and northeast of the Black Sea. In the PMN4LT run with the positive SST anomaly east of Newfoundland (Figure 9c) a small negative height anomaly is located over and east of the SST center and a relatively strong positive height anomaly placed north and west of the negative anomaly. In the case of the negative SST anomaly east of Newfoundland (the NMN4LT run, Figure 9d) negative height anomalies are found over the northern parts of the North Atlantic and in polar

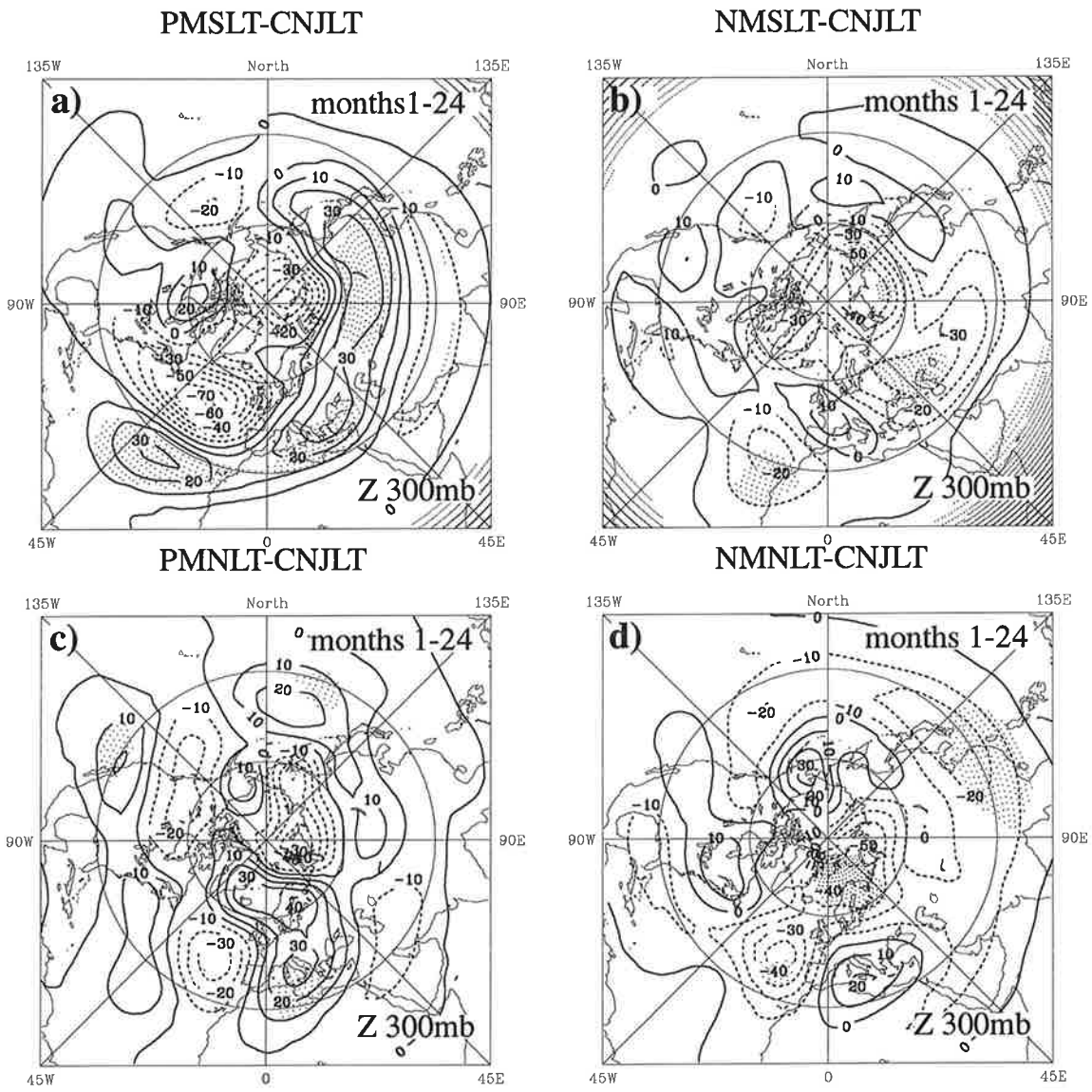

Figure 17: *24-month mean anomaly fields of geopotential height at 300 hPa in the PMS4LT (a), the NMS4LT (b), the PMN4LT (c) and the NMN4LT (d) experiments in the Northern Hemisphere compared to the control run. Contour interval is 10 gpm. Stipling represents areas with estimated local level of recurrence $p \leq 30\%$ or $p \geq 70\%$ (light), $p \leq 20\%$ or $p \geq 80\%$ (moderate).*

regions. However, all these anomalies are only weak stable.

There are some indications that the response to the negative SST anomaly located east of Newfoundland (Figure 9d) supports the North Atlantic response to the positive SST anomaly at the US coast (Figure 9a) resulting together in near the same pattern as the North Atlantic response to the SST dipole (Figure 9a). Thus, the atmospheric response to the dipole SST anomalies in this case is to some extent the sum of the signals to the individual SST centers.

The response to the positive SST anomaly which was derived from the second SST canonical pattern in the PMM4LT run (not shown) was appeared to be very weak and not statistically stable. For the negative SST anomaly in the NMM4LT run the signal is slightly stronger but still statistically nor very stable.

The obtained results demonstrate clearly that the stationary atmospheric response depends crucially on the local position of SST anomalies. Seemingly, only the SST anomalies located in the region with strongest near surface temperature gradients leads to the strongest response. In Section 7 we will show that exactly in this region the adjoint modes of the barotropic operator, which represent the patterns of the forcing exciting the internal variability modes of the barotropic atmosphere most efficiently, have the largest amplitudes.

6 The atmospheric response to time-variable SST

In this section the results of the CCA and EOF analysis for the GCM experiments made with the observed SST (GAGO, MOGA and TOGA runs) are presented. First, the atmospheric response in the North Atlantic region is examined. Then the atmospheric variability in the Northern Hemisphere in the GCMs in terms of the leading EOFs is compared to the observed variability modes. After that the atmospheric response in the Northern Hemisphere in the GAGO, MOGA and TOGA runs as found by the CCA is compared to each other.

6.1 The atmospheric response in the North Atlantic region

To compare the model results with the observational ones discussed in Section 2 the CCA was applied to SLP and SST in the near same geographical region. The SST field covers the area $14°N - 64°N$ $90°W - 5°W$. The oceanic grid points with sea surface temperature below $-1.8°$ were assumed to be covered with ice and were excluded from the analysis. The SLP field covers the area $100°W - 10°E$ $0°N - 90°N$.

Since there is no interannual SST variability almost in the whole region in study in the TOGA run, we consider in this subsection only the GAGO and MOGA experiments. The results of the CCA applied to SST in the tropical Atlantic ($25°S - 25°N$) and SLP in the North Atlantic region in the TOGA run appeared to be statistically insignificant. The first canonical correlation in this case is 0.49 which is statistically significant only at the level below 70% (see Appendix A). Thus, in the TOGA run there is no statistically stable relationship between North Atlantic SLP and tropical Atlantic SST.

The first 5 EOFs explain about 87% of the total SLP variability and 72% of the total SST variability in the GAGO run in the region in study. In the MOGA run the amount of the variance explained by the first 5 EOFs is 85% for SLP and 78% for SST. The obtained first pairs of canonical patterns of SLP and SST in the GAGO and MOGA experiments are shown in Figure 9. The canonical patterns appeared to be stable with respect to the number of the EOFs retained in the analysis. The pattern correlations between the first canonical maps of SLP and SST obtained in the CCA with 5 EOFs retained for each field and the canonical maps obtained in the CCA with the number of retained EOFs in the range 4-7 exceed in all cases the value of 0.99. The pattern correlations are still high ($\geq$ 0.92) if the results of the CCA for the 3-month winter season (December-February) and 5 EOFs retained for each field are compared to the

corresponding results of the CCA for the 5-month winter season (November-March).

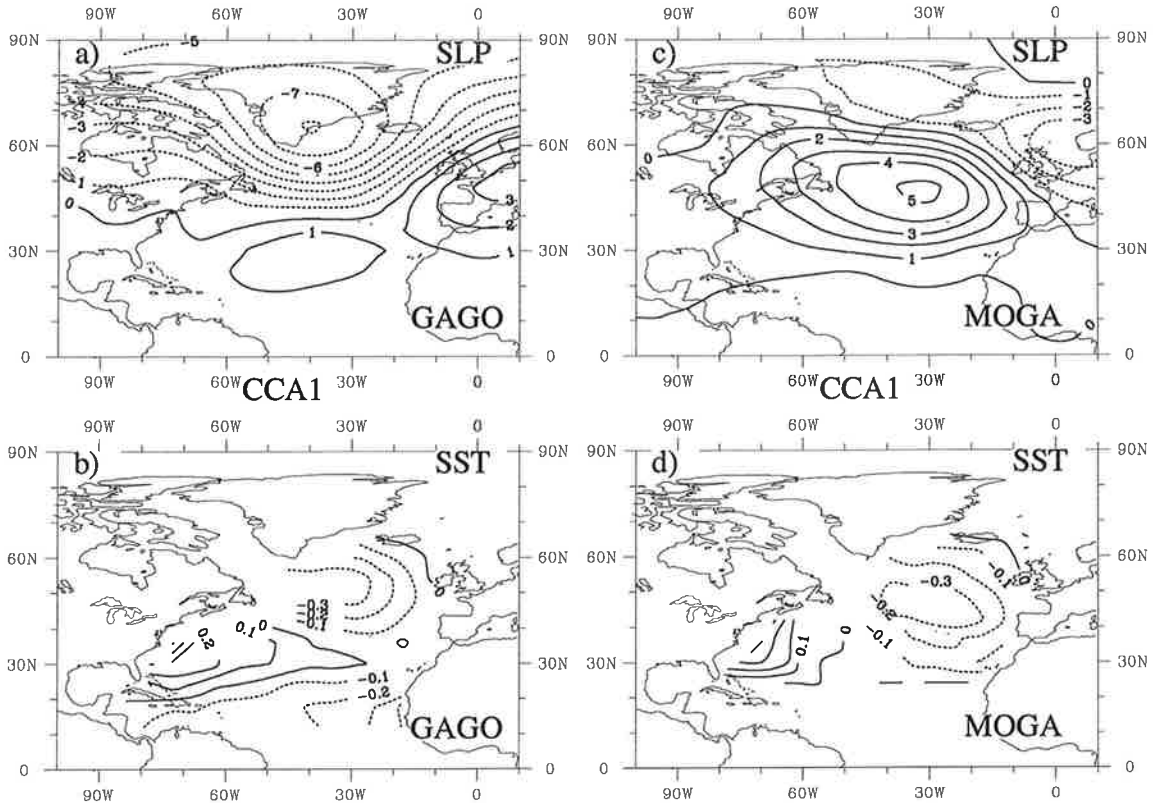

Figure 18: *The SLP and SST first canonical patterns in the North Atlantic area in the GAGO run (a, b; canonical correlation 0.66) and in the MOGA run (c, d; canonical correlation 0.54). They explain 32% (a; SLP) and 21% (b; SST) of the total variance in the GAGO run and 15% (c; SLP) and 25% (d; SST) of the total variance in the MOGA run. Contour interval is 1 mb for SLP and 0.1 K for SST.*

The SLP and SST patterns in the GAGO run are very similar to the first pair of canonical patterns calculated for the observed data. The SLP pattern (Figure 9a) explains 32% of the total variance and is essentially the first EOF in this region. It is characterized by a large scale north-south dipole with one center with amplitude of about 8 mb over the south of Greenland and another one of opposite sign and weaker amplitude of 1 mb in the central North Atlantic at $30°N$. There is another positive SLP anomaly of 3 mb over Europe. The SLP pattern represents basically the intensification of zonal circulation over the North Atlantic in the latitude band $50°N - 60°N$. The SST canonical pattern (Figure 9b) explains 21% of the total variance and contains three regions with SST anomalies of high amplitude. Negative SST anomalies are placed south of Greenland at $55°N$ $40°W$ and west of North of Africa at $15°N$. A positive center is

situated at the American coast between Newfoundland and the Florida peninsula.

The canonical correlation is 0.66. The statistical significance of this value defined by Monte-Carlo simulations is 99.5% (Appendix A). The atmospheric signal was found to be equivalent-barotropic. Particularly, the structure of the linear regression map of 500 hPa geopotential height (H500) in the North Atlantic obtained on the base of the first canonical time component of SST (not shown) is very similar to the structure of the SLP pattern with a pattern correlation above 0.8.

The linear relationship between SLP and SST in the North Atlantic in the MOGA run is weaker than in the GAGO run. The canonical correlation for the first pair of SLP and SST patterns in the MOGA run is 0.54 which is statistically significant only at the 80% level. The SLP pattern (Figure 9c) explains 15% of the total variance and differs significantly from the SLP pattern in the GAGO run. A positive large scale SLP anomaly of 5 mb is located over the central North Atlantic with the center at $45°N$ $30°W$. A negative SLP anomaly of 3 mb is found over Northern Europe. The first canonical pattern of SST (Figure 9d) is responsible for about 25% of the total SST variability in the North Atlantic northwards of $25°N$. This pattern resembles the first canonical SST map in the GAGO run in the corresponding region. A positive SST anomaly is placed at the US coast at $30°N - 45°N$. A negative SST anomaly is located at $40°N$ $30°W$.

The corresponding time components of the SLP and SST patterns in the GAGO and MOGA runs are shown in Figure 9. The high correlation between the two time series in the GAGO experiment (Figure 9a) is not due only to some single events. On both time scales, monthly and interannual, the time series behave coherently. In the MOGA run (Figure 9b) there are periods of coherent behavior (e.g. years 1981-1983) as well as several events which are out of phase (e.g. years 1972-1973).

Although the differences between the first canonical SST patterns in the GAGO and MOGA runs are not very large (the pattern correlation is 0.65 in the region northwards of $25°N$ and the correlation between canonical SST time series is 0.67) the atmospheric signals look very different. Since the first canonical correlation in the MOGA run is relatively weak, one might think that only in the GAGO run we deal with a statistically stable linkage between SLP and SST anomalies in the North Atlantic. The near surface atmospheric response in the North Atlantic in the GAGO run is nearly consistent with the stationary SLP signal to the positive SST dipole which is very similar to the SST canonical pattern (Figure 9). In the both patterns a negative SLP anomaly is found in the northern part of the North Atlantic and a positive SLP anomaly over the subtropical

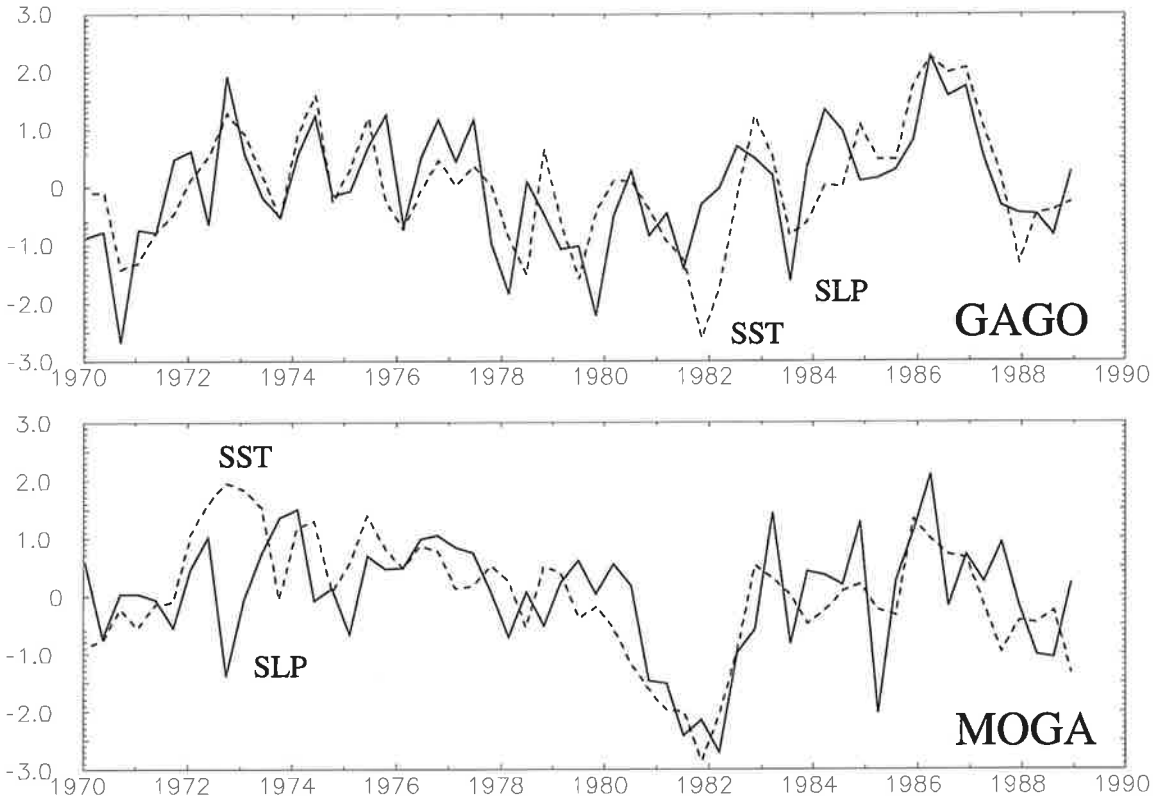

Figure 19: *Time components of the first canonical patterns of North Atlantic SLP (solid line) and North Atlantic SST (dashed line) in the GAGO run (a) and in the MOGA run (b). The correlation between the time series is 0.66 in the GAGO run and 0.54 in the MOGA run.*

North Atlantic. However, the negative center in the long term run PD4LT is placed further to the east compared to the negative center in the GAGO run.

6.2 The leading modes of atmospheric variability in the GCM runs

Before the results of the CCA will be presented we examine first the leading modes of the wintertime atmospheric variability in the Northern Hemisphere in the GCM runs in terms of EOFs and compare them with the observed variability modes. The EOFs were calculated as the eigenvectors of the covariance matrix. Before the EOF analysis the H500 anomalies were weighted by the square root of the latitude cosine to take into account the spherical geometry of the fields. In the following, presenting the results, the area weightings have been removed from the data. The principal components have been normalized by unity so that the EOF maps represent the "typical" strength of the atmospheric variability.

The first EOFs of Northern Hemisphere H500 in the GAGO, MOGA, TOGA and CONTROL runs are depicted in Figure 9. The general structure of the all EOFs is similar, having negative geopotential height anomalies over the northern parts of the oceans and in the polar regions and positive eight anomalies roughly southwards of the negative anomalies. Anomalies of maximal amplitude are located in the North Atlantic sector. The pattern correlation between the first EOF in the CONTROL run and other first EOFs exceeds in all cases the value of 0.9 indicating the general similarity of the model first EOFs in the Northern Hemisphere. A more thorough analysis reveals, however, some differences in the structure of the EOFs. In the GAGO run the zero line between positive and negative anomalies in the North Atlantic is placed slightly further south than in the other runs. The first EOF of the MOGA run has a more zonally symmetric structure. In the TOGA run the positive height anomaly in the North Pacific has the largest amplitude over 40 gpm.

The explained variances of the first 10 EOFs in absolute values gpm^2 and the relative explained variances in % in the GCM experiments are shown in Figure 9. In the GAGO run the first EOF has the largest amplitude and explains the largest portion of the total variance in relative units (26%) as well as in absolute values (452 gpm^2). The second EOF in the GAGO run explained almost twice less the variance (14%). The EOFs 3-6 explain each about 6-8%. The EOF spectra in the MOGA and TOGA runs are flatter. The amplitude of the first EOF in the MOGA run is the smallest among all the GCM

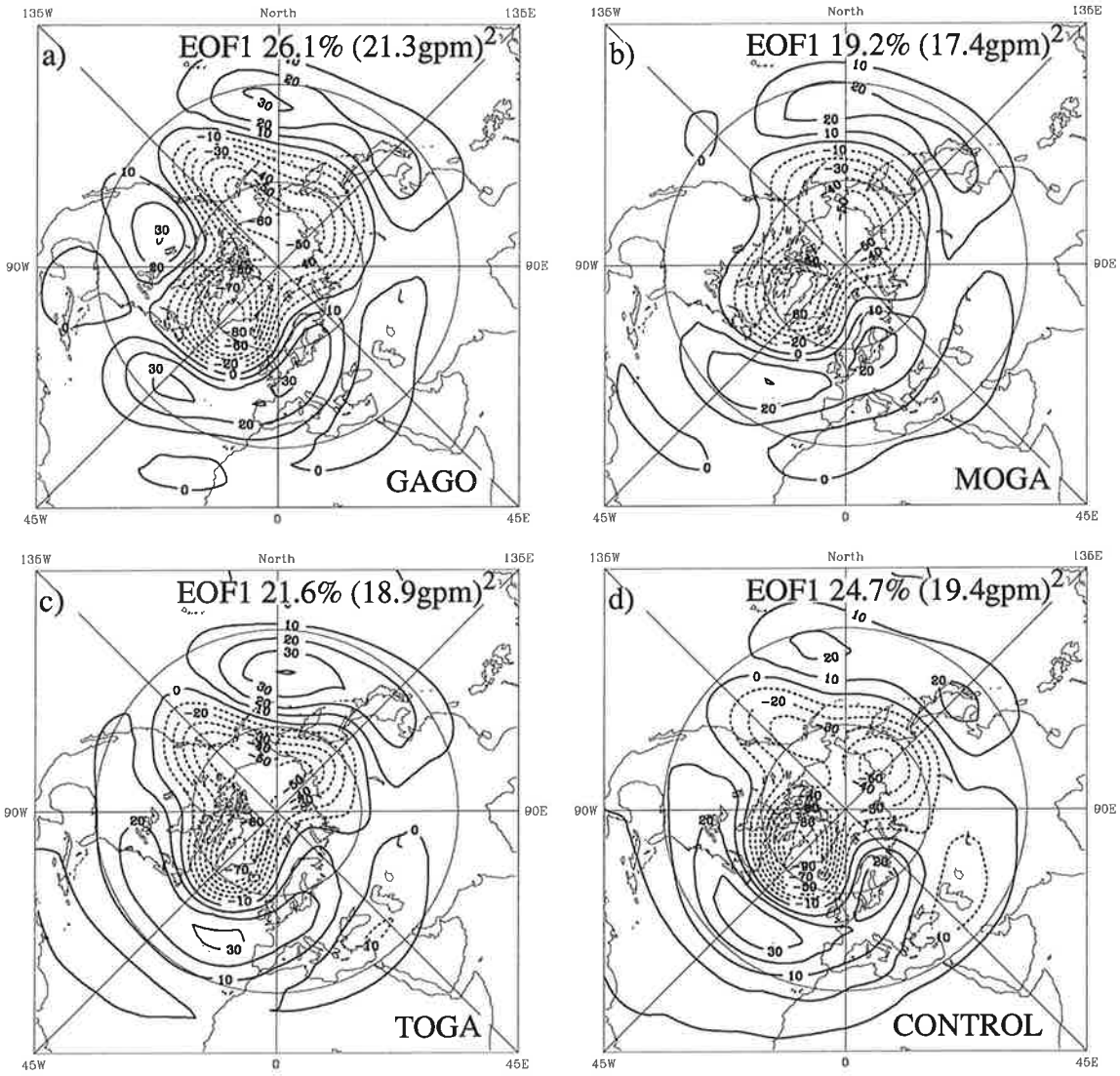

Figure 20: *The first EOFs of Northern Hemisphere H500 in winter in the GAGO (a), MOGA (b), TOGA (c) and CONTROL (d) runs. They explain 26.1%, 19.2%, 21.6% and 24.7%, respectively. Contour interval 10 gpm.*

experiments (302 gpm^2). It explains 19% of the total variance. The EOFs 2-4 explain a roughly equal amount of the variance (11-12%). The first EOF of the TOGA run is of larger amplitude than in the MOGA run but is weaker than in the GAGO and CONTROL experiments and is responsible for 22% of the total variability. The ratio of the variance explained by the first EOF to the variance explained the second EOF in the MOGA and TOGA runs is about 1.5 so that the leading EOF is less dominant in these experiments than in the GAGO run. In the CONTROL run the first EOF (25% of the total variance) is again well separated from the second EOF (14% of the total variance). The shape of the EOF spectra for the EOF numbers larger than 5 is nearly the same in the all GCM runs. In all GCM experiments the first 5 EOFs explain about 60% of the total variability.

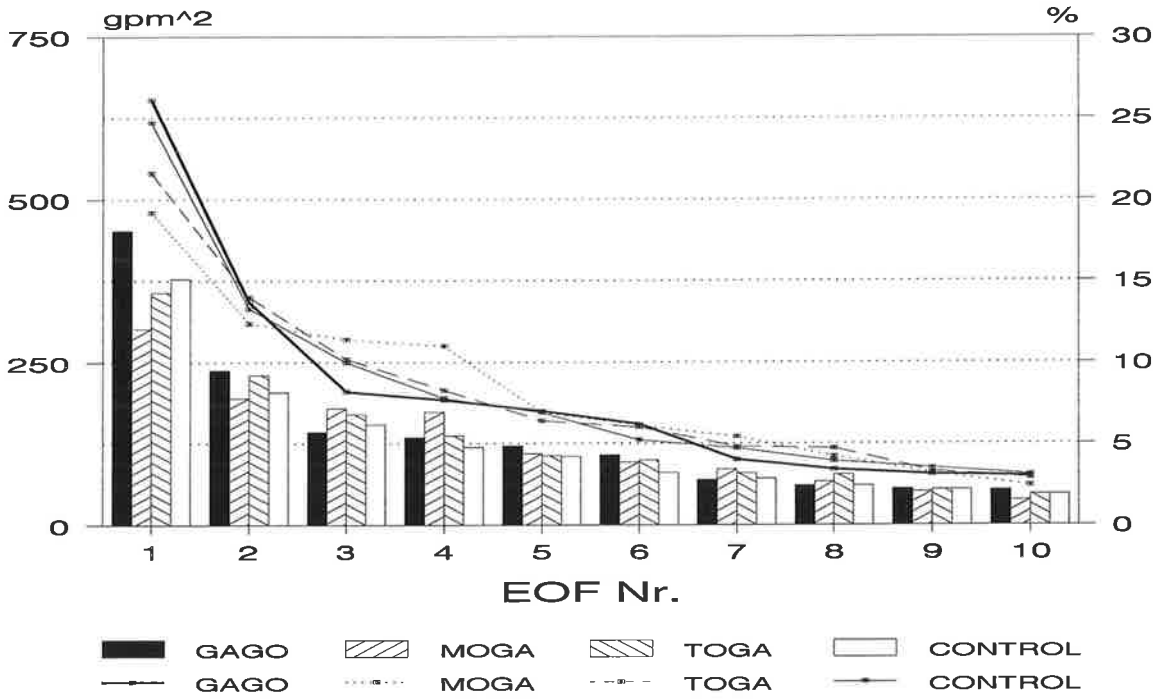

Figure 21: *The explained variances of the first 10 EOFs of Northern Hemisphere H500 in winter in absolute values gpm^2 (bars) and in relative units % (lines) in the GAGO, MOGA, TOGA and CONTROL runs.*

The second EOFs in the GAGO, TOGA and MOGA runs (not shown) have the strongest anomalies in the North Pacific / North America sector. They are to some extent similar to the PNA pattern described by Wallace and Gutzler (1981). They possess positive height anomalies in the tropical North Pacific and over the northern part of the North American continent, and negative height anomalies over the northern

part of the North Pacific and over the south-east of North America. Such a pattern is missing in the CONTROL run. The second EOF in the CONTROL experiment has a wavetrain structure with anomalies spreading from the western North Pacific over the North Pole to the central North Atlantic.

For comparison the first two EOFs calculated for observed monthly means of H500 in the region north of 20°N in 1970-1987 in winter (provided by NCAR) are shown in Figure 9. The first EOF of the observed atmospheric variability has the main center over the North Pacific and differs significantly from the leading EOFs in the GCM runs. The amplitude of the positive anomaly in the North Pacific is over 90 *gpm* which exceeds substantially the amplitude of the height anomalies in this region in the GCM runs. The negative anomaly in the northern part of the North Atlantic is, on the contrary, of much smaller amplitude than in the GCM experiments. Only the second observed EOF has some similarity with the model first EOFs in the North Atlantic region. The pattern correlation between the observed second EOF and the first EOF in the CONTROL run is 0.68 in the Northern Hemisphere north of 20°N. The first EOF is less dominant compared to the GCM experiments. The explained variances are 21% and 16%, respectively. The ratio of the variance explained by the first EOF to the variance of the second EOFs (1.3) is smaller than in the GCM runs.

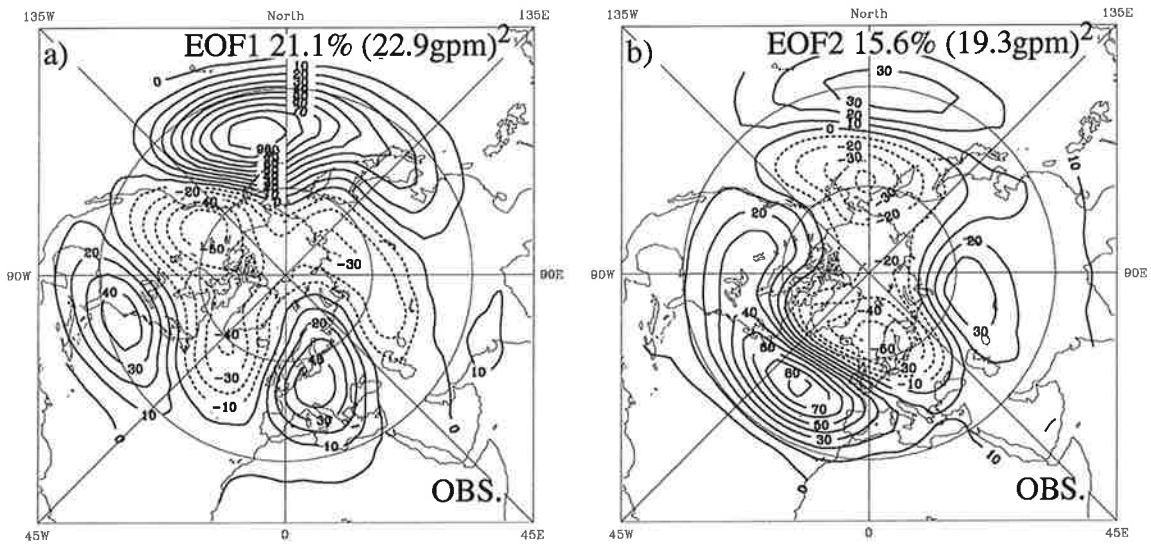

Figure 22: *The first and the second EOFs of Northern Hemisphere H500 variability in winter in the observed in 1970-1987 data provided by NCAR. They explain 21% and 16% of the total variance, respectively.*

Thus, the leading modes of atmospheric variability in the GCM differ significantly from that in the observations. In some sense the order of the first two EOFs in the

GCM experiments is inverse compared to the observed EOFs. A variability mode like PNA is the first EOF in the observations and the second EOF in the GAGO, MOGA and TOGA runs. A variability mode with the strongest anomalies in the North Atlantic is the first EOF in the GCMs and only the second EOF in the observations. In view of this fact the spatial structure atmospheric response in the GCM experiments might be improperly reproduced compared to the observed atmosphere. Therefore the results of the GCM experiments might be of poor relevance if compared directly with the observed atmospheric anomalies. Nevertheless, it still might be interesting to know the potential effect of the SST forcing in different geographical regions on the atmospheric variability in the GCM and to understand the dynamical mechanisms which could be important for the atmospheric response in the observed atmosphere/ocean coupled system.

From the results of the EOF analysis which manifest the overall impact of the SST variability on the model atmospheric circulation one could suggest that the global SST forcing in the GAGO run substantially increases the variability associated with the first EOF. The relative variance of the second EOFs in the GAGO and TOGA run, which is similar to the PNA pattern and presumably related to the tropical SST anomalies in the Pacific, is slightly larger than in the CONTROL and in the MOGA runs. In the following subsections we try to identify by means of the CCA the SST anomaly distributions which are responsible for the changes in the atmospheric variability in the GCM runs.

6.3 The Northern Hemisphere atmospheric response in the GAGO run

First, we show that in the GAGO run both the North Atlantic and the extratropical North Pacific SST anomalies contribute to the atmospheric response found in the North Atlantic sector. We applied the CCA to H500 over the whole Northern Hemisphere northwards of the Equator and SST in the North Atlantic and the North Pacific. The North Atlantic region for SST was the same as in the previous section. The SST anomalies in the North Pacific were taken northwards of $25°N$ to avoid the influence of the prominent anomalies in the Equatorial Pacific.

The best correlated H500 and SST patterns are shown in Figure 9. Both atmospheric patterns (Figure 9a,c) explain about 15% of the total variability and are of near the same structure in the North Atlantic sector as the SLP pattern shown in Figure 9a. The pattern correlation between the H500 maps in the North Atlantic region ($100°W - 10°E$

$14°N-85°N$) is about 0.8. The spatial correlation over the whole Northern Hemisphere is, however, weaker ($\sim$ 0.5) which is explained by the map differences in the North Pacific sector. The North Atlantic SST canonical pattern (Figure 9b) remains nearly the same as in the case of the CCA applied to North Atlantic SST and SLP. It explains somewhat less variance (14%). In the North Pacific the SST canonical map (Figure 9d) explains about 16% of the total variance and consists basically of two centers, a negative anomaly in the West Pacific off the Japan coast and a positive anomaly centered at $150°W$ $35°N$.

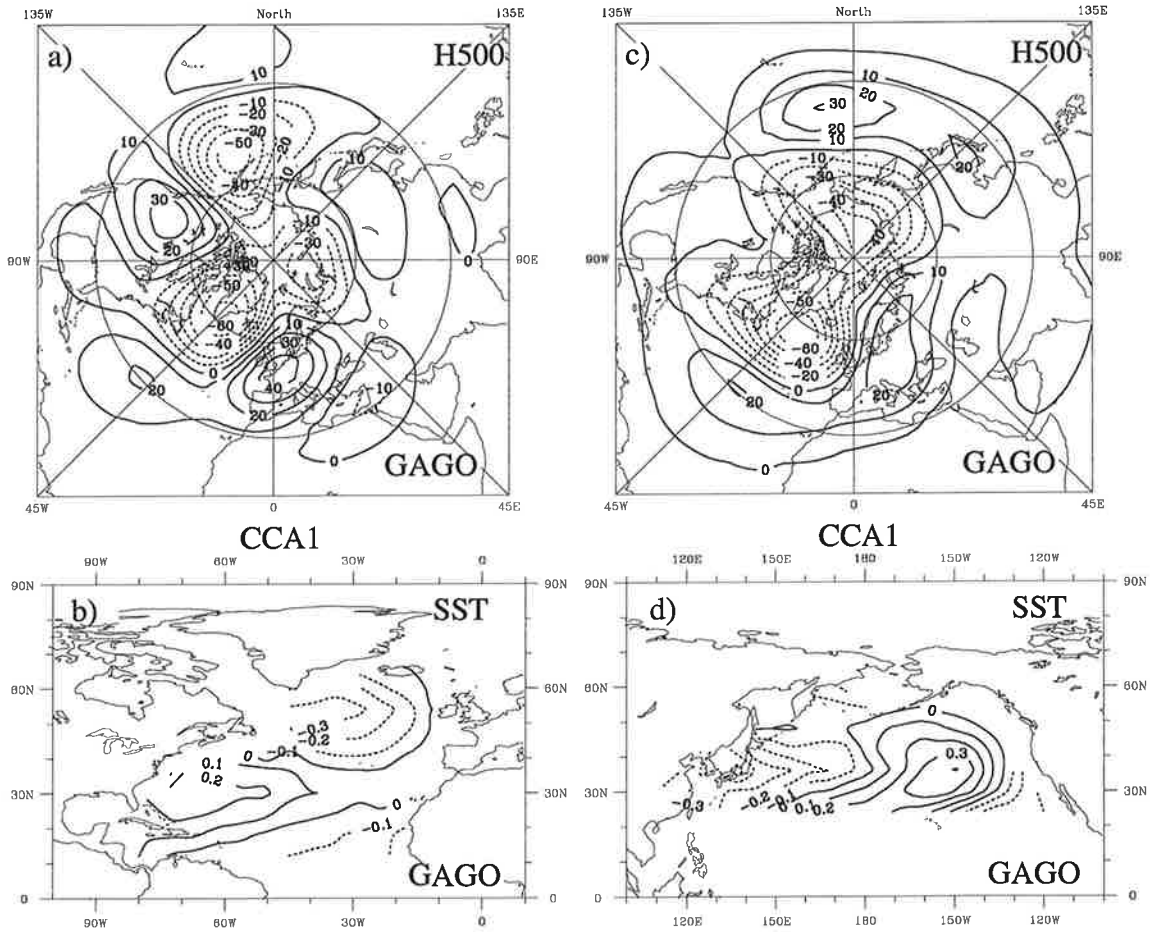

Figure 23: *The patterns of the first canonical pairs of Northern Hemisphere H500 (a) and North Atlantic SST (b) and of Northern Hemisphere H500 (c) and North Pacific SST (d) in the GAGO run. The H500 patterns (a, d; contour interval 10 gpm) explain 15% of the total variance. The SST patterns (b, d; contour interval 0.1 K) explain 14% and 16% of the total variance in the North Atlantic and the North Pacific, respectively.*

The first canonical correlations are 0.61 and 0.64 for the North Atlantic and North

Pacific regions, respectively, which are statistically significant at the 97% level (Appendix A). The canonical patterns are relatively stable and do not change significantly if the number of EOFs retained in the CCA analysis is varied in the range of 3-7. The results of the CCA for the 5-month winter season are also essentially the same as described above.

To answer the question whether the atmospheric signal in the GAGO experiment found in the previous analyses is affected by the tropical SST anomalies in the Pacific we applied the CCA to Northern Hemisphere H500 and near global SST north of 25°S. In this region the observed SST was prescribed in the GAGO run during the whole 19-year period. The first two pairs of canonical patterns are shown in Figure 9.

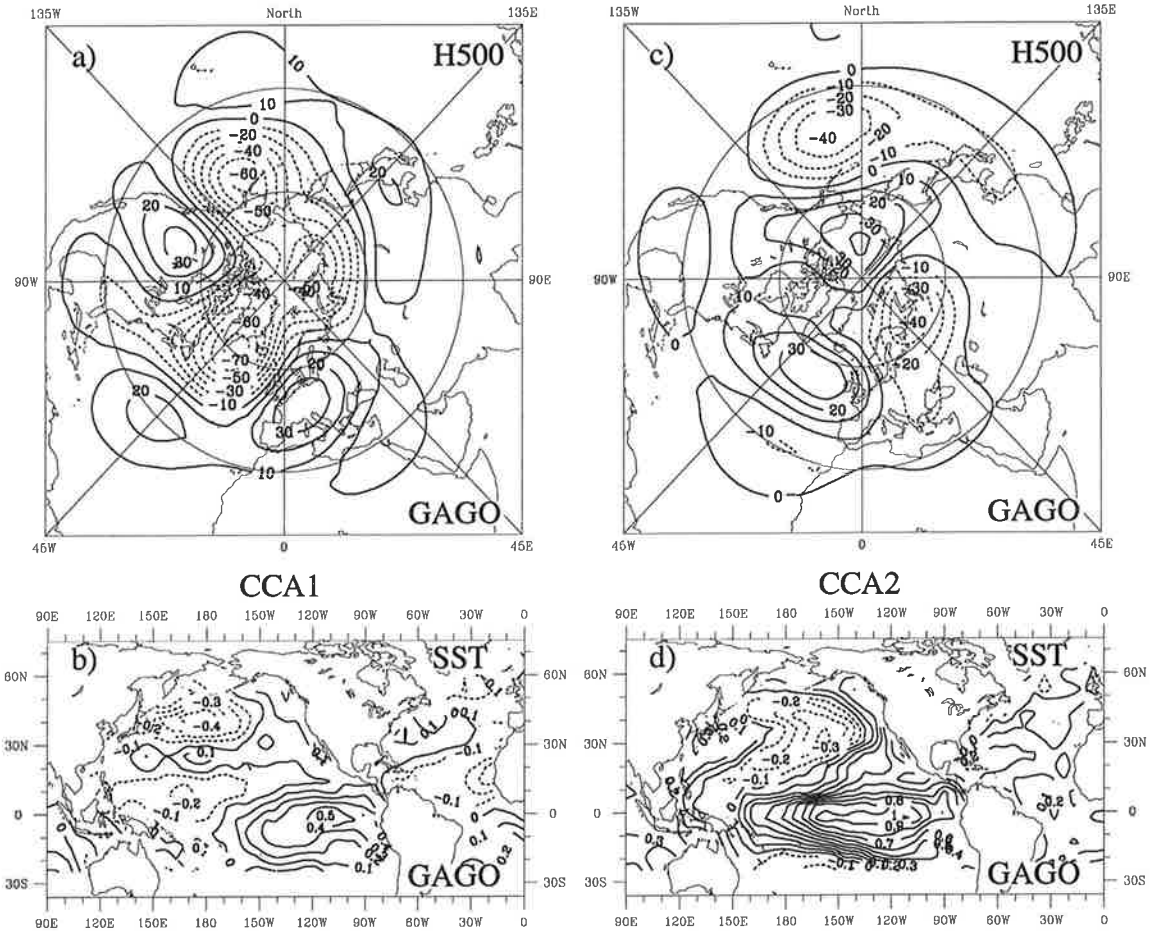

Figure 24: *The patterns of the first two canonical pairs of Northern Hemisphere H500 (a, c; contour interval 10 gpm) and SST north of 25°S (b, c; contour interval 0.1 K) in the GAGO run. The first canonical patterns explain 21% (H500) and 9% (SST) of the total variance. The second canonical patterns explain 9% (H500) and 40% (SST) of the total variance.*

The first H500 pattern (Figure 9a), which explains 21% of the total variance, has a similar global structure as in Figure 9a,c. In the SST pattern (Figure 9b) one can still recognize three centers of action in the North Atlantic and a similar SST dipole in the middle latitudes of the North Pacific which have been already found in the previous SST patterns. Another SST maximum of 0.5 K is located in the eastern tropical Pacific. The explained variance of the global SST pattern is less than 9%. This map is certainly not a typical El Niño pattern which is the dominant mode of the global interannual SST variability.

In the following we will refer to this coupled H500-SST mode as the GAGO1 mode. The first canonical correlation between the two fields is over 0.66 which is statistically significant at the 98% level. The corrected unbiased estimate of this value, according to Glynn and Muirhead's test (Appendix B), is 0.54 with 95% significance interval 0.33-0.70 (Table 9).

Since the first canonical pattern of H500 in the GAGO experiment is very similar to the leading EOF in this run (the pattern correlation is 0.89) one might think that this pattern is an artificial result of linear projections on the dominant mode of the GCM. To estimate the probability of the fact that the CCA results in the canonical patterns which are similar to the dominant variability modes, even if there is no linear relation between two fields, we computed in Monte-Carlo simulations described in Appendix A the pattern correlations between the first canonical pattern of H500 as obtained in the CCA of randomly rearranged time series and the first EOF of H500. In more than 97% of all cases the obtained spatial correlation was smaller than 0.89 indicating that a good resemblance of the first canonical pattern of H500 in the GAGO run to the first EOF is caused with high probability not only by chance. The probability to have high spatial correlation between the first canonical pattern and the first EOF *and* high canonical correlation in Monte-Carlo simulations was even lower. Particularly, none of 200 CCA cases exhibited a first canonical correlation higher than 0.60 and a spatial correlation higher than 0.75.

The typical El Niño pattern in the SST field appeared to be the second canonical pattern (Figure 9d) which explains more than 40% of the total SST variance. There is a strong positive SST anomaly up to 1 K over the central and eastern tropical Pacific and a negative SST anomaly in central midlatitudes of the North Pacific Ocean. These anomalies are usually observed as the leading EOF of SST variability in this region. The atmospheric signal related to this SST pattern with the canonical correlation 0.60 is shown in Figure 9c. The second canonical H500 pattern explains about 9% of the

total variance and consists of negative anomalies of 40 gpm in the North Pacific area and over the Barents Sea and weaker positive anomalies over the North Atlantic and over the East Siberian Sea. In the North Pacific / North America sector the second canonical pattern remains the PNA pattern with the positive height anomalies in the tropical North Pacific and over northern North America and negative anomalies in the extratropical North Pacific and in the subtropical area of North America. Hereafter we will refer to this mode as the GAGO2 mode.

The GAGO1 mode is not related to the prominent SST anomalies in the tropical Pacific. To verify this fact that we calculated the correlation between the index defined as SST averaged each month over the region $150°W - 90°W$ $5°S - 5°N$ (the ENSO3 region) and the corresponding canonical time series of SST and H500. For both the H500 and the SST time components of the first canonical pair the correlation with the SST index is only about 0.2-0.3. The second canonical time component of SST is, on the contrary, very well correlated with the SST index (~ 0.9). The correlation of the second canonical time series of H500 with the SST index is, however, somewhat weaker (~ 0.5) but still higher than for the first canonical mode.

To be sure that the SST anomalies associated with the El Niño phenomenon do not influence the GAGO1 signal we eliminated from the original SST and H500 fields the variability which is linearly related to the SST index defined as above and then repeated the CCA with these new fields. The first canonical patterns obtained in this case (not shown) were practically not changed. The only difference in the new SST canonical pattern was that the relatively small positive SST anomalies in the eastern part of the tropical Pacific, which were presented in the original SST canonical pattern, disappeared. The first canonical correlation was even higher (0.68) than for the original fields. Thus we can conclude that the strongest atmospheric signal of the CCA analysis in the GAGO experiment is not related to the strong SST variability associated with El Niño.

The GAGO1 signal is related to the extratropical SST anomalies in the eastern parts of the both basins which have a longitudinal structure. These regions are known for the most significant transport of vorticity and heat into the extratropics. The variations of the SST meridional gradients associated with the SST anomalies in these regions are presumably related to the variability of the storm tracks which are expected to exert a considerable influence on the seasonal and interannual circulation. The GAGO1 pattern is very similar to the stationary atmospheric response in the long term experiment PD4LT (Figure 9) which again indicates a physical meaning of the GAGO1 mode.

6.4 The Northern Hemisphere atmospheric response in the MOGA and TOGA runs

Before we present the results of the MOGA and the TOGA experiments, we discuss shortly the atmospheric signal which can be expected in these runs compared to the coupled modes found in the GAGO experiment. Basically we are interested in the question of whether the MOGA run or the TOGA run is able to reproduce the strongest atmospheric signal found in the GAGO integration. If we assume that the GAGO1 mode is a physically meaningful and statistically significant signal and is not just an artificial product of the CCA (a small probability of the latter still exists, as was demonstrated by Monte-Carlo simulations in Appendix A) then there are several possibilities for the atmospheric response behavior in the MOGA and the TOGA runs:

- If only extratropical SST anomalies are essential for exciting the global dominant GAGO1 mode then we would expect the same signal in the MOGA run.
- If, on the contrary, tropical SST anomalies play the most important role for the GAGO1 mode, then the TOGA run should reproduce this signal.
- Finally, it could happen that none of the runs reproduces the GAGO1 mode. That would mean that both tropical and extratropical SST anomalies contribute to the atmospheric response like the GAGO1 mode. If SST anomalies in midlatitudes and tropics act on the atmosphere in a linear way then the atmospheric response in the GAGO experiment would be just the sum of the responses in the MOGA and TOGA runs. Then one would expect that the linear combination of atmospheric anomalies in the MOGA and TOGA runs would result in the same signal as in the GAGO experiment.
- If the last possibility still fails to explain the GAGO1 mode then the problem becomes more complicated, since nonlinear interactions between midlatitudes and tropics are important for the atmospheric response.
- A wrong representation of the SST gradient at $25° - 30°N$ in the MOGA and TOGA runs could also influence the atmospheric response in these experiments.

The first canonical patterns of Northern Hemisphere H500 and of extratropical and tropical SST in the MOGA and TOGA runs, respectively, are shown in Figure 9. The canonical correlation between the corresponding time series in the MOGA run is 0.61.

This is weaker than in the GAGO run but still statistically significant at the 95% level. The corrected unbiased correlation (Table 9 in Appendix B) is 0.49 which is also lower than in the GAGO run. The H500 pattern depicted in Figure 9a (we will call it hereafter the MOGA1 mode) has strong anomalies in the North Atlantic sector and explains less variance (13%) than the first canonical pattern in the GAGO experiment. In the North Atlantic region the structure of the H500 pattern is similar to the structure of the first canonical SLP pattern shown in Figure 9c. The pattern correlation of the first canonical pattern of H500 with the first EOF in the MOGA run is 0.66 so that the resemblance between the leading variability mode and the first canonical mode in this experiment is substantially weaker than in the GAGO run.

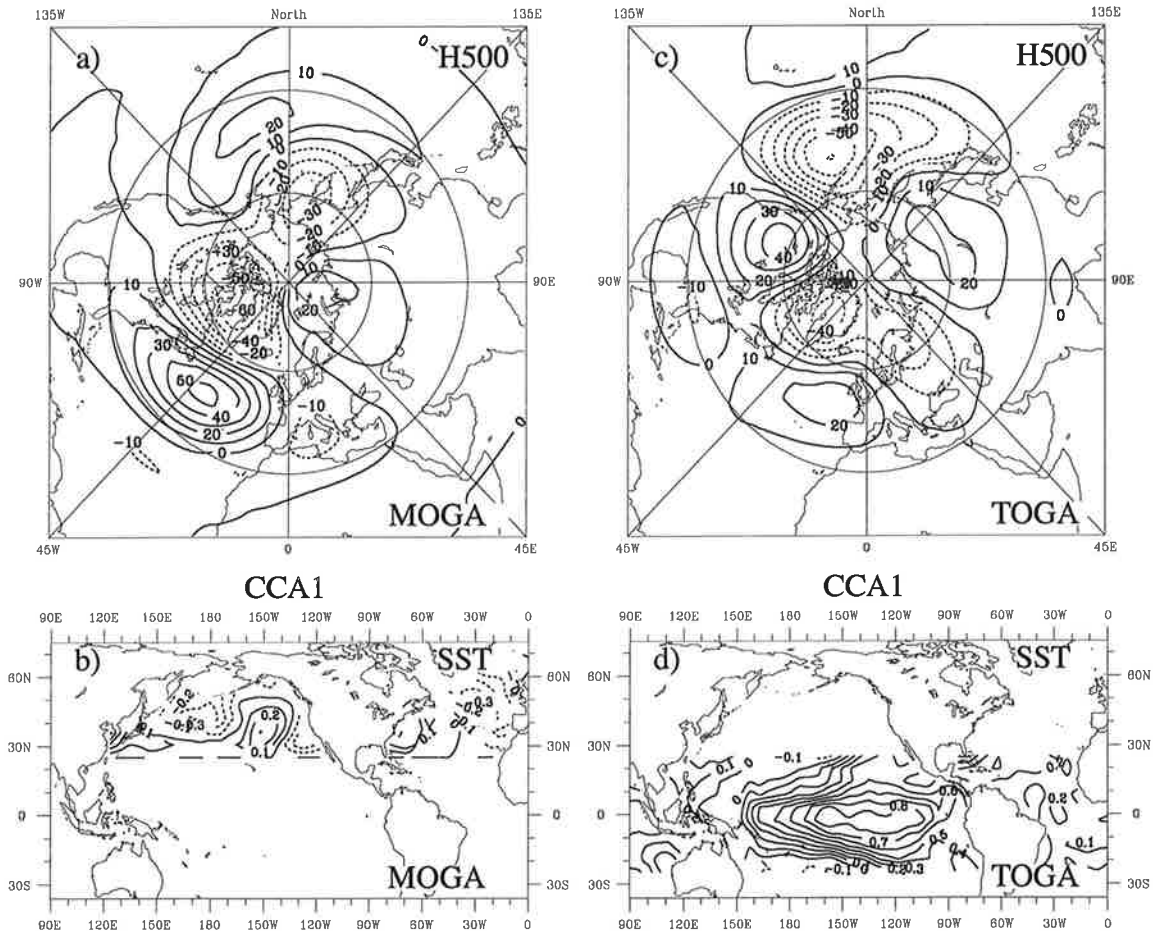

Figure 25: *The patterns of the first canonical pairs of Northern Hemisphere H500 and extratropical (tropical) SST in the MOGA (TOGA) run. They explain 13% (a; H500) and 11% (b; SST) of the total variance in the MOGA run and 14% (c; H500) and 41% (d; SST) of the total variance in the TOGA run. Contour interval is 10 gpm for H500 and 0.1 K for SST.*

The distribution of SST anomalies in the first canonical pattern in the MOGA run (Figure 9b) is similar in the extratropics to that in the first SST canonical pattern obtained in the GAGO run. More thorough analysis reveals some differences in the structure of the SST maps. The SST anomalies in the first canonical pattern in the MOGA run are more zonally orientated compared to the extratropical SST anomalies in the first canonical SST map in the GAGO run. The positive SST anomaly in the western North Pacific is stronger in the MOGA run than in the GAGO experiment. The zero line between positive and negative SST anomalies in the western North Pacific in the MOGA run is situated slightly north of its position in the GAGO experiment. The meridional SST gradients associated with the SST anomalies in the GAGO1 and MOGA1 SST patterns are substantially different, especially in the $25^{o}N-30^{o}N$ latitude band.

The strongest atmospheric response in the MOGA run has a quite different structure from that in the GAGO experiment. It seems that the heat and vorticity forcing associated with a slightly different SST anomaly distribution in the MOGA run excites completely different type of atmospheric mode than in the GAGO run. The SST anomalies in the MOGA run are only weakly, if at all, related to the like GAGO1 mode of atmospheric variability. Correlation coefficients between SST anomalies at each grid point and the time series associated with the GAGO1 mode obtained by projecting anomalies of H500 taken from the MOGA run onto the GAGO1 H500 pattern are less than 0.2 in the MOGA experiment.

The strongest signal in the TOGA run is again not the same as the GAGO1 mode. The first canonical H500 pattern in the TOGA run (Figure 9c) is similar to the second canonical pattern in the GAGO experiment (the GAGO2 mode in Figure 9c) which is supposed to be associated with the El Niño phenomenon. This mode will be called the TOGA1 mode. The negative atmospheric anomaly over the North Pacific in the TOGA run is stronger than in the GAGO experiment and its center is shifted slightly northwards compared to the GAGO2 mode. The positive atmospheric anomaly over North America is more strongly developed than in the GAGO2 mode, increasing the resemblance of this mode to the PNA pattern of Wallace and Gutzler (1981). The structure of atmospheric anomalies over the North Atlantic sector in both experiments is also different. The first canonical SST pattern in the TOGA run (Figure 9d) looks like the second SST canonical pattern in the GAGO experiment. Both patterns have strong positive SST anomalies in the central and eastern tropical Pacific. The correlations of the time series of the TOGA1 mode with the ENSO3 SST index defined above are 0.51

for H500 and 0.78 for SST.

To verify again that the atmospheric variability associated with the GAGO1 mode in the TOGA run is not related to the tropical SST anomalies we calculated the correlation coefficients between the first canonical time series of SST in the GAGO experiment and anomalies of H500 in the TOGA run at each grid point. The correlations (not shown) are small with maximal values of about 0.3 over the North American continent. On the other hand, the time series of H500 associated with the GAGO1 mode calculated for the TOGA run is also weakly correlated with the tropical SST anomalies. Thus, similar to the MOGA run, the GAGO1 mode is not a good descriptor of the SST anomalies in the TOGA run.

6.5 The linear combination of the TOGA and the MOGA runs

The MOGA and TOGA runs do not reproduce the atmospheric signal found in the GAGO run as the first canonical pair of patterns. Some similarity was found between the first canonical SST patterns in extratropical regions in the GAGO and MOGA runs. However, the atmospheric signals in the Northern Hemisphere are significantly different in these experiments. Assuming that the influence of SST on the atmosphere is linear, i.e. the atmospheric response to the SST anomalies in the GAGO run is the sum of the responses to SST anomalies in the middle latitudes and in the tropics, one might expect the same results as in the GAGO run if the CCA is applied to the sum of the geopotential height anomalies from the MOGA and the TOGA runs and to the global SST field.

However, the first canonical pattern of the linearly combined H500 fields (not shown) appeared to be quite different from the GAGO1 mode. It is rather similar to the GAGO2 mode or to the TOGA1 mode. The corresponding SST pattern resembles the El Niño mode. Therefore the atmospheric response in the linearly combined data is different from the GAGO1 mode and it seems that nonlinear interactions between midlatitudes and tropics play an important role in the atmospheric circulation and its response to SST anomalies.

6.6 Atmospheric circulation and SST gradient

Palmer and Sun (1985) assumed that the transient eddies could be of decisive importance for the extratropical atmospheric response. Since the baroclinic activity depends partly on the SST gradients, another possible reason why neither the MOGA nor the TOGA run is able to reproduce the strongest atmospheric response found in the GAGO experiment could be a wrong representation of the meridional SST gradient near $30°N$ in the MOGA and the TOGA runs. At this latitude the observed and climatological SST values come together in these runs so that artificial meridional SST gradients in this region arise. If the correct values of the SST gradient are important for the atmospheric response, then the results of the MOGA and the TOGA runs could be inconsistent with those of the GAGO run.

To have an idea about the relationship between atmospheric anomalous circulation and the SST gradient, we computed the linear regression coefficients between the time series of the first canonical patterns of H500 in the GAGO and MOGA runs and the meridional SST gradient at each grid point in the Northern Hemisphere. The obtained distributions of the regression coefficients are shown in Figure 9. The GAGO run reveals a relatively strong relation between the GAGO1 atmospheric mode and SST gradients in the North Atlantic at $20°N - 30°N$ and at about $45°N$ off Newfoundland as well as in the central and western North Pacific at $15°N$ and at $30°N$ (Figure 9a). The MOGA1 mode is related to a relatively strong SST gradient anomaly in the western North Atlantic and the central North Pacific north of $30°N$.

The main anomalies of the SST gradient which are related to the MOGA1 mode are placed slightly further northwards of their position in the GAGO run. Particularly, the negative SST gradient anomaly in the western and central North Pacific in the MOGA is located fully north of $30°N$ whereas in the GAGO run it is spreading from about $20°N$ to $45°N$. A strong positive SST gradient anomaly in the MOGA run is located in the North Atlantic at the US coast and in the central North Pacific at $25°N - 30°N$, i.e. exactly in the regions where the observed SST anomalies occur together with the climatological SST values. In the GAGO run the subtropical SST gradient anomaly in the North Atlantic is of more moderate amplitude than in the MOGA run and covers the whole area between the North American coast and the African continent at $15°N - 30°N$.

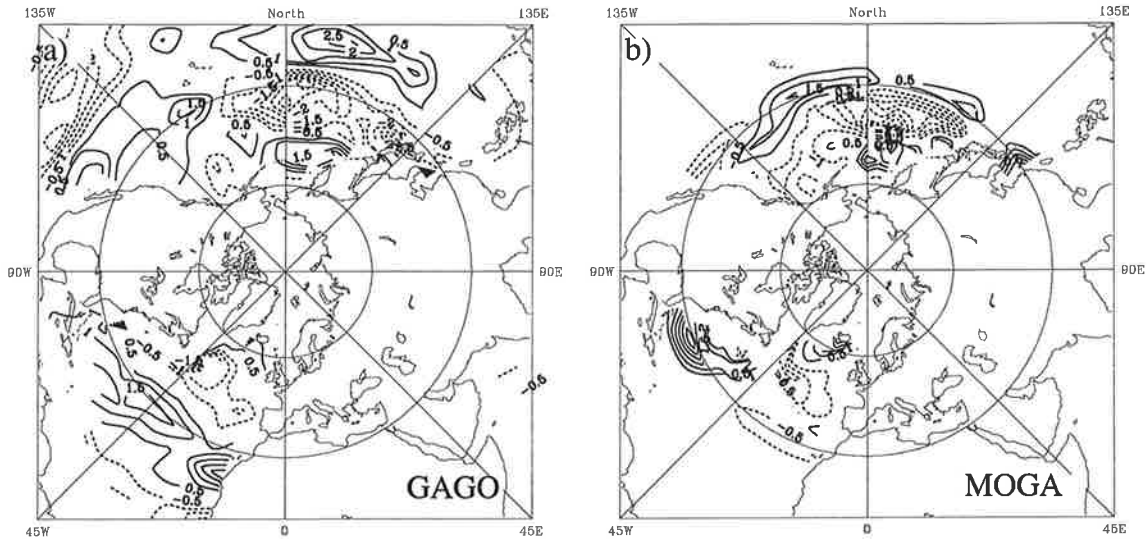

Figure 26: *The distribution of linear regression coefficients between the time component of the first canonical pattern of Northern Hemisphere H500 and meridional SST gradient in the GAGO run (a) and between the time component of the first canonical pattern of Northern Hemisphere 500 hPa geopotential height and meridional SST gradient in the MOGA run (b). Contour interval is* $0.5 \cdot 10^{-7} K/m$. *Labels are scaled by* 10^{-7}.

6.7 Summary of GCM results

To obtain an overview over all the experiments (GAGO, MOGA, TOGA and CONTROL) we reduced some of the results of the CCA into Table 9. For each GCM run (GAGO, MOGA, TOGA and CONTROL) we calculated time series associated with the atmospheric canonical mode described above (GAGO1, GAGO2, MOGA1 and TOGA1). Table 9 presents the variance of these time series in each run normalized by the corresponding variance in the CONTROL run. This value characterizes the relative strength of canonical modes in each GCM run compared to the CONTROL run. The correlation between time series associated with atmospheric modes in each run and the corresponding to these modes canonical time series of SST are also shown to demonstrate the relationship of atmospheric modes to SST anomalies.

From Table 9 one can see that the variance of the GAGO1 mode in the GAGO run is almost twice as large as in the MOGA and TOGA runs. The variance of the GAGO2 mode is largest in the TOGA run (more than twice as large as in the CONTROL run) and is relatively large in the GAGO run. The MOGA1 mode has nearly the same variance in all GCM experiments. The variance of this mode in the MOGA run does

	GAGO run	MOGA run	TOGA run	CONTROL run
GAGO1	var=1.60	var=0.85	var=0.89	var=1.00
MODE	cor=0.66	cor=-0.14	cor=-0.01	cor=0.16
GAGO2	var=1.98	var=1.26	var=1.98	var=1.00
MODE	cor=0.61	cor=-0.06	cor=0.42	cor=0.18
MOGA1	var=0.89	var=1.05	var=0.86	var=1.00
MODE	cor=0.31	cor=0.61	cor=-0.06	cor=-0.16
TOGA1	var=1.64	var=0.91	var=2.14	var=1.00
MODE	cor=0.24	cor=-0.07	cor=0.65	cor=-0.07

Table 2: *The variance of the time series associated with the canonical modes in each GCM run normalized by that in the CONTROL run together with the correlation coefficients between these time series and the corresponding canonical time series of SST.*

not significantly exceed that of the CONTROL run. The TOGA1 mode is strongly presented in the TOGA and in the GAGO runs whereas the variance of this mode in the MOGA run is nearly the same as in the CONTROL run.

The first canonical time series of SST in the GAGO run is well related to the GAGO1 mode only in the GAGO experiment. The correlation is in this case 0.63. Since there is no SST variability in the CONTROL run, except the annual cycle, correlation values presented in the corresponding column characterize the level of correlations which could occur just by chance even if the atmospheric circulation is independent of SST anomalies. One can see that correlations less than 0.2-0.3 should be considered as statistically insignificant. The second canonical time series of SST in the GAGO run is relatively well correlated with the GAGO2 mode in the GAGO run itself and in the TOGA experiment. The canonical SST time series of the MOGA1 and the TOGA1 modes are well related to the corresponding time series of H500 only in the MOGA and the TOGA runs, respectively.

7 Normal mode analysis of the barotropic operator

As it has been mentioned in the previous sections, the atmospheric anomalies produced in the GAGO, MOGA and TOGA runs and in the long term GCM experiments are of large scale and equivalent-barotropic. Thus we might expect that the main dynamical features of the atmospheric response can be captured by a nondivergent barotropic vorticity equation model. Such a simplified model cannot reproduce the whole chain of physical mechanisms involved in the formation of an atmospheric anomaly as a response to SST anomalies. However it still describes processes important for atmospheric variability on intra- and interannual time scales, such as Rossby wave propagation and the development of barotropic instability in a zonally asymmetric flow.

The use of linear barotropic models is not new in studies on internal atmospheric variability and atmospheric response to SST anomalies. Branstator (1985 a,b), for example, applied such a model to reproduce a midlatitude atmospheric response of NCAR's Community Climate Model to central tropical Pacific SST anomalies. He found that much of the structure of the pattern can be reproduced by the linear model if it is forced by a vorticity source/sink in approximately the same geographical location as the SST anomaly. The problem of the atmospheric response to extratropical SST anomalies is more complicated since there is no obvious relationship between the forcing term and the SST anomalies. A linear model can only supply us with general ideas about possible reactions of the atmosphere and about processes which can play an important role in this subject.

In a recent paper of Metz (1994) a linearized barotropic model was used to compute singular modes (Schmidt modes) of a linear operator which under certain conditions represent the EOFs of a linear stationary noise-forced model (Dymnikov, 1988; Navarra, 1993). He showed that the leading EOF of the linear stationary barotropic model linearized about the 300 hPa basic state and driven by the forcing evaluated from the GCM run is very similar to the leading singular mode of the linear operator. On the other hand, he demonstrated that the leading singular mode associated with the equivalent-barotropic level basic state matches quite well the GCM low frequency variability mode of the atmosphere.

There are several strong assumptions and caveats in using linear barotropic models. The first problem is the treatment of the nonlinear terms. Since deviations of

the atmospheric flow from the basic state are not generally small, nonlinear terms can significantly influence the dynamics of the atmosphere. Another open problem in linear barotropic models is the choice of the basic state. Some authors (Branstator, 1985a,b) recommended the use of the 300 hPa level. Metz (1994) found, however, that the equivalent-barotropic basic state produced more realistic planetary waves. Finally, the formulation of linear drag in such models is not obvious. A constant linear drag coefficient has no influence on the spatial structure of normal modes. But the growth rates of unstable normal modes and the amplitude of the eigenvalues depends crucially on this parameter.

Let us consider now the nondivergent barotropic vorticity equation on the sphere

$$\frac{\partial \nabla^2 \psi}{\partial t} + J(\psi, \nabla^2 \psi + f) + \alpha \nabla^2 \psi + \mu \nabla^6 \psi = F. \tag{43}$$

Here ψ is the stream function, f is the Coriolis parameter, α is the linear drag coefficient and μ is the horizontal diffusion coefficient. F on the right hand side stands for external forcing.

Equation (43) can be rewritten in terms of disturbances of the streamfunction ψ' from the time-independent basic state $\overline{\psi}$ as follows

$$\frac{\partial \nabla^2 \psi'}{\partial t} + J(\psi', \nabla^2 \overline{\psi} + f) + J(\overline{\psi}, \nabla^2 \psi') + J(\psi', \nabla^2 \psi') + \alpha \nabla^2 \psi' + \mu \nabla^6 \psi' = F' \tag{44}$$

where $F' = F - \overline{F}$ and $\overline{F} = J(\overline{\psi}, \nabla^2 \overline{\psi} + f) + \alpha \nabla^2 \overline{\psi} + \mu \nabla^6 \overline{\psi}$. For small enough perturbations ψ' the nonlinear term $J(\psi', \nabla^2 \psi')$ in (44) can be neglected. In the absence of external forcing ($F' = 0$) we have an equation describing the internal dynamics of the linear barotropic model

$$\frac{\partial \psi'}{\partial t} + \mathcal{A}\psi' = 0 \tag{45}$$

with the linear operator $\mathcal{A}\psi' = \nabla^{-2}(J(\psi', \nabla^2 \overline{\psi} + f) + J(\overline{\psi}, \nabla^2 \psi') + \alpha \nabla^2 \psi' + \mu \nabla^6 \psi')$. In deriving (45) we supposed that all functions in the equation (44) are orthogonal to a constant so that we are allowed to apply the inverse Laplacian operator ∇^{-2} to both sides of (44).

Searching for solutions of (45) in the form $\psi'(\lambda, \phi; t) = \psi(\lambda, \phi) e^{-\omega t}$ we obtain the following eigenvalue problem

$$\mathcal{A}\psi = \omega \psi. \tag{46}$$

Eigenvectors $\{\psi_j\}$ of the operator $\mathcal{A}$ barotropic normal modes. Since the operator $\mathcal{A}$ is not Hermitian its eigenvalues and eigenvectors are complex in general. Normal modes with a negative real part ω_j^r of the corresponding eigenvalue are unstable with e-folding time $T_r = 1/\omega_j^r$. The nonzero imaginary part ω_j^i defines the time period $T_i = 2\pi/\omega_j^i$ of travelling normal modes. The imaginary part of complex normal modes represents the structure of the atmospheric anomalies a quarter of the time period after the real part of the mode. Normal modes with purely real eigenvalues are stationary planetary waves.

In the case of very low frequency variability, or for stationary solutions, we can make further simplifications. Averaging the equation (44) over a long time period and supposing that all normal modes of the operator $\mathcal{A}$ are stable (or, at least that growth times of all unstable modes are much larger than the characteristic time scale of low frequency variability), we can neglect in the first approximation the time derivative in equation (44):

$$J(\widehat{\psi'}, \nabla^2\overline{\psi} + f) + J(\overline{\psi}, \nabla^2\widehat{\psi'}) + J(\psi', \widehat{\nabla^2\psi'}) + \alpha\nabla^2\widehat{\psi'} + \mu\nabla^6\widehat{\psi'} = \widehat{F'}, \tag{47}$$

or, in terms of the operator $\mathcal{A}$

$$\mathcal{A}\widehat{\psi'} + \nabla^{-2}J(\psi', \widehat{\nabla^2\psi'}) = \mathcal{F}'. \tag{48}$$

Here $\widehat{\cdot}$ stands for time averaging and $\mathcal{F}' = \nabla^{-2}\widehat{F'}$. To simplify (48) the nonlinear term is parameterized by a linear diffusion scheme like

$$J(\psi', \widehat{\nabla^2\psi'}) \simeq \mu_{add}\nabla^6\widehat{\psi'} \tag{49}$$

with a constant coefficient μ_{add}. Such a parameterization means that the total time averaged effect of nonlinear dynamical processes is equivalent to an additional diffusivity. Nevertheless, we accepted this hypothesis as a first order approximation to get a linear equation. Finally we obtain the following linear problem

$$\mathcal{A}'\widehat{\psi'} = \mathcal{F}'. \tag{50}$$

Here the operator $\mathcal{A}'$ has the same form as in equation (46) but with the diffusion coefficient $\mu_{tot} = \mu + \mu_{add}$. In the following we will omit for simplicity a prime $'$ for the operator $\mathcal{A}'$.

Suppose that the set of the normalized eigenvectors ψ_j of the operator $\mathcal{A}$ builds a full basis. In the real situation we always deal with a phase space of finite dimension

N, and therefore we replace the linear operator $\mathcal{A}$ by a matrix of size $N \times N$ and the functions $\widehat{\psi'}$ and $\mathcal{F}'$ by vectors of dimension N. If the eigenvalues of the matrix are all different, then its eigenvectors build a full basis in N-dimensional space. Thus we can write the forcing term $\mathcal{F}'$ as an expansion in terms of the eigenvectors of the operator $\mathcal{A}$

$$\mathcal{F}' = \sum_j \phi_j \psi_j. \tag{51}$$

The scalar coefficients ϕ_j of the forcing term can be found from the relation

$$\phi_j = \langle \mathcal{F}', \psi_j^* \rangle. \tag{52}$$

Here $\langle \cdot, \cdot \rangle$ denotes a scalar product on the sphere and ψ_j^* is the eigenvector of the adjoint operator $\mathcal{A}^*$ which corresponds to the eigenvalue ω_j^*. The solution of (50) can be then found in the form

$$\widehat{\psi'} = \sum_j a_j \psi_j \tag{53}$$

with scalar coefficients a_j defined as

$$a_j = \frac{\phi_j}{\omega_j}. \tag{54}$$

Thus the magnitude of the coefficient a_j of the solution of (50) is proportional to the amplitude of the projection of forcing $\mathcal{F}'$ onto the adjoint eigenvector ψ_j^* and is inversely proportional to the amplitude of the corresponding eigenvalue.

The basic state $\overline{\psi}$ was derived from the winter model climate at 500 hPa. All fields were represented in spectral form and truncated at wave number 21 analogously to the ECHAM2/T21 model. Assuming that the basic state in the Southern Hemisphere does not influence the barotropic normal modes in the Northern Hemisphere, the basic state was antisymmetrically extrapolated into the Southern Hemisphere and only antisymmetric spherical harmonics were retained in the spectral presentation of all fields. By doing so we reduced the size of the complex nonsymmetric matrix which approximates the operator $\mathcal{A}'$ in (50) to 231×231. The eigenvalue problem (46) was solved using a standard procedure from the NAG-library. The details of the basic state derivation from the H500 field are presented in Appendix C.

A constant linear drag coefficient α only shifts the eigenvalues of the operator $\mathcal{A}$ along the real axis and does not influence the spatial structure of the eigenvec-

tors. The eigenvalue problem was solved for the horizontal diffusion coefficient μ_{tot} which corresponds to damping times for the shortest model scales of 0.65 days. In the ECHAM2/T21 model the diffusion coefficient is smaller and corresponds to damping times for the shortest model scales of 1.12 days. Additional numerical tests indicated that the general structure of the normal modes is rather insensitive to the value of the horizontal diffusion.

The normal modes presented in the following subsections are ordered according to the amplitude of the corresponding eigenvalues. So, the first normal mode has the smallest eigenvalue, the second mode has the second smallest eigenvalue etc. According to (54), normal modes with smallest eigenvalues would mainly contribute into the solution of (50) under the condition that the magnitude of projections of forcing onto the adjoint eigenvectors ϕ_j is of the same order for all j.

7.1 Normal modes of the operator $\mathcal{A}$

The first two normal modes of the linear operator $\mathcal{A}$ computed for the winter climate in the GAGO experiment and the first normal mode of the observed climate are shown in Figure 9. For better comparison with the results of previous sections the stream function of normal modes was transformed to geopotential height by means of the balance equation $\nabla^2\Phi = \nabla \cdot f\nabla\psi$. All normal modes appeared to be stable even for zero linear drag coefficient. Thus, at least in this formulation the internal instability of barotropic flow on monthly time scales in the absence of external forcing can play only a limited role in atmospheric variability.

The first mode is nearly stationary with a time period $T \simeq 300$ days. The real part of the first mode (Figure 9a) resembles very much the stationary response in the long term experiment PD4LT (Figure 9a) as well as the first canonical patterns of H500 found in the GAGO run and the first EOF of H500 in the GAGO run and in other GCM runs. Negative anomalies are located over the northern parts of the North Atlantic and North Pacific Oceans. Positive anomalies are placed south of the negative anomalies as well as over the North American continent, South Europe and over the Japan Sea. These aspects are common to the leading variability modes found in the GCM runs. The imaginary part (Figure 9b) has a positive anomaly around the North Pole and negative anomalies over North America, the North Sea and East Siberia.

The second normal mode (Figure 9c) is stationary. It is located mainly in the North Atlantic sector. Except a rather strong feature around the North Pole, the structure of

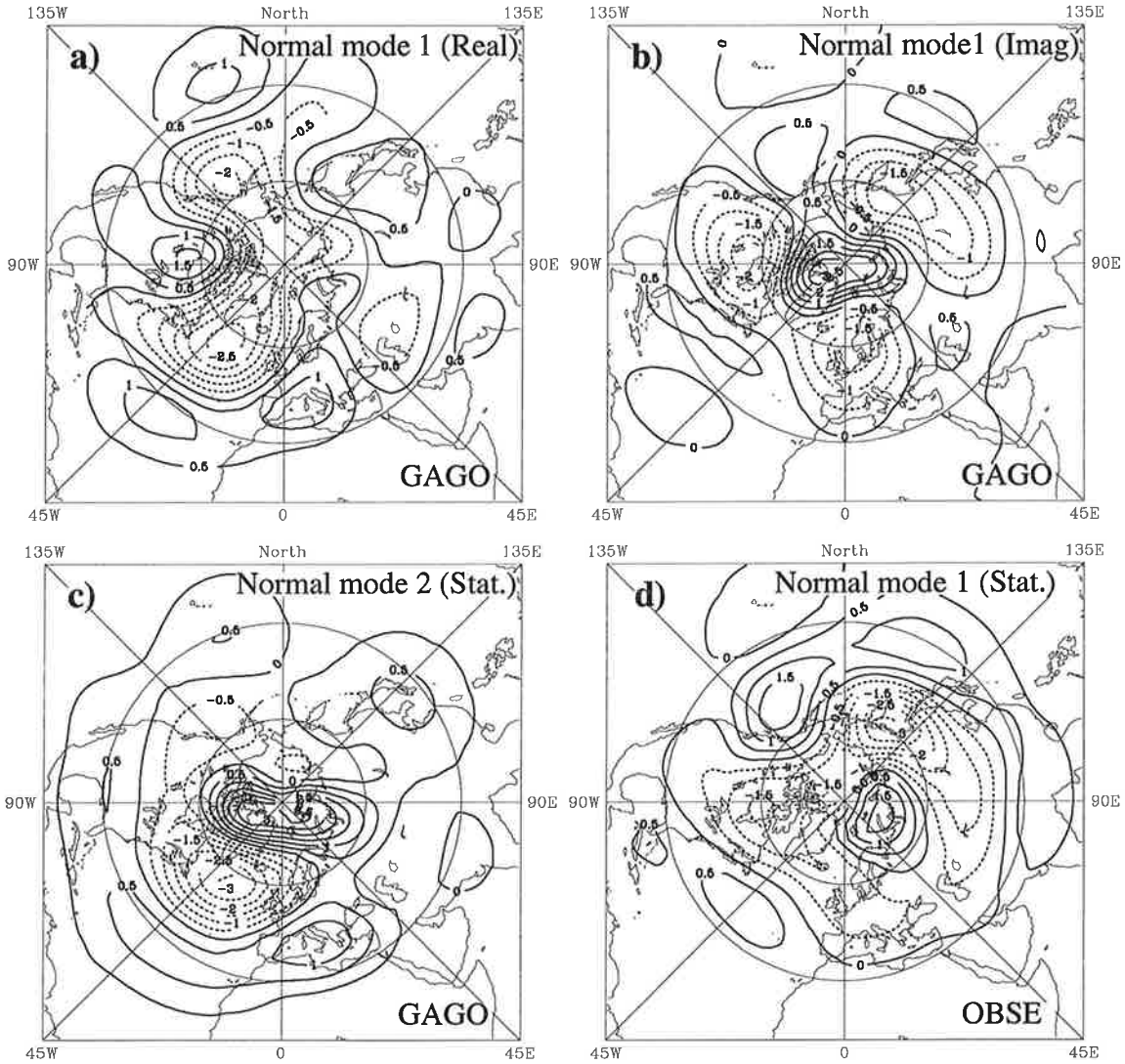

Figure 27: *The first (a, real part; b, imaginary part) and the second (c, stationary mode) normal modes of the barotropic operator linearized about the winter climate of the GAGO run and the first normal mode of the observed climate (d, stationary). Contour interval is 0.5.*

the second normal mode is similar to the structure of the real part of the first normal mode in the North Atlantic. The second mode in moderate latitudes is also similar to the stationary signal in the ND4LT run (Figure 9d) and to the first canonical mode found in the MOGA run. It seems that the first two normal modes contribute mainly to the monthly atmospheric variability in the GCMs and to the atmospheric response to the SST anomalies.

The first two normal modes computed for the other GCM runs are very similar to the normal modes described above. The first normal modes in the MOGA and in the TOGA runs are again nearly stationary with a time period of 480 days. The second normal modes are stationary in these runs. The pattern correlations between the first two normal modes in the GAGO run and the corresponding modes in the MOGA and TOGA run exceed 0.9. In the CONTROL run the resemblance is somewhat weaker. The first normal mode in the CONTROL run has time period of more than 10 years with very similar real and imaginary parts. The second mode is stationary and resembles the first normal mode. The pattern correlation of the first two normal modes in the CONTROL run with the real part of the first mode in the GAGO run is of the order of 0.7.

The first normal mode computed for the observed climate is shown in Figure 9d. There is no obvious correspondence between this mode and the observed leading EOFs in Figure 9 as it is the case for the GCM climate. The main anomalies in the first normal mode are, however, located in the North Pacific sector. Some similarity with the PNA-type pattern can be found in the east Pacific / North America sector. Particularly, negative anomalies are placed in the subtropical North Pacific and over the north of North America. Positive anomalies are found in the north-east of the North Pacific and in the south-west of the North Atlantic. However, the negative center over the east of Russia has a much stronger amplitude and is placed further south and east as it is the case in the first observed EOF. The second normal mode (not shown) is nearly stationary with a time period over 400 days and is similar to the first normal mode in the GAGO run.

It can be hardly expected that the normal modes of a simple linear barotropic model would have strong resemblance to the leading modes of the atmospheric variability. Remarkably, however, that at least the very crude structure of the first two normal modes is common to the structure of the leading EOFs. Especially in the GCMs, where the variability mode associated with the first EOF is very dominant and well separated from the second EOF, the correspondence is relatively good. For the observed climate

the results are less satisfactory. Note, however, that the observed basic state in the tropical area south of $20°N$ was derived from the CONTROL climate (see Appendix C) so that the details of the basic flow in this area can influence the results of the normal mode analysis.

7.2 Eigenvectors of the adjoint operator $\mathcal{A}^*$

According to (52) the scalar coefficients ϕ_j in the expansion of the external forcing $\mathcal{F}'$ in terms of the eigenvectors of the operator $\mathcal{A}'$ are the projections of the forcing onto the adjoint eigenvectors ψ_j^*. Thus, the spatial structure of the adjoint eigenvectors represents an anomalous vorticity forcing which excites the corresponding normal modes most efficiently.

The eigenvectors of the operator $\mathcal{A}^*$ which correspond to the normal modes presented above are shown in Figure 9. The real part of the first eigenvector (Figure 9a) has anomalies with large amplitudes over the western North Pacific. The anomalies have the form of zonally oriented belts. In the imaginary part of the first adjoint mode (Figure 9b), in the second adjoint eigenvector (Figure 9c) in the GAGO run and in the first adjoint mode of the observed climate (Figure 9d) anomalies of large amplitude are found over the western parts of the both basins. The centers of action in the adjoint eigenvectors are in the vicinity of zones of strong baroclinic activity over both oceans. Shifting of the storm tracks in the north-south direction, and/or, intensification/weakening of transient eddy activity in these regions due to SST anomalies leads to variability of the high-frequency forcing of the time mean circulation. Recent studies of the atmospheric response to SST anomalies in the midlatitudes (Palmer and Sun, 1985; Lau and Nath, 1990; Fraedrich et al., 1993) also support the idea that transient eddy forcing can play an important role in the formation of large scale circulation anomalies.

Metz (1989) investigated the relation between low-frequency atmospheric variability and transient forcing on the base of six winters of ECMWF analysis. He applied the canonical correlation analysis to the low-pass filtered streamfunction and the pattern that results from the effects of cyclone-scale eddies on the mean circulation. Low frequency counterparts of the first two canonical modes were of planetary scale. Canonical patterns, which represented the eddy effects, were locally concentrated over the North Pacific and North Atlantic. The canonical patterns of eddy forcing had a similar elongated structure as the adjoint eigenvectors described above.

Since the variability of the storm tracks is at least partly related to the extratropical

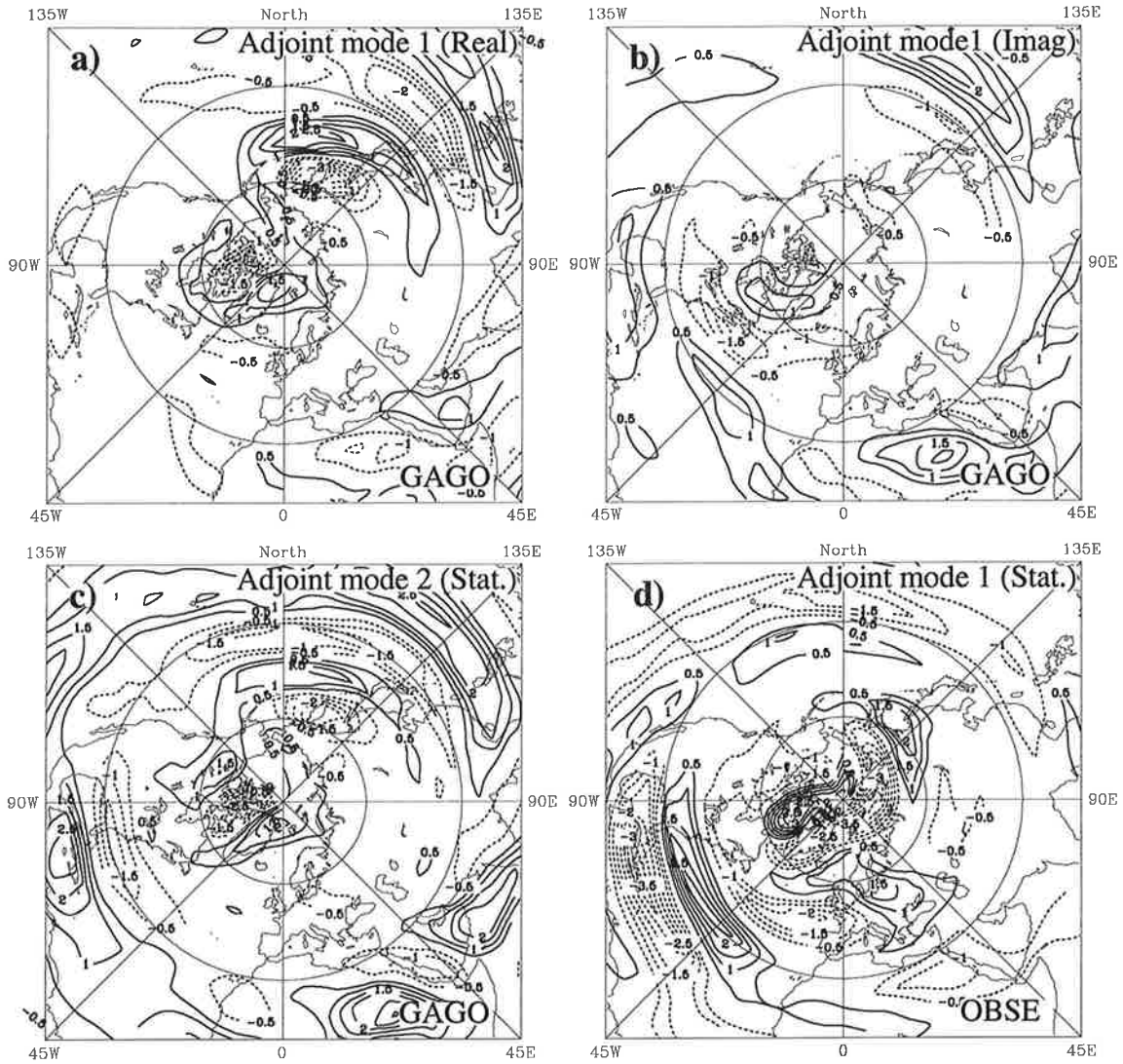

Figure 28: *The first (a, real part; b, imaginary part) and the second (c, stationary) eigenvectors of the adjoint barotropic operator linearized about the winter climate of the GAGO run and the first adjoint eigenvector of the observed climate (d, stationary). Contour interval is 0.5. Zero line is omitted.*

SST gradients it is interesting to compare the adjoint barotropic modes with the SST gradient patterns associated with the canonical modes shown in Figure 9. For the GAGO1 mode the SST gradients anomalies are generally larger in the North Pacific than in the North Atlantic. In the adjoint eigenvector which corresponds to the normal mode like GAGO1 mode (the real part of the first normal mode in the GCMs) the main anomalies are located also in the North Pacific. In the MOGA run a relatively strong and presumably artificial SST gradient anomaly is located also in the North Atlantic. The second adjoint vector which is associated with the normal mode like the MOGA1 canonical mode has large anomalies over the both oceans.

8 Summary and conclusions

8.1 SST sensitivity GCM experiments with constant SST anomalies

The extratropical atmospheric response to SST anomalies in the North Atlantic in winter was studied by means of the Hamburg version of the ECMWF general circulation model ECHAM2/T21. Several kinds of GCM experiments have been done. The stationary atmospheric response was examined in the long term GCM integrations. In these experiments the GCM was integrated over the time period of 24 to 30 months. The atmospheric system was assumed to be in a new equilibrium state which was compared with the climate state of the undisturbed control run. The nonstationary transient period and the dynamical processes involved in the formation of the atmospheric response during the first several weeks were studied my means of Monte-Carlo simulations. This set of GCM experiments was made for the time period of 3 months, starting from different statistically independent initial conditions.

The main goal of this GCM experiments with constant SST anomalies was to determine the dynamical mechanisms which are relevant for the development of the extratropical atmospheric response to SST anomalies in the midlatitudes of the North Atlantic. The linearity and the dependence of the atmospheric response on the geographical localization of SST anomalies was also examined.

The formation of the atmospheric response can be subdivided into three stages: 1) generation of anomalous potential vorticity over SST anomalies and its advection by the mean flow, 2) propagation of planetary Rossby waves and 3) the establishment of the stationary response. Of course, such a classification of the mechanisms involved in the development of the atmospheric response is only formal. All the processes occur at the same time and one may say only on a relative importance of this or that process at the certain stage.

Right after the beginning of the integrations with introduced SST anomalies the response is localized over the SST anomalies. All processes related to the planetary spatial scale may be neglected at this stage. The response is baroclinic in the vicinity of the heat source with negative (positive) height anomalies right over the warm (cold) SST anomalies and height anomalies of the opposite sign in the middle and upper troposphere. Since the amplitude of the signal is small at this stage compared to the amplitude of the natural atmospheric disturbances, the response behaves linearly with

respect to the sign of SST anomalies. The structure of the atmospheric response is rather insensitive to the details of the basic flow and depends mainly on the structure of the SST anomaly pattern.

The produced vorticity anomalies are advected downstream by the mean circulation. The amplitude of vorticity anomalies is steadily growing and their spatial scale becomes larger. The meridional variations of the mean potential vorticity cannot be more neglected for large scale waves. Planetary Rossby waves of equivalent-barotropic structure propagate away from the source. The trajectories of Rossby wave propagation deviate only little from the great circles on the sphere.

Due to internal diffusion and friction in the planetary boundary layer all non-stationary waves disappear after about two weeks. The stationary atmospheric response is dominated by the equivalent-barotropic component. Barotropic mode analysis presented in the last section of this study indicates that the structure of the stationary signal depends decisively on the details of the zonally asymmetric mean flow and on the structure of the external forcing. Normal modes of the barotropic operator linearized about the model climate were computed and compared to the atmospheric response in the GCM experiments. The spatial structure of the stationary response to the dipole SST anomaly in the North Atlantic appeared to be similar in many aspects to the structure of the most unstable and near resonant normal mode.

The corresponding eigenvectors of the adjoint operator, which represent an external forcing optimal for exciting normal modes, have a longitudinal structure with maxima in regions characterized by enhanced high-frequency baroclinic activity over both oceans. Such a structure suggests that small meridional variations of the vorticity forcing in these regions would lead to a large variability of the corresponding normal modes. The barortopic transient eddy forcing tends to support the atmospheric response.

The GCM experiments with SST anomalies in different geographical regions indicate that the atmospheric reaction is very sensitive to the position of the SST anomaly. Especially strong atmospheric response in this particular GCM was found only in the case of the positive SST anomalies placed of the US coast. The response to SST anomalies east of Newfoundland was significantly weaker.

The amplitude of the stationary response to ± 4 K SST anomalies is comparable with that of the internal variability of the extratropical atmosphere. The response is not symmetric with respect to the sign of SST anomalies. The nonlinear behavior of the atmospheric signal cannot be exclusively attributed to the nonlinear dependence of Richardson number, which controls the turbulent heat exchange coefficient in the

parameterization of heat fluxes in the boundary layer, on SST.

8.2 GCM experiments with observed SST anomalies

The atmospheric wintertime interannual variability in several 19-year GCM runs with different types of SST forcing was examined by means of the EOF analysis. The leading modes of atmospheric variability in GCMs were found to be substantially different from the observed ones. Particularly, the first model EOF of H500 has a global structure with negative anomalies over the northern parts of the North Atlantic and North Pacific and in polar regions and positive anomalies roughly south of the negative ones. The first observed EOF, on the contrary, has main anomalies over the North Pacific. The first two EOFs in the GCM are stronger separated than in the observations.

The results of the EOF analysis indicate that the atmospheric variability in the GCMs is dominated by an internal mode which is not quite common for the observed circulation. This circumstance complicates the direct comparison of the atmospheric anomalies in the GCM experiments with the observed ones. The details of the atmospheric response in the extratropics are probably not correctly reproduced compared to the observations. Thus, the GCM results in this study can be considered with care. They demonstrate only the potential effect of the SST forcing in different geographical regions on the atmospheric circulation and reveal the dynamical mechanisms which can be relevant for the observed air-sea interactions.

The CCA was used to find the best correlated pair of patterns of SST in the North Atlantic and Pacific and atmospheric circulation in the Northern Hemisphere. In the GAGO and MOGA experiments the atmospheric response over the North Atlantic area was found to be a part of global patterns. The best correlated pattern of Northern Hemisphere geopotential height at 500 hPa in the GAGO run is global and is related to SST anomalies in the North Atlantic and the North Pacific. It resembles the leading variability mode in the GAGO run. The statistical significance of the canonical correlation for the GAGO1 mode is very high. The variance explained by the first canonical pattern of H500 is much higher than for the other experiments (1.6 times as large as in the CONTROL run and almost twice as large as in the MOGA and the TOGA runs). This mode is quite robust and insensitive to the number of the EOFs and the choice of geographical regions or SST anomalies used in the CCA.

In the MOGA experiment the atmospheric signal in the Northern Hemisphere is weaker than in the GAGO run. The first canonical pattern of H500 differs from the

GAGO1 mode, despite the fact that the corresponding canonical pattern of SST is similar in midlatitudes to the first canonical SST pattern in the GAGO run. The variance explained by the MOGA mode is approximately the same in all GCM integrations, including the CONTROL run. It seems that in the MOGA run another type of atmospheric variability mode is excited by extratropical SST anomalies. However the signal is weak and probably not very stable.

The El Niño type mode was found as the first canonical pair of patterns in the TOGA run and as the second canonical mode in the GAGO run. The variances explained by the GAGO2 and the TOGA1 atmospheric modes in both runs are about twice as large as the magnitude of those in the CONTROL integration and the MOGA run. It seems that for the El Niño mode, tropical SST anomalies are of essential importance which is consistent with the previous results (e.g. Graham et al., 1994). The tropical SST anomalies in the Pacific associated with the El Niño phenomenon have, on the contrary, no influence on the GAGO1 mode in the GAGO experiment.

Neither the MOGA and the TOGA runs alone, nor their linear combination is able to reproduce the signal found in the GAGO run as the first canonical mode. The nonlinear effects and the interactions between midlatitudes and tropics seem to be important. Artificial meridional SST gradients at $25°N - 30°N$ in the MOGA and the TOGA runs probably influence the atmospheric response in these GCM experiments. The last effect represents a real problem in the experiments like GAGO-MOGA-TOGA by means of which the relative importance of the SST forcing in the middle latitudes and in the tropics is intended to be investigated. Particularly, in the MOGA run the first canonical pattern of H500 seems to be related to the artificial SST meridional gradients in the North Atlantic and North Pacific at $25°N - 30°N$.

A normal mode analysis was performed in order to explain the discrepancies between the leading atmospheric variability modes in the GCM and in the observations. The leading normal modes of the barotropic operator linearized about the winter climate at 500 hPa in the GCMs were compared with the canonical modes and the EOFs. The first two normal modes in the GCM runs were found to have some similarity to the leading variability modes in the GCMs. Particularly, the spatial structure of the real part of first nearly stationary mode is very similar to the structure of the GAGO1 mode. The second normal mode is, at least qualitatively, similar to the MOGA1 canonical mode.

The first normal mode for the observed winter climate differs significantly from the first two normal modes in the GCMs. The resemblance of the observed first normal mode to the leading mode of the observed variability is, however, relatively weak. The

largest anomalies in the observed first normal mode are located in the North Pacific. Some similarity to the observed first EOF is found in the eastern North Pacific / North America sector.

Eigenvectors of the adjoint operator display the structure of the forcing which excites the normal mode most efficiently. Leading adjoint vectors have strong zonally elongated anomalies over the eastern parts of the North Pacific and the North Atlantic oceans in the extratropics i.e. in the regions where the strongest transport of the heat and momentum occur in the troposphere. The variability of the storm tracks which is partly related to the SST variability in the extratropics can significantly influence the variability of nearly resonant barotropic normal modes.

Observational studies (e.g. Zorita et al., 1992) indicate that the atmospheric disturbances usually lead the extratropical SST anomalies on monthly time scales. The atmospheric response in the GCM experiments with prescribed SST anomalies occur, on the contrary, at best simultaneously with SST variations or lag them. Thus, they demonstrate possible feedbacks from the SST on the atmospheric circulation. As a result of such feedbacks, the amplitude or/and the persistence of the atmospheric and oceanic anomalies could increase (decrease) if the feedback is positive (negative). Particularly, if we assume that the atmospheric response found in the North Atlantic in the GAGO run as the first canonical pair of patterns or in the GCM experiment with the positive SST dipole in the North Atlantic is correctly represented (it might be not the case as discussed above), then such a response would positively contribute into the atmospheric anomalies which are known to be responsible for the appearence of the same SST anomalies in the North Atlantic.

9 Acknowledgements

It is a great pleasure for me to thank Dr. Hans von Storch for his assistance and intensive encouragement of the work. I highly appreciate his manifold help, constructive criticism and numerous fruitful discussions on the topic. My work on this study has greatly profited from his scientific and social experience.

I thank very much Professor Dr. Valentin P. Dymnikov who initiated this study and supplied me with many valuable suggestions and ideas. Numerous scientific discussions with him during his several visits at the Max-Planck-Institute for Meteorology have decisively contributed to the present study.

Special thank to the Foundation F.V.S. to Hamburg for giving me the possibility to come to Hamburg and to start the research work. I thank Professor Dr. Klaus Hasselmann for the possibility to make my Ph.D. thesis at the Max-Planck-Institute for Meteorology where I enjoyed a very stimulated, warm and friendly atmosphere. I thank Professor Dr. Klaus Fraedrich for his friendly readiness to be a reviewer of this study.

A significant part of this study has been done in a close collaboration with Dr. Eduardo Zorita. His help, fresh ideas and sharp comments were very valuable for me. Heiko Borgert and Wolfgang Welke helped me to get along with computer facilities and with available software. I thank them very much.

I would like to thank Dr. Jin von Storch for a careful reading of the manuscript and her helpful comments and suggestions for improving the text. Numerous corrections and comments on earlier versions of the manuscript made by Victor Ocaña and Dr. Gabriele Hegerl were very useful.

The study has benefited from many discussions and stimulating talks I have had with colleagues at the Max-Planck-Institute and outside, especially with Dr. Ute Luksch, Dr. Ralf Weiße, Dr. Mojib Latif and Dr. Grant Branstator. I thank very much all of them.

Appendices

A Significance tests for canonical correlations

To define the statistical significance of canonical correlations we produced, for each GCM run, 200 CCAs under exactly the same conditions as described in Sections 6 (December-February, 5 EOFs for each variable) and with the same data except that the data fields were randomly rearranged in time so that the correlations between two fields were caused by chance. The purpose of this is to determine what values of correlation coefficients are significant in the CCA. The $x\%$ significance value was defined as the canonical correlation value for which the percentage of all 200 CCA cases with smaller canonical correlations was $x\%$. Particularly, in the CCAs for North Atlantic SST vs. North Atlantic SLP there were 198 cases (99%) with the first canonical correlations less than 0.646. Thus, the first canonical correlation higher than 0.646 is considered as 99% significant in this particular case. The same procedure is applied to the second canonical correlation.

Other statistical tests were performed to examine the expectation of the fact that the leading mode of atmospheric variability would appear as the first canonical pattern in the CCA. For this purpose we calculated the pattern correlations between the first EOF of atmospheric variability and the first canonical patterns appeared in the Monte-Carlo simulations of the CCA described above. The statistical significance of the pattern correlation was defined in the same way as the statistical significance of the canonical correlations. Particularly, in the CCAs for North Atlantic SST vs. North Atlantic SLP there were 198 cases (99%) with the pattern correlation between the first EOF of SLP in the North Atlantic and the first canonical pattern less than 0.646 (95%)

Table 9 summarizes the results of Monte-Carlo simulations.

B Glynn and Muirhead's test

Since the data sets are limited in time, covariance matrices involved in the calculation of canonical correlations are estimated only approximately. For example, if the time series are not long enough, leading eigenvalues of the covariance matrix tend to be overestimated and eigenvalues with higher numbers are underestimated. Thus, the

CCA	GAGO: SLP(NA) vs. SST(NA)			MOGA: SLP(NA) vs. SST(NA)			TOGA: SLP(NA) vs. SST(TR)			GAGO: H500(NH) vs. SST(NA)		
Level	1.C	2.C	P.C.	1.C	2.C	P.C.	1.C	2.C	P.C.	1.C	2.C	P.C.
70%	.514	.378	.825	.515	.387	.720	.522	.384	.727	.500	.378	.618
80%	.536	.406	.867	.540	.411	.775	.537	.405	.771	.521	.393	.696
90%	.562	.430	.913	.567	.432	.850	.571	.435	.830	.553	.421	.785
95%	.589	.447	.936	.590	.465	.879	.592	.451	.877	.582	.434	.816
97%	.600	.464	.937	.610	.470	.896	.608	.459	.879	.599	.456	.853
98%	.627	.475	.940	.620	.483	.902	.628	.465	.881	.606	.459	.883
99%	.641	.489	.941	.631	.487	.910	.644	.486	.887	.638	.489	.894
99.5%	.650	.508	.949	.664	.492	.917	.665	.490	.896	.652	.416	.894

(Continued)

CCA	GAGO: H500(NH) vs. SST(NP)			GAGO: H500(NH) vs. SST(GL)			MOGA: H500(NH) vs. SST(ML)			TOGA: H500(NH) vs. SST(TR)		
Level	1.C	2.C	P.C.	1.C	2.C	P.C.	1.C	2.C	P.C.	1.C	2.C	P.C.
70%	.518	.382	.706	.513	.378	.743	.516	.386	.675	.517	.375	.628
80%	.539	.400	.761	.529	.405	.797	.543	.406	.738	.537	.402	.690
90%	.575	.437	.838	.559	.431	.847	.582	.421	.797	.565	.452	.778
95%	.596	.460	.869	.601	.450	.876	.602	.456	.817	.599	.452	.794
97%	.621	.476	.880	.610	.460	.886	.617	.455	.842	.614	.468	.815
98%	.642	.485	.881	.637	.469	.904	.630	.469	.854	.631	.470	.826
99%	.655	.487	.897	.677	.495	.912	.632	.505	.869	.671	.481	.844
99.5%	.677	.493	.902	.703	.496	.931	.643	.520	.871	.680	.514	.852

Table 3: *The values of the first and the second canonical correlations (1.C and 2.C) and of the pattern correlation (P.C.) between the first atmospheric canonical pattern and the first EOF statistically significant at different levels, as obtained from Monte-Carlo simulations. NA, NP, GL, ML and TR are the abbreviations for "North Atlantic", "North Pacific", "Global", "Middle Latitudes", "Tropics", respectively.*

canonical correlations obtained as eigenvalues of a matrix which is the product of the covariance and inverse autocovariance matrices are estimated with errors.

Glynn and Muirhead (1978) proposed a technique which enables one to get corrected unbiased estimates of canonical correlations and their significance intervals. Input parameters for this approach are the length of time series, the number of EOFs retained in the CCA and the values of all canonical correlations. In Table 9 we present corrected values and their 95% significance intervals for the first and the second canonical correlations between the Northern Hemisphere H500 and the global SST in winter in the GAGO, MOGA and TOGA runs. Particularly, the unbiased value of the first canonical correlation in the GAGO run is 0.57 compared to 0.66 for its original value. In the MOGA run the corrected first correlation (0.49) differs significantly from the original first canonical correlation 0.61 and is 0.08 smaller than the unbiased first correlation in the GAGO run.

C The derivation of the basic state $\bar{\Psi}$

The stream function of the basic state is derived from the winter climate mean of H500 in the Northern Hemisphere, both for the model and observed climates. First the geostrophic zonal and meridional winds are calculated from the H500 field

$$U_g = -\frac{1}{fa}\frac{\partial \Phi}{\partial \phi}, \quad V_g = \frac{1}{fa\cos\phi}\frac{\partial \Phi}{\partial \lambda}.$$

After that the relative vorticity field is computed as follows

$$\nabla^2 \psi = \frac{1}{a\cos\phi}\left(\frac{\partial V_g}{\partial \lambda} - \frac{\partial U_g \cos\phi}{\partial \phi}\right)$$

The stream function is obtained by applying the inverse Laplacian operator to relative vorticity. Since the observed data were available only north of 20^o the geostrophic velocities U_g and V_g south of this latitude for the observed climate were estimated from the H500 field taken from the CONTROL run.

The obtained stream function in the Northern Hemisphere is antisymmetrically extrapolated into the Southern Hemisphere. Such an extrapolation may cause problems in the vicinity of the Equator. The stream function used for the basic state is defined uniquely except a constant and is not necessarily zero at the Equator. Thus, discontinuities of the stream function and related to them artificial zonal winds can appear

CCA	GAGO: SLP(NA) vs. SST(NA)	MOGA: SLP(NA) vs. SST(NA)	GAGO: H500(NH) vs. SST(NA)	GAGO: H500(NH) vs. SST(NP)
1.C	.73 (+95%) .66 .58 (unbias.) .38 (-95%)	.59 (+95%) .54 .39 (unbias.) .15 (-95%)	.68 (+95%) .61 .51 (unbias.) .29 (-95%)	.71 (+95%) .64 .55 (unbias.) .34 (-95%)
2.C	.45 (+95%) .38 .21 (unbias.) -.05 (-95%)	.41 (+95%) .44 .17 (unbias.) -.10 (-95%)	.59 (+95%) .45 .40 (unbias.) .15 (-95%)	.57 (+95%) .55 .36 (unbias.) .11 (-95%)

(Continued)

CCA	GAGO: H500(NH) vs. SST(GL)	MOGA: H500(NH) vs. SST(ML)	TOGA: H500(NH) vs. SST(TR)
1.C	.70 (+95%) .66 .54 (unbias.) .33 (-95%)	.67 (+95%) .61 .50 (unbias.) .27 (-95%)	.73 (+95%) .66 .58 (unbias.) .27 (-95%)
2.C	.64 (+95%) .61 .46 (unbias.) .23 (-95%)	.68 (+95%) .47 .50 (unbias.) .29 (-95%)	.49 (+95%) .40 .27 (unbias.) .01 (-95%)

Table 4: *The first and second canonical correlations in the GCM runs and their corrected unbias. values. The 95% significance interval is depicted above and below the unbiased correlations. NA, NP, GL, ML and TR are the abbreviations for "North Atlantic", "North Pacific", "Global", "Middle Latitudes", "Tropics", respectively.*

at the Equator if the stream function is extrapolated into the Southern Hemisphere antisymmetrically. Atmospheric waves propagating to the Equator can reflect from the zero wind line (e.g. Held, 1983). Therefore, tropical easterlies can play an important role for the resonant behavior of the atmospheric circulation. In the model 500 hPa winter climate there is a narrow area with easterlies almost everywhere in the vicinity of the equator. We added to the stream function of the basic state such a constant that after the extrapolation the smallest possible easterlies occur everywhere in the equatorial region.

List of Figures

List of Tables

References

Alexander R. C. and Mobley R. L., 1976: Monthly averaged sea-surface temperatures and ice-pack limits on a global grid. Mon. Wea. Rev. 104, 143-148

Anderson C. W., 1984 An introduction to multivariate statistical analysis. 2nd ed., Wiley and Sons, 480-520

Barnett, T. P., Heinz H.-D. and Hasselmann K., 1984: Statistical prediction of seasonal air temperatures over Eurasia. Tellus 36A, 132-146

Barnett T. P. and Preisendorfer R., 1987: Origins and levels of monthly and seasonal forecast skill for United States surface air temperatures determined by canonical correlation analysis. Mon. Wea. Rev. 115, 1825-1850

Bjerknes J., 1962: Synoptical survey of the interaction between sea and atmosphere in the North Atlantic. Geofys. Publ., 24, 116-145

Branstator G., 1985a: Analysis of general circulation model sea-surface temperature anomaly simulations using a linear model. Part I: forced solutions. J. Atmos. Sci. 42, 2225-2241

Branstator G., 1985b: Analysis of general circulation model sea-surface temperature anomaly simulations using a linear model. Part II: eigenanalysis. J. Atmos. Sci. 42, 2242-2254

Bretherton C. S., Smith C. and Wallace J. M., 1992: An intercomparison of methods for finding coupled patterns in climate data. J. Climate 5, 541-559

DKRZ: Deutsches KlimaRechenZentrum, 1992: The ECHAM3 atmospheric general circulation model. Technical Report No. 6, Edited by: DKRZ, Modellbetreuungsgruppe

Davis R. E., 1976: Predictability of sea surface temperature and sea level pressure anomalies over the North Pacific Ocean. J. Phys. Oceanogr. 6, 249-266

Dymnikov V. P., 1988: Relationship of natural orthogonal components of the fields of meteorological characteristics to the eigenfunctions of dynamical operators. Izv. Acad. Sci. Atmos. Ocean. Phys., 24, 493-496

Dymnikov V. P. and Filin S. K., 1985a: A study of correlations between sea surface temperature anomalies in midlatitudes and anomalies of heating based on data from the First GARP Global Experiment. Reprint of the Department of Numerical Mathematics of the USSR Academy of Sciences, No. 83, Moscow, USSR (in Russian)

Dymnikov V. P. and Filin S. K., 1985b: Numerical simulation of the atmospheric response to sea surface temperature anomalies in North Atlantic. Reprint of Depart-

ment of Numerical Mathematics of the USSR Academy of Sciences, No. 84, Moscow, USSR (in Russian)

Dymnikov V. P. and Skiba Yu. N., 1985: The barotropic instability of zonally asymmetric flows. Reprint of Department of Numerical Mathematics of the USSR Academy of Sciences, No. 101, Moscow, USSR (in Russian)

Fraedrich K, Bantzer C. and Burkhardt U., 1992: Winter climate anomalies in Europe and their associated circulation at 500 hPa. Cli. Dyn. 8, 161-175

Frankignoul C., 1985: Sea surface temperature anomalies, planetary waves and air-sea feedback in the middle latitudes. Rev. Geophys. 23, 357-390

Glynn W. and Muirhead R., 1978: Influence in canonical correlation analysis. J. Multivariate Analysis, 8, 468-478

Graham N. E., Barnett T. P., Wilde R., Ponater M. and Schubert S., 1994: On the roles of tropical and mid-latitude SSTs in forcing interannual to interdecadal variability in the winter Northern Hemisphere circulation. J. Climate 7, 1416-1441

Held A., 1983: The theory of stationary and quasistationary eddies in the extratropical atmosphere. In: Large-scale dynamical processes in the atmosphere. Edited by B. J. Hoskins and R. P. Pearce, Academic Press, 127-168

Hense A., Glowienka-Hense R., von Storch H. and Stähler U., 1990: Northern Hemisphere atmospheric response to changes of Atlantic Ocean SST on decadal time scales: a GCM experiment. Clim. Dyn. 4, 157-174

Hoskins B. J. and Karoly D. J., 1981: The steady linear response of a spherical atmosphere to thermal and orographic forcing. J. Atmos. Sci. 38, 1179-1196

Kharin V. V., 1995: The relationship between sea surface temperature anomalies and atmospheric circulation in general circulation model experiments. Clim. Dyn. (in press)

Kushnir Y. and Lau N.-C., 1992: The general circulation model response to a North Pacific SST anomaly: Dependence on time scale and pattern polarity. J. Climate 5, 271-283

Lanzante J. R., 1984: The leading modes of 10-30 day variability in the extratropics of the Northern Hemisphere during the cold season. J. Atmos. Sci. 47, 2115-2140

Lau N.-C., 1988: Variability of the observed midlatitude storm tracks in relation to low-frequency changes in the circulation pattern. J. Atmos. Sci. 45, 2718-2743

Lau N.-C. and Holopainen E. O., 1984: Transient eddy forcing of the time-mean flow as identifed by geopotential tendencies. J. Atmos. Sci. 41, 313-328

Lau N.-C. and Nath M. J., 1990: A general circulation model study of the at-

mospheric response to extratropical SST anomalies observed in 1950-79. J. Climate 3, 965-989

Lau N.-C. and Nath M. J., 1994: A modeling study of the relative roles of tropical and extratropical SST anomalies in the variability of the global atmosphere-ocean system. J. Climate 7, 1184-1207

Metz W., 1989: Low-frequency anomalies of the atmospheric flow and the effects of cyclone-scale eddies: a canonical correlation analysis. J. Atmos. Sci. 46, 1026-1041

Metz W., 1994: Singular modes and low-frequency atmospheric variability. J. Atmos. Sci. 51, 1740-1753

Namias, J., 1964: Seasonal persistence and recurrence of European blocking during 1958-1960. Tellus 16, 394-407

Namias, J., 1978: Multiple causes of the North American abnormal winter 1976-1977. Mon. Wea. Rev. 106, 279-295

Navarra A., 1990: Steady linear response to thermal forcing of an anomaly model with an asymmetric climatology. J. Atmos. Sci. 47, 148-169

Navarra A., 1993: A new system of orthonormal modes for linearized meteorological applications. J. Atmos. Sci. 50, 2569-2583

Palmer T. N. and Sun Z., 1985: A modelling and observational study of the relationship between see surface temperature in north-west Atlantic and the atmospheric general circulation. Quart. J. Roy. Meteor. Soc. 111, 947-975

Pedlosky J., 1979: Geophysical Fluid Dynamics. Springer-Verlag, 624 pp.

Pitcher E. J., Blackmon M. L., Bates G. T.and Mu S., 1988: The effect of North Pacific sea surface temperature anomalies on the January climate of a general circulation model. J. Atmos. Sci. 45, 173-188

Ratcliffe R. A. S. and Murray R., 1970: New lag associations between North Atlantic sea temperature and European pressure applied to long-range weather forecasting. Quart. J. Roy. Meteor. Soc. 96, 226-246

Reynolds R. W., 1988: A real-time global sea surface temperature analysis. J. Climate 1, 75-86

Roeckner E., Arpe K., Bengtsson L., Brinkop S., Dü:menil L., Esch M., Kirk E., Lunkeit F., Ponater M., Rockel B., Sausen S., Schlese U., Schubert S.and Windelband M., 1992: Simulation of the present-day climate with the ECHAM model: impact of model physics and resolution. Max-Planck-Institut fü:r Meteorologie, Hamburg, Report No. 93

Simmons A. J., 1982: The forcing of stationary wave motion by tropical diabatic

heating. Quart. J. Roy. Meteor. Soc. 108, 503-534

Simmons A. J., Branstator G. W. and Wallace J. M., 1983: Barotropic wave propagation, instability and atmospheric teleconnection patterns. J. Atmos. Sci. 40, 1363-1392

Ting M., 1991: The stationary wave response to a midlatitude SST anomaly in an idealized GCM. J. Atmos. Sci. 48, 1249-1275

von Storch H. and Zwiers F. W., 1988: Recurrence analysis of climate sensitivity experiments. J. Climate 1, 157-171

Wallace J. M. and Gutzler D. S., 1981: Teleconnections in the geopotential height field during the Northern Hemisphere winter. Mon. Wea. Rev. 106, 296-310

Wallace J. M. and Jiang Q., 1987: On the observed structure of the interannual variability of the atmosphere/ocean climate system. In "Atmospheric and ocean variability", Roy. Meteor. Soc., H. Cattle (ed), 17-43

Wallace J. M., Smith C. and Bretherton C. S., 1992: Singular value decomposition of wintertime sea surface temperature and 500-mb height anomalies. J. Climate 5, 561-576

Wallace J. M., Smith C. and Jiang Q., 1990: Spatial patterns of atmosphere/ocean interaction in the Northern winter. J. Climate 118, 990-998

Webster P. J., 1981: Mechanisms determining the atmospheric response to sea surface temperature anomalies. J. Atmos. Sci. 38, 554-571

Woodruff S. D., Slutz R. J., Jenne R. L. and Steurer P. M., 1987: A Comprehensive Ocean-Atmospheric Data Set. Bull. Amer. Meteor. Soc. 68, 1239-1250

Zorita E., Kharin V. and von Storch H., 1992: The atmospheric circulation and sea surface temperature in the North Atlantic Area in winter: their interaction and relevance for Iberian precipitation. J. Climate 5, 1097-1108